

**SYNTHESIZING SPACECRAFT  
GROUND TRUTH SPECTRA USING  
HOMOGENEOUS MATERIAL  
SPECTRAL BRDFS AND FACETED  
CAD MODELS**

A system to simulate measured quantities utilized for  
unresolved spacecraft characterization

**SYNTHÈSE DE MESURES DE  
RÉFÉRENCES À PARTIR DE  
SPECTRES DE MATÉRIAUX  
HOMOGÈNES ET DE MODÈLES CAD**

Un système pour simuler des quantités utilisées pour  
la caractérisation de satellites non résolus

A Thesis Submitted to the Division of Graduate Studies  
of the Royal Military College of Canada  
by

Alexander Alan Willison, B.Sc., B.Ed.

In Partial Fulfillment of the Requirements for the Degree of  
Master of Science in Physics

July, 2015

---

© This thesis may be used within the Department of National Defence but copyright for open publication remains the property of the author.

*For my wife, Lindsey.  
Thank you for keeping my eyes on the stars, and feet on the ground.*

# Acknowledgements

I would like to thank my supervisor, Major Donald Bédard, for his unwavering support, strong guidance, and jovial camaraderie. His vision inspired the work presented in this thesis, which is built upon foundations that he established. I am forever grateful to Don for taking me in when I showed up on his doorstep.

Thank you also to my co-supervisor, Dr. Gregg Wade, for his pointed questions and thoughtful ideas, helping to advance this work over the many hurdles it has encountered. He started the ball rolling, and it continues to gain momentum.

I would also like to voice my appreciation for my fellows in the Space Surveillance Research Laboratory (SSRL) at the Royal Military College of Canada (RMCC) including Michael Earl, Flight Lieutenant (RAAF) Andrew Jolley, Flight Lieutenant (RAAF) Carl Clancy, and Lieutenant (RCAF) Jason Shaw for their encouragement and assistance. Thanks also to Alex Cushley for his friendship and Matlab assistance.

Finally, words cannot describe the gratitude that I have for the support of my wife, Lindsey. She has worked infinitely harder than I have over the last two years to take care of the both of us. I have been able to complete this thesis because of her. It is for her that I will accomplish much more.

# Abstract

Willison, Alexander Alan., M.Sc., Royal Military College of Canada, July, 2015. *Synthesizing Spacecraft Ground Truth Spectra Using Homogeneous Material Spectral BRDFs and Faceted CAD Models*. Supervised by Major Donald Bédard, Ph.D. Co-supervised by Dr. Gregg Wade.

Resident space objects appear as unresolved point sources in most cases when viewed using ground-based optical telescopes. The measured reflectance spectra of these objects are products of the reflected solar spectrum and their surface material composition, and are a function of the illumination and observation geometry of their illuminated and observable surfaces, atmospheric absorption and scattering effects, and telescope/detector performance. Correct interpretation of these spectra requires a complete optical ground truth characterization of the spacecraft. This is difficult to obtain due to the challenges associated with limited access to completed spacecraft immediately before launch. Systems that produce a synthetic optical spacecraft ground truth characterization, using homogeneous material reflectance properties applied to computer models, present an attractive solution to this problem as they are not impeded by these difficulties.

There are presently systems that model the ground truth spectra of spacecraft, however, they are not peer-reviewed nor commercially or publicly available, leaving the validity of their simulated quantities in question. The most common deficiency of these systems is their dependence on misunderstood functions that inaccurately model material reflection phenomena. The quantity that best describes spectral reflectance is the spectral bidirectional reflectance distribution function (sBRDF), a function of wavelength and four illumination and observation angles, able to reproduce measured changes in intensity and spectral features. All materials possess their own unique sBRDF allowing, in principle, for the reflecting material to be directly inferred from its reflectance spectrum properties.

This thesis presents the development of an open-source system to syn-

---

thesize the sBRDF of spacecraft, which may be utilized to simulate quantities useful for the surface composition characterization of unresolved objects. This research required: the establishment of a homogeneous material reflectance database, an approach to represent the complex surface properties of spacecraft using a computer model, and the derivation of a mathematical algorithm to compute the overall sBRDF of the subject depending on its illumination and observation geometry. The efficacy of the synthetic ground truth system was established through a comprehensive verification process comprised of a series of experiments. The project concluded by synthesizing the sBRDF of the CanX-1 spacecraft engineering model (EM), which was then used to simulate other quantities useful for its surface composition characterization.

**Keywords:** space situational awareness, spectroscopy, ground truth, surface composition characterization, spectral bidirectional reflectance distribution function

# Résumé

Willison, Alexander Alan., M.Sc., Collège militaire royal du Canada, Juillet 2015. *Synthèse de mesures de références à partir de spectres de matériaux homogènes et de modèles CAD*. Supervisé par le major Donald Bédard, Ph.D. Co-supervisé par Gregg Wade, Ph.D.

Les objets spatiaux en orbite apparaissent comme des sources ponctuels non-résolus dans la plupart des cas lorsqu'ils sont observés avec des télescopes terrestres. La réflectance spectrale de ces objets qui est mesurée est un produit du spectre solaire, de la réflectance des matériaux se trouvant à la surface de l'objet, de la géométrie d'illumination et d'observation, des effets atmosphériques ainsi que de la performance du télescope utilisé. Idéalement, une interprétation exacte des spectres de réflectance de l'objet spatial en orbite terrestre requerrait la caractérisation au sol de cet objet avant son lancement dans l'espace, ce qui est pratiquement très difficile d'obtenir. Une solution potentielle à ce problème est l'utilisation de système informatique étant en mesure de générer des mesures de références d'un objet spatial à partir de son modèle CAD ainsi que de spectres de matériaux homogène se trouvant à sa surface.

Il y a présentement quelques systèmes pouvant synthétiser des mesures de références d'un objet spatial par contre leurs performances n'ont pas subis d'évaluation et ils ne sont pas disponibles au public général. De plus, d'après les quelques textes décrivant ces systèmes, ces systèmes utilisent des spectres de matériaux qui ont été acquis sans aucune considération de la géométrie d'illumination et d'observation. La quantité physique qui décrit le mieux les caractéristiques de réflexions spectrales est la fonction de distribution de réflexion bidirectionnelle spectrale. Cette fonction est dépendante de la longueur d'onde ainsi que des quatre angles nécessaires pour définir la géométrie d'illumination et d'observation.

Cette thèse présente le développement du système open-source pour synthèse de mesures de références de spectres satellites pouvant être utilisées pour

---

simuler des quantités utilisées pour la caractérisation de satellites non résolus. Cette recherche a donc requis : le développement d'une base de données de spectres de réflectance de matériaux homogènes de satellites, un approche pour représenter les propriétés de surface d'un satellite à partir d'un modèle informatique, et finalement l'élaboration d'un algorithme pour calculer la réflectance du satellite pour une géométrie d'illumination et d'observation donnée. La performance du système qui a été créé pendant ce projet fut évalué par un processus de validation comprenant une série d'expériences divers. Une fois la validation du système obtenu, le système fut utilisé pour obtenir les signatures spectrales du modèle d'ingénierie du nanosatellite CanX-1 pour différentes géométries d'illumination et d'observation. Ces résultats furent ensuite utilisés pour produire les quantités physiques utiles pour la caractérisation de la composition de la surface du modèle de CanX-1.

**Mots clefs** connaissance de la situation spatiale, spectroscopie, mesures de synthèse, caractérisation de la composition surfacique, fonction de distribution de réflexion bidirectionnelle spectrale



# Contents

<b>Acknowledgements</b>	<b>iv</b>
<b>Abstract</b>	<b>v</b>
<b>Résumé</b>	<b>vii</b>
<b>List of Tables</b>	<b>xiv</b>
<b>List of Figures</b>	<b>xv</b>
<b>1 Introduction</b>	<b>1</b>
1.1 Background . . . . .	1
1.2 Visible-wavelength spectroscopy . . . . .	7
1.2.1 The electromagnetic spectrum . . . . .	7
1.2.2 Spectroscopy . . . . .	8
1.2.3 Reflectance spectroscopy . . . . .	9
1.3 Theoretical foundations of reflection . . . . .	12
1.3.1 Illumination and reflection geometry . . . . .	12
1.3.2 The phase angle . . . . .	13
1.3.3 Definitions of radiometric terms . . . . .	13
1.3.4 The spectral BRDF . . . . .	14
1.3.5 The broadband BRDF . . . . .	15
1.3.6 Colour-filtered BRDFs . . . . .	17
1.3.7 Colour ratios . . . . .	17
1.3.8 Reflection components . . . . .	17
1.3.9 Shadowing and masking . . . . .	19
1.4 Optical ground truth characterization of spacecraft . . . . .	21
1.5 Aim of the research project . . . . .	23
1.6 Thesis outline . . . . .	25

---

<b>2</b>	<b>Spacecraft Ground Truth and Homogeneous Material Characterization</b>	<b>27</b>
2.1	Spectrometric characterization of the CanX-1 EM . . . . .	27
2.1.1	The CanX-1 EM . . . . .	28
2.1.2	Experimental setup . . . . .	29
2.1.3	Experimental procedure . . . . .	29
2.1.4	CanX-1 EM characterization results . . . . .	30
2.1.5	Consideration for spacecraft ground truth synthesis . . . . .	33
2.2	Spectrometric characterization of homogeneous spacecraft materials . . . . .	34
2.2.1	Homogeneous spacecraft materials . . . . .	34
2.2.2	Experimental setup . . . . .	34
2.2.3	Experimental procedure . . . . .	35
2.2.4	Homogeneous spacecraft material characterization results . . . . .	35
	The nature of sBRDFs . . . . .	36
	Normalized broadband BRDFs and colour ratios . . . . .	37
2.2.5	Consideration for spacecraft ground truth synthesis . . . . .	39
<b>3</b>	<b>Literature Survey</b>	<b>41</b>
3.1	BRDF models . . . . .	41
3.1.1	Theoretical BRDF models . . . . .	42
3.1.2	Experimental BRDF models . . . . .	45
3.1.3	Empirical BRDF models . . . . .	46
3.2	Previous attempts to model spacecraft reflectance . . . . .	48
3.2.1	Simulating light curves using computer rendering software . . . . .	48
	Früh and OpenSceneGraph . . . . .	48
	Arnold and LuxRender . . . . .	50
3.2.2	Simulating spacecraft reflectance using TASAT . . . . .	52
	Luu and generating spacecraft spectra using material class reflectance . . . . .	52
	Hall and the production of range-normalized light curves . . . . .	53
3.2.3	Producing radiometric images using DIRSIG . . . . .	57
3.2.4	Light curve simulation in a numerical computing environment . . . . .	61
3.2.5	Approach for a system to produce synthetic spacecraft ground truth . . . . .	62
<b>4</b>	<b>The Synthetic Spacecraft sBRDF System</b>	<b>65</b>
4.1	Redefinition and modification of angles . . . . .	65
4.1.1	Redefining reflection angles . . . . .	65

---

4.1.2	Modifying the illumination and observation angles . . .	66
4.2	A material reflectance database . . . . .	69
4.2.1	Measured material sBRDFs . . . . .	69
4.2.2	Developing comprehensive look-up tables . . . . .	70
4.3	Triangular facets, colour-material definitions, and CAD models	73
4.3.1	Triangular facets . . . . .	73
4.3.2	Colour-material definition . . . . .	74
4.3.3	CAD models . . . . .	74
4.4	System architecture for synthetic spacecraft sBRDF . . . . .	76
4.5	Scene generation . . . . .	78
4.5.1	Placement and orientation of CAD models . . . . .	78
4.5.2	Illumination and observation positions . . . . .	79
4.6	Mathematical algorithm for spacecraft sBRDF synthesis . . . .	81
4.6.1	Facet illumination and observation geometry . . . . .	81
4.6.2	sBRDF acquisition from material reflectance look-up tables . . . . .	82
4.6.3	Synthesis of overall spacecraft sBRDF . . . . .	83
4.7	Producing BRDFs and colour ratios . . . . .	86
4.7.1	Producing BRDFs . . . . .	86
4.7.2	Producing colour-filtered BRDFs . . . . .	86
4.7.3	Producing colour ratios . . . . .	87
<b>5</b>	<b>Verifying the Synthetic Spacecraft sBRDF System</b>	<b>88</b>
5.1	Verification of sBRDF look-up and simulation of BRDFs . . . .	88
5.1.1	Experiment aim and objectives . . . . .	89
5.1.2	Experiment setup and procedure . . . . .	89
5.1.3	Results . . . . .	90
5.1.4	Conclusion . . . . .	92
5.2	Verification of sBRDF look-up tables developed using a cubic spline fit . . . . .	94
5.2.1	Experiment aim and objectives . . . . .	94
5.2.2	Experiment setup and procedure . . . . .	94
5.2.3	Results . . . . .	95
5.2.4	Conclusion . . . . .	97
5.3	Verification of facet contribution calculation . . . . .	100
5.3.1	Experiment aim and objectives . . . . .	100
5.3.2	Experiment setup and procedure . . . . .	100
5.3.3	Results . . . . .	102
5.3.4	Conclusion . . . . .	104
5.4	Assessment of effect of angle conversion for sBRDF look-up . .	105

---

5.4.1	Experiment aim and objectives . . . . .	105
5.4.2	Experiment setup and procedure . . . . .	105
5.4.3	Results . . . . .	106
5.4.4	Conclusion . . . . .	109
5.5	3D model verification . . . . .	110
5.5.1	Experiment aim and objectives . . . . .	110
5.5.2	Experiment setup and procedure . . . . .	110
5.5.3	Results . . . . .	114
5.5.4	Conclusion . . . . .	119
5.6	Summary of conclusions . . . . .	120
<b>6</b>	<b>The Synthetic sBRDF of the CanX-1 EM</b>	<b>121</b>
6.1	Experiment aim and objectives . . . . .	121
6.2	Experiment setup and procedure . . . . .	122
6.2.1	Experimental subject . . . . .	122
6.2.2	Experimental setup . . . . .	122
6.2.3	Experimental procedure . . . . .	123
6.3	Results . . . . .	125
6.3.1	Synthetic sBRDF of the CanX-1 EM . . . . .	125
6.3.2	Simulated BRDF of the CanX-1 EM . . . . .	125
6.3.3	Normalized simulated BRDF and colour ratios . . . . .	125
6.3.4	Normalized simulated BRDFs and colour ratios of the unit cubes for fixed-phase . . . . .	127
6.4	Discussion . . . . .	129
6.4.1	Interpreting the synthetic sBRDF . . . . .	129
6.4.2	Comparing synthetic sBRDF with measured reflectance factor . . . . .	130
6.4.3	Interpreting the simulated BRDF . . . . .	131
6.4.4	Comparing simulated BRDF and measured photometric light curve . . . . .	132
6.4.5	Interpreting the colour ratios . . . . .	133
6.5	Conclusion . . . . .	134
<b>7</b>	<b>Conclusion</b>	<b>136</b>
7.1	Summary of conclusions . . . . .	136
7.2	Future work . . . . .	139
7.2.1	Improved sBRDF look-up tables and a more compre- hensive material reflectance database . . . . .	139
7.2.2	More realistic CAD models . . . . .	140
7.2.3	Expanded CAD model library . . . . .	141

7.2.4	On-orbit simulation scenarios . . . . .	141
7.2.5	Simulated sensor measurements . . . . .	141
	<b>Bibliography</b>	<b>142</b>
<b>8</b>	<b>Curriculum Vitae</b>	<b>147</b>

# List of Tables

3.1	The desired properties of BRDF models. . . . .	42
4.1	Angle ranges of measured material sBRDFs. . . . .	69
4.2	The four matrices of a CAD model facet. . . . .	73
4.3	The colour-material definitions. . . . .	75

# List of Figures

1.1	A spatially resolved satellite. . . . .	2
1.2	Four unresolved satellites. . . . .	3
1.3	A broadband photometric light curve and colour-filtered photometric light curves. . . . .	4
1.4	The solar spectrum is modified by reflection. . . . .	4
1.5	The Bessel BVRI colour filters . . . . .	5
1.6	A normalized broadband photometric light curve and colour ratios. . . . .	6
1.7	The electromagnetic spectrum. . . . .	7
1.8	Fraunhofer's solar spectrum. . . . .	8
1.9	Vesta's relative reflectance ratio. . . . .	9
1.10	Spacecraft reflectance spectra. . . . .	10
1.11	Illumination and reflection geometry. . . . .	12
1.12	The phase angle. . . . .	13
1.13	Three sBRDFs. . . . .	15
1.14	A normalized BRDF. . . . .	16
1.15	Three colour ratios. . . . .	18
1.16	The three reflection components. . . . .	18
1.17	Three cylinders depicting the three components of reflection. . . . .	19
1.18	Shadowing and masking. . . . .	20
1.19	Spacecraft ground truth characterization. . . . .	22
2.1	The CanX-1 EM. . . . .	28
2.2	The CanX-1 EM characterization experiment setup. . . . .	29
2.3	A broadband photometric light curve of the CanX-1 EM. . . . .	31
2.4	A broadband image of the CanX-1 EM. . . . .	31
2.5	Four reflectance factors of the CanX-1 EM. . . . .	32
2.6	A conceptual goniospectrometer setup. . . . .	35
2.7	Three sBRDFs of Azure 3G30A TJPV cell. . . . .	36

---

2.8	Three sBRDFs of 6061-T6 aluminum alloy and Lord Aeroglaze 276A reflective white low-outgassing paint. . . . .	37
2.9	A comparison of the sBRDFs of two TJPV cells. . . . .	38
2.10	A BRDF and associated colour ratios of Emcore TJPV cell and Lord Aeroglaze 276A reflective white low-outgassing paint. . . . .	38
2.11	Three BRDFs and associated colour ratios of 6061-T6 aluminum alloy. . . . .	40
3.1	A flow chart of theoretical BRDF models. . . . .	43
3.2	A flow chart of experimental BRDF models. . . . .	45
3.3	A flow chart of empirical BRDF models. . . . .	46
3.4	Früh's [38] simulated light curve of a Lambertian cube. . . . .	49
3.5	Arnold's [39] simulated light curve of a Lambertian sphere. . . . .	51
3.6	Luu's [6] material reflectance spectral traces. . . . .	54
3.7	Luu's [6] simulated spacecraft spectra. . . . .	55
3.8	Hall's [43] Beard-Maxwell BRDF models and hemispherical reflectance. . . . .	56
3.9	Hall's [43] simulated light curve. . . . .	58
3.10	Bennet's [47] Ward BRDF model. . . . .	59
3.11	Bennet's [47] simulated radiometric image. . . . .	60
3.12	Scott's [48] material BRDFs. . . . .	61
3.13	Scott's [48] simulated light curve. . . . .	63
4.1	The illumination and observation angles of interest to this research project. . . . .	66
4.2	The difference-in-azimuth angle. . . . .	67
4.3	The angle-off-specular. . . . .	68
4.4	A linear interpolation of a measured sBRDF for one illumination angle and wavelength. . . . .	71
4.5	A spline fit of an sBRDF for one angle-off-specular and wavelength. . . . .	72
4.6	The facet represented by the matrices in Table 4.2 . . . . .	74
4.7	Architecture of the synthetic spacecraft sBRDF system. . . . .	76
4.8	CAD model rotation. . . . .	79
4.9	The spherical coordinate system. . . . .	80
4.10	The illumination and observation positions. . . . .	80
4.11	The conversion of the difference-in-azimuth angle from a calculated value to one contained in the material sBRDF look-up table. . . . .	84
4.12	Orthogonal projection of a CAD model. . . . .	85
5.1	A unit sheet CAD model. . . . .	89



---

5.2	Synthetic sBRDFs of Emcore TJPV cell, 6061-T6 aluminum alloy, and Lord Aeroglaze 276A reflective white low-outgassing paint unit sheet. . . . .	91
5.3	Simulated BRDFs and colour ratios of Emcore TJPV cell, 6061-T6 aluminum alloy, and Lord Aeroglaze 276A reflective white low-outgassing paint unit sheet. . . . .	93
5.4	Comparing measured sBRDFs with those produced using a spline fit. . . . .	96
5.5	Simulated BRDFs and colour ratios of Emcore TJPV cell and Lord Aeroglaze 276A reflective white low-outgassing paint unit sheets using sBRDFs produced with a spline fit. . . . .	97
5.6	The simulated BRDFs and colour ratios of a 6061-T6 aluminum alloy unit sheet using sBRDFs produced with a spline fit. . . . .	98
5.7	The all-phase-angle simulation scenario. . . . .	101
5.8	CAD models of mixed composition. . . . .	101
5.9	A comparison of synthetic sBRDFs with and without orthographic area calculation. . . . .	102
5.10	Comparison of BRDFs and colour ratios simulated with and without orthographic area projection. . . . .	103
5.11	Comparison of synthetic sBRDFs produced using models of different size and composition. . . . .	103
5.12	A bow-tie CAD model in two orientations. . . . .	106
5.13	The fixed-illumination and fixed-observation simulation scenarios. . . . .	107
5.14	Fixed-illumination BRDFs and colour ratios for a bow-tie CAD model. . . . .	107
5.15	Fixed-observation BRDFs and colour ratios for a bow-tie CAD model. . . . .	108
5.16	Three three-dimensional CAD models. . . . .	111
5.17	The fixed-phase and fixed-illumination simulation scenarios. . . . .	112
5.18	Model rotation about the $z$ -axis for three-dimensional model verification. . . . .	112
5.19	Fixed-phase BRDFs of an Emcore TJPV cell unit cube. . . . .	114
5.20	Fixed-phase BRDF of a 6061-T6 aluminum alloy unit cube. . . . .	115
5.21	Fixed-illumination BRDFs of an Emcore TJPV cell unit cube and 6061-T6 aluminum alloy unit cube. . . . .	116
5.22	Fixed-phase BRDFs of an Emcore TJPV cell disc and a 6061-T6 aluminum alloy disc. . . . .	116
5.23	Fixed-illumination BRDFs of an Emcore TJPV cell disc and a 6061-T6 aluminum alloy disc. . . . .	117

---

5.24	Fixed-phase BRDFs of an Emcore TJPV cell sphere and a 6061-T6 aluminum alloy sphere. . . . .	118
5.25	Fixed-illumination BRDFs of an Emcore TJPV cell sphere and a 6061-T6 aluminum alloy sphere. . . . .	119
6.1	A scaled photograph of the CanX-1 EM. . . . .	123
6.2	The CanX-1 EM CAD model. . . . .	124
6.3	The phase angle and fixed-phase simulation scenarios using the CanX-1 EM. . . . .	124
6.4	The synthetic sBRDF of the CanX-1 EM for four phase angles. . . . .	126
6.5	A simulated BRDF of the CanX-1 EM. . . . .	127
6.6	The first magnified region of the CanX-1 EM BRDF, associated colour ratios, and five integrated sBRDFs. . . . .	128
6.7	The second magnified region of the CanX-1 EM BRDF, associated colour ratios, and five integrated sBRDFs. . . . .	128
6.8	Magnified regions of the BRDFs and colour ratios of a 6061-T6 aluminum alloy unit cube and Emcore TJPV cell unit cube. . . . .	129
6.9	The normalized synthetic sBRDF of the CanX-1 EM for four phase angles. . . . .	131
7.1	Suggested off-plane sBRDF measurement angles. . . . .	140

# Acronyms

<b>AFRL</b>	Air Force Research Laboratory
<b>AGI</b>	Analytical Graphics, Inc.
<b>AMOS</b>	Air Force Maui Optical Site
<b>ASCII</b>	American Standard Code for Information Interchange
<b>BRDF</b>	bidirectional reflectance distribution function
<b>BVRI</b>	blue-visible-red-infrared
<b>CAD</b>	computer-aided design
<b>CanX</b>	Canadian Advanced Nanospace eXperiment
<b>CCD</b>	charge-coupled device
<b>CMOS</b>	complimentary metal-oxide-semiconductor
<b>DIRSIG</b>	Digital Imaging and Remote Sensing laboratory's Image Generation
<b>EM</b>	engineering model
<b>FOV</b>	field of view
<b>GEO</b>	geosynchronous Earth orbit
<b>HSL</b>	Hue-Saturation-Lightness
<b>HST</b>	Hubble Space Telescope
<b>ICBMs</b>	intercontinental ballistic missiles
<b>LEO</b>	low Earth orbit
<b>MLI</b>	multi-layer insulation
<b>OCS</b>	optical cross-section
<b>OSR</b>	optical solar reflector
<b>RGB</b>	Red-Green-Blue
<b>RSOs</b>	resident space objects
<b>sBRDF</b>	spectral bidirectional reflectance distribution function
<b>SED</b>	spectral energy distribution
<b>SFL</b>	Space Flight Laboratory
<b>SNR</b>	signal-to-noise ratio
<b>SSA</b>	space situational awareness
<b>SSN</b>	Space Surveillance Network

<b>STK</b>	Satellite Tool Kit
<b>STL</b>	STereoLithography
<b>TASAT</b>	Time-domain Analysis Simulation for Advanced Tracking
<b>TJPV</b>	triple-junction photovoltaic
<b>TLE</b>	two-line-element
<b>US</b>	United States
<b>UTIAS</b>	University of Toronto Institute for Aerospace Studies

# 1 Introduction

## 1.1 Background

The need for satellites and other spacecraft is continuously increasing the number of artificial resident space objects (RSOs) in Earth orbit [1]. Understandably, space situational awareness (SSA), defined as “the comprehensive knowledge of the population of space objects, of existing threats/risks, and of the space environment” [2], is becoming increasingly important to manage these valuable space assets as well as identify potential hazards and threats to humans on Earth and in orbit. The “routine, operational service of detection, correlation, characterization, and orbit determination of space objects” [2] is referred to as space surveillance, which promotes SSA.

Orbit determination and tracking is the most established area of space surveillance. The United States (US) Space Surveillance Network (SSN) currently monitors the orbits of more than 21,000 objects larger than 10 cm, a significant proportion of which includes used rocket stages, obsolete satellites, and debris of unknown origin [1]. These RSOs are tracked in order to manage traffic and prevent collisions. They need to be observed within a regular time interval as their orbits are continuously affected by a number of perturbations including the Earth’s non-uniform gravitational field, solar radiation pressure, and manoeuvres, to name a few. Most of the US SSN sensors consist of radar, a technology established for the tracking of intercontinental ballistic missiles (ICBMs) [3], measuring the range and range-rate of targets, quantities useful for orbit determination and tracking. The range of space surveillance radar fences in the US SSN is limited to approximately 30,000 km [4], which is below geosynchronous Earth orbit (GEO).

Optical telescopes are also employed for SSA. Their range is much greater than radar, allowing for orbit determination and tracking of RSOs in GEO. For example, the Keck-II telescope in Hawaii is one of the largest optical telescopes in the world, with a diameter of 10 m. Figure 1.1a shows an image of the GE-23 GEO satellite, a spacecraft with a span of 40 m, taken by this

telescope. The image has limited spatial resolution and is the result of overlaying ten images taken at two wavelengths, for a total exposure time of 0.53 s [5]. A computer model of the satellite is provided in Figure 1.1b for context, presenting the spacecraft's orientation and physical shape.

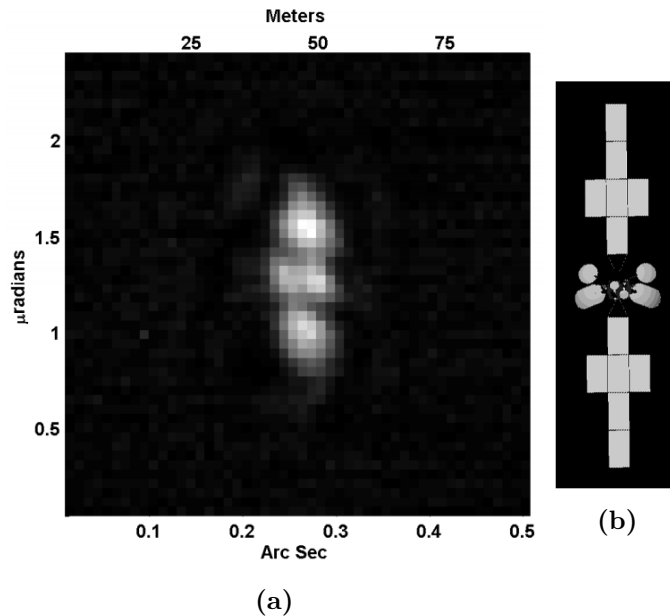


**Figure 1.1:** (a) A resolved image of GE-23 obtained by the Keck-II telescope, and (b) the approximate attitude of the spacecraft for reference. (Source: Drummond, 2010)[5]

Most spacecraft, even those with an altitude less than 1000 km in low Earth orbit (LEO), are beyond the diffraction-limitations of ground-based optical telescopes tasked for space surveillance. Typically on the order of 1 m, these telescopes are unable to obtain any useful spatial resolution in images [6]. An example of an observation made using such a telescope is shown in Figure 1.2, which contains four GEO satellites. These appear as spatially unresolved point sources, indistinguishable from one another. The fact that they were stationary in the field of view (FOV) for the 20-second-long exposure is the only confirmation that these are GEO satellites. This indicates that their motion coincided with that of the Earth-based telescope, which rotates at the same rate. Conversely, the stars streak across the FOV as they have a fixed position on the celestial sphere.

In addition to tracking objects optical telescopes are able to *characterize*

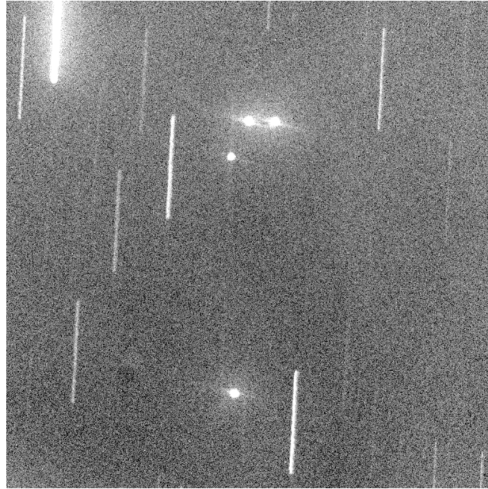


**Figure 1.2:** An image containing Anik-F1, -F1R, -G1, and Echostar 17. (Source: Jolley, 2014)[7]

them. This is the practice of learning more about object nature in order to distinguish them from one another. Distinguishing characteristics include: orientation, rate of change of orientation, physical shape, and surface material composition. Research into the determination of spacecraft characteristics using unresolved observations has focussed on the analysis of *light curves*, using the science of *photometry* [6–10]. A broadband photometric light curve is a plot of the magnitude of spacecraft brightness, essentially a photon count, as a function of time. An example of a broadband photometric light curve is presented in Figure 1.3. Photometric variation has been used successfully to determine the spin rate and spin axis of uncontrolled spacecraft [9], as well as differentiate between co-located satellites in the GEO ring [8].

The light gathered by optical space surveillance sensors is not emitted by RSOs. These objects are in fact illuminated by the Sun, and it is the reflected sunlight that is measured. A consequence of this reflection is a modification of the light’s spectral energy distribution (SED), caused by the spacecraft’s surface materials, shown in Figure 1.4. Spectrometric variation is a change in SED as a function of time, orientation, or both, and is indicative of the composition of the object.

Broadband photometric light curves do not provide any indication of spectrometric variation. Conversely, colour-filtered light curves, products of *colour photometry*, are able to provide insight into the spectral changes occurring within the spacecraft’s reflection over time [7, 10, 12]. These are produced by

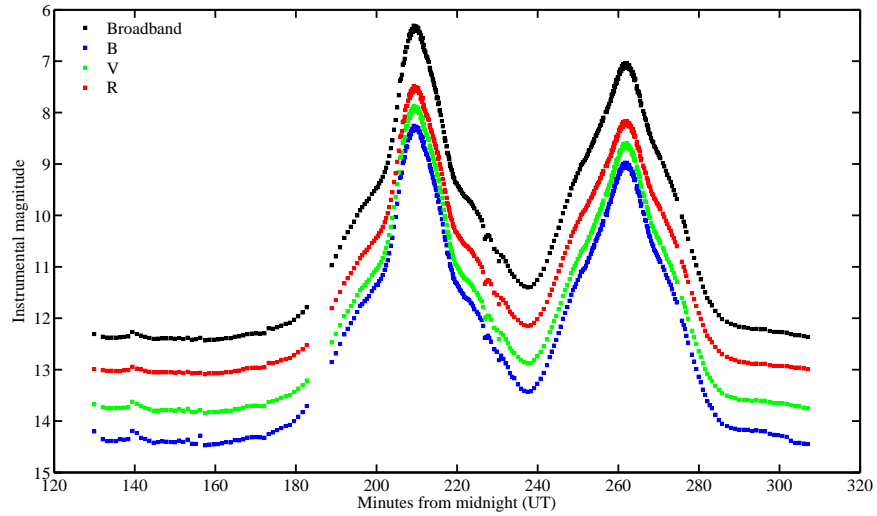


Figure 1.3: A broadband photometric light curve and colour-filtered photometric light curves of the Galaxy 11 GEO satellite. (Source: Bédard, 2015)[11]

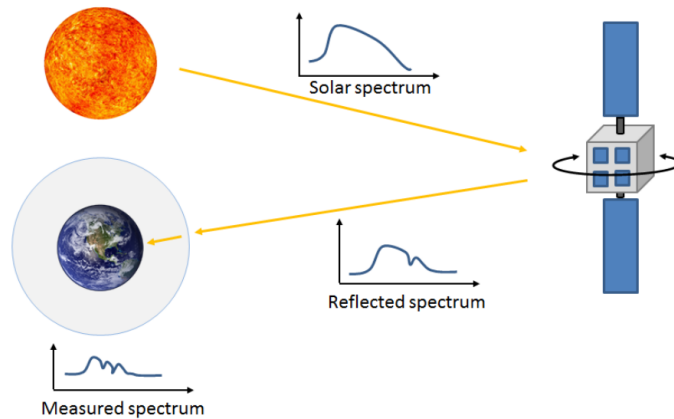
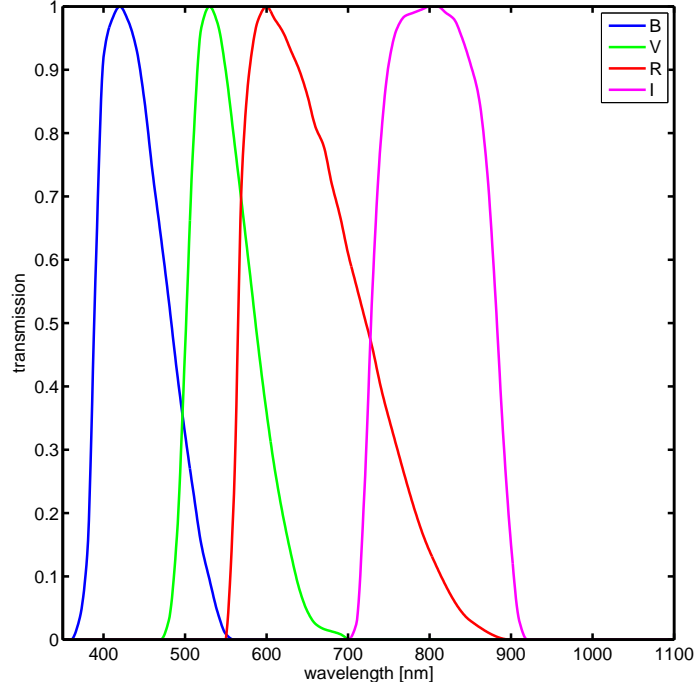


Figure 1.4: The solar spectrum is modified by reflection. (Source: Bédard, 2013)[10]



filtering the reflected photons from spacecraft for specific wavelength ranges. Figure 1.5 provides a visual representation of the four Bessel [13] filters that are commonly used for colour photometry. Three examples of a spacecraft's colour-filtered light curves, measured simultaneously, are provided in Figure 1.3.



**Figure 1.5: The Bessel BVRI filters.**

*Colour ratios*, the quantitative comparison of one colour light curve to another, may be produced using colour-filtered light curves to identify their relative changes over time [13]. Figure 1.6 depicts the colour ratios for the colour-filtered light curves of Galaxy 11 in Figure 1.3 along with the normalized broadband light curve. Note that the colour ratios indicate changes in spacecraft reflection that are not readily seen in the colour-filtered light curves.

Spectrometric observations, measurements of wavelength-resolved spectra, are ideal for the surface composition characterization of unresolved objects. Unfortunately, these are the most difficult to obtain due to the signal magnitudes required to do so. RSOs are constantly changing their orientation towards their illumination source and observer, which in turn affects how reflected light is modified. Combined with the limited size of space surveillance-

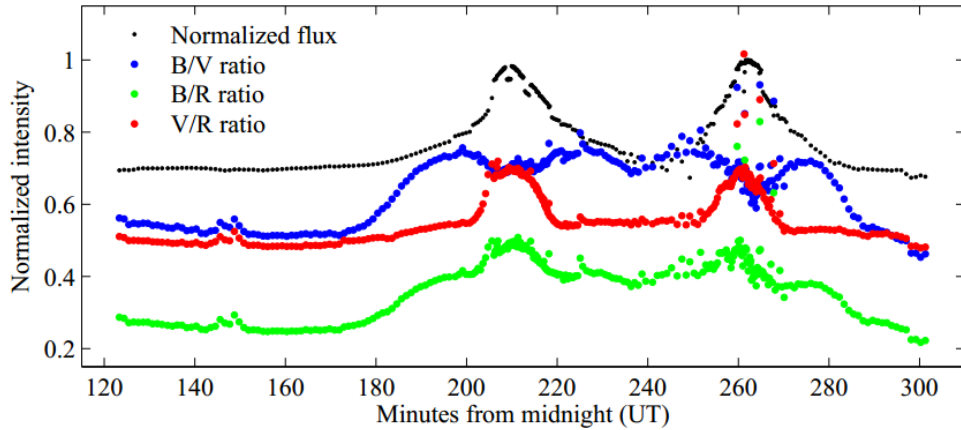


**Figure 1.6:** The normalized broadband photometric light curve and colour ratios of the Galaxy 11 GEO satellite associated with Figure 1.3. (Source: Bédard, 2014)[12]

tasked telescopes, it is difficult to achieve a significant signal-to-noise ratio (SNR) for these measurements [14]. As a result, current space surveillance ability limits surface composition characterization to the interpretation of photometric measurements. Accurate modelling tools are therefore required to produce synthetic spectrometric observations that can be utilized towards this interpretation, allowing for the characterization of unresolved objects for SSA.

This chapter begins by introducing visible-wavelength spectroscopy, the determination of material composition through remote sensing, and reflectance spectroscopy, a science that has been established to characterize asteroids. It then provides the theoretical foundations of reflection as required for this research project, particularly the spectral bidirectional reflectance distribution function. The next section describes the characterization of a spacecraft's optical ground truth characterization, which is essential to interpret its spectra reflected from Earth orbit. The aim of the thesis and outline of the work conducted as part of this research project are then provided. The chapter concludes with an overview of how the thesis is presented.

## 1.2 Visible-wavelength spectroscopy

The ability to determine the composition of an object does not require physical access to that object. Astronomers have been able to identify the composition of the Sun, other stars, planets, asteroids, and comets, through observation using spectroscopy [15]. This section presents the electromagnetic spectrum and highlights the region of importance to this research. It then provides a brief synopsis of spectroscopy and how it has been used in the characterization of distant objects. The section concludes by introducing reflectance spectroscopy, how it has been used to identify the surface composition of asteroids, and the promise it shows towards characterizing the surface composition of spacecraft.

### 1.2.1 The electromagnetic spectrum

The electromagnetic spectrum, shown in Figure 1.7a, encompasses all types of electromagnetic radiation. The entire spectrum ranges from the shortest-wavelength cosmic rays to the longest-wavelength radio waves.

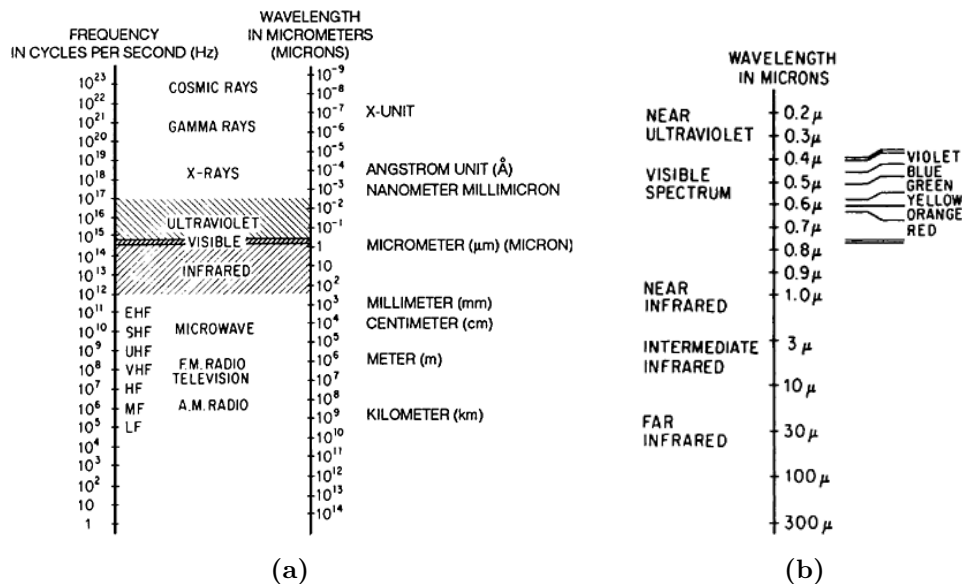
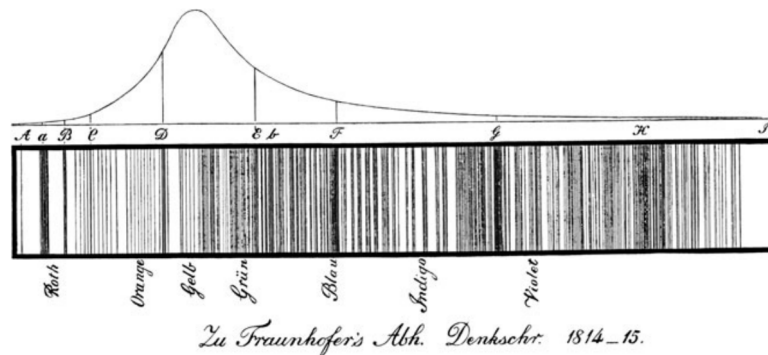


Figure 1.7: The (a) complete electromagnetic spectrum and (b) subdivision of the optical region. One micron is equal to one  $\mu\text{m}$ , or  $10^{-6}$  m. (Source: Smith, 2008)[16]

The electromagnetic region of interest to the research presented here ranges from 350 nm to 1100 nm in wavelength; the visible and near-infrared regions. The ordered subdivision of the visible region by colour is depicted in Figure 1.7b.

### 1.2.2 Spectroscopy

It is possible to determine key characteristics of an object simply through observation, by separating the light that it emits, transmits, or reflects into a spectrum. These characteristics include composition, temperature, and rotation speed. *Spectroscopy* is an optical-analysis method that measures the distribution of photons as a function of wavelength and has been effectively used to build the knowledge base for modern astronomy [15]. Fraunhofer was the first person to analyze the solar spectrum, depicted in Figure 1.8, noticing that the two darkest lines coincided with the emission lines of a candle flame. Kirchoff later proved that the emission lines were indicative of the chemical composition of the light source [15]. In the case of the Sun, the absorption lines were indicative of the chemical composition of the colder elements in its atmosphere.



**Figure 1.8:** Fraunhofer's solar spectrum. (Source: Chromey, 2010)[15]

Most modern astronomical spectroscopy is performed using a spectrograph and a charge-coupled device (CCD) detector. This technology has been used to classify stars according to their spectral types, providing the basis of the Harvard spectral classification system [17]. In addition to determining the chemical composition of stars, astronomers have also used spectra to determine their radial velocities, measuring the Doppler shift of their emission lines [17].

### 1.2.3 Reflectance spectroscopy

The spectral nature of asteroids was first noticed in the 1960s, and they were initially classified based on narrow-band photometric observations [18, 19]. The development of the spectrograph led to *reflectance spectroscopy*, a spectrometric technique first developed to determine the composition of an asteroid, based on its measured spectra [19]. McCord et al. [20] first used this technique to identify the surface composition of Vesta in 1970, by comparing its spectra with laboratory measurements of meteorites and samples returned from the Moon by Apollo 11.

The spectra of solar-illuminated objects, such as asteroids, are produced by dividing the observed spectrum by that of the Sun or a solar analog. Additionally, observations made from Earth need to be corrected as the atmosphere scatters and absorbs some of the reflected light [18]. Figure 1.9 provides Vesta's relative reflectance spectrum, the result of dividing its observed spectrum by a solar analog.

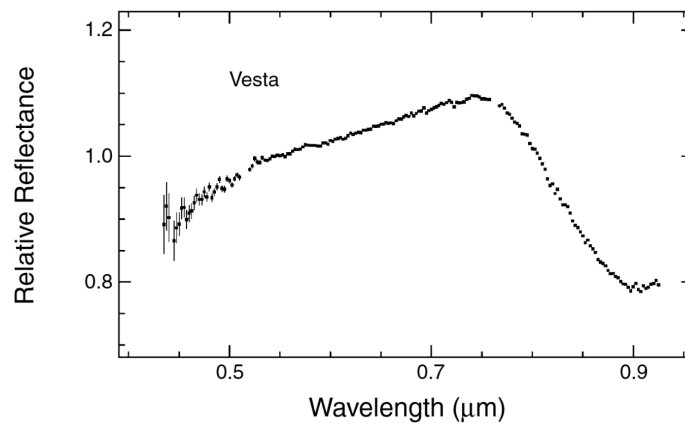


**Figure 1.9:** The relative reflectance ratio produced by dividing Vesta's observed spectrum by a solar analog. (Source: Bus, 2003)[19]

Absorption features in asteroid spectra are specific to certain minerals, allowing for the determination of their surface composition [19]. The confidence of correct mineral identification relies on a number of factors including the shape of the spectral features, the absence of others, and the known presence of the mineral in that particular region of the Solar System [18].

Spacecraft, like asteroids, are illuminated by the Sun. Considering its success with asteroids, the application of reflectance spectroscopy towards the

characterization of spacecraft surface composition is currently being studied [21, 22]. Some examples of the measured spectral of a spacecraft are depicted in Figure 1.10. Note that the spacecraft's reflectance spectrum changes over time.

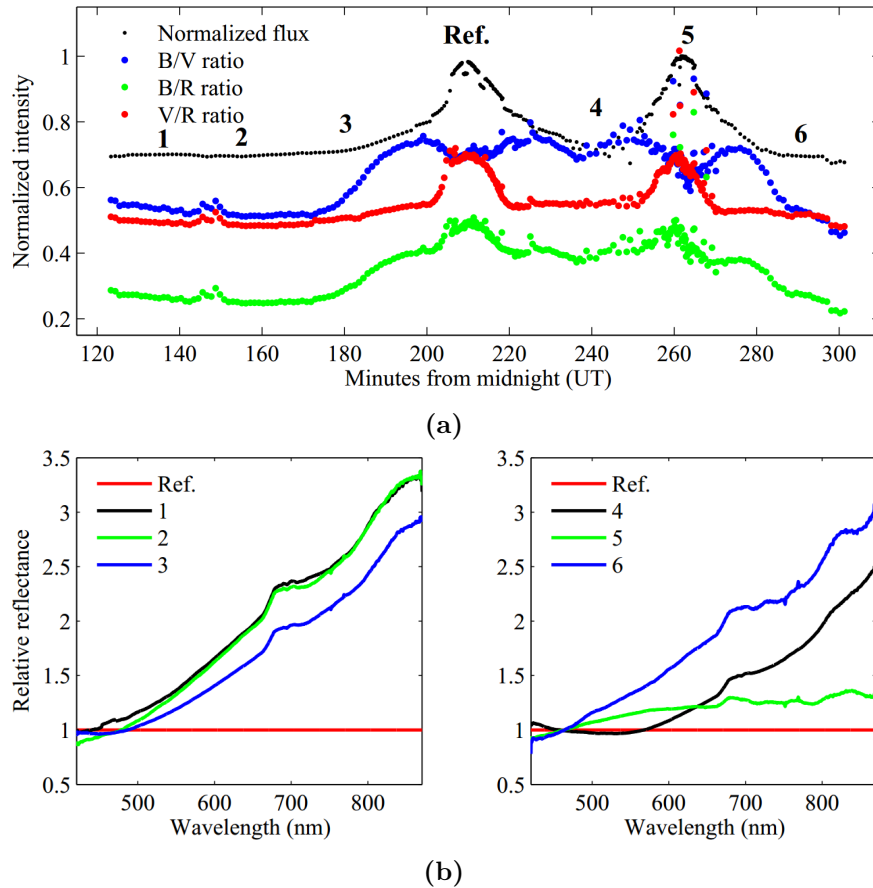


**Figure 1.10:** (a) The normalized broadband photometric light curve and colour ratios of the Galaxy 11 GEO satellite, and (b) the relative reflectance spectra of the spacecraft that correspond with the identification numbers on the light curve. (Source: Bédard, 2014)[12]

Similar to asteroids, spacecraft come in all sizes and shapes and have non-uniform surface composition. Unlike asteroids, these three factors show greater variability. Some spacecraft are no bigger than a basketball, where others are about the size of a school bus; some are simple cubes, while others have cylindrical buses and possess solar panels that extend like wings; and

most have components of different materials, such as aluminum and solar cell, which can have varying amounts of surface roughness or wrinkled texture. All of this variability presents a greater challenge towards the use of reflectance spectroscopy for unresolved spacecraft characterization. Compounding the problem is the fact that spacecraft spectra change over time due to their changing position and orientation.

Simplifying the problem, the surfaces of most spacecraft are composed of a limited number of materials, specifically designed for the space environment. These include aluminum alloys, a typical structural material, and solar cells that convert the Sun's electromagnetic energy into electrical energy. White paints are employed to reflect solar energy from sensitive locations, while multi-layer insulation (MLI) reduces heat loss from the spacecraft body. Therefore, it is important to understand the reflection properties of these materials to characterize the surface composition of spacecraft.

Numerous studies have been conducted to determine the utility of spectra for unresolved spacecraft characterization [6, 21–25]. While none have demonstrated a marked level of success by conclusively determining a spacecraft's physical shape or material composition (or both) solely through the use of spectrometric data, they have provided some insight into what *a priori* knowledge is required. A comprehensive database of material reflection properties is the most critical factor. This is because the spectrum of a spacecraft is a combination of the individual spectra of its component materials, with contributions proportional to their relative abundance [6, 24]. It is not possible to identify the surface composition of a spacecraft without recognizing the spectral characteristics of each individual material. Due to the nature of reflection, this comprehensive database must contain the spectral characteristics for the spacecraft's surface materials, for all orientations, in order to correctly identify them as being present on the spacecraft. Accordingly, knowledge of the physical shape and size of the spacecraft, along with its orientation in space, must be known [6, 24, 25]. Using this information, along with the positions of the illumination source and reflection sensor, the surface composition of a spacecraft can be characterized.

### 1.3 Theoretical foundations of reflection

Reflection is a complex physical phenomenon that is based on a number of factors, including multiple angles, the wavelength of illuminating light, and the physical characteristics of the reflecting material. The goal of this section is to present the theoretical foundations of reflection pertaining to this research project. The section begins by introducing the angles that describe the illumination and reflection geometry, and presents the phase angle. It then defines the radiometric terms that will be referred to throughout this thesis, and derives the spectral bidirectional reflectance distribution function, the focus of the thesis. The section concludes by introducing the components of reflection, as well as shadowing and masking effects.

#### 1.3.1 Illumination and reflection geometry

Illumination and reflection geometry is defined by six angles [26]. Figure 1.11 provides a visual reference of these angles. Illumination angles are denoted by subscript  $i$  and reflection angles are denoted by subscript  $r$ .  $\theta_i$  and  $\theta_r$  are the polar angles subtending the surface normal vector,  $\vec{N}$ , and the illumination and reflection vectors.  $\phi_i$  and  $\phi_r$  are the azimuth angles measured from an arbitrary axis in the surface plane, usually defined by the illumination vector [27], though this is not the case here. Finally,  $\omega_i$  and  $\omega_r$  are the solid angles subtended by the illumination source and reflection beam.

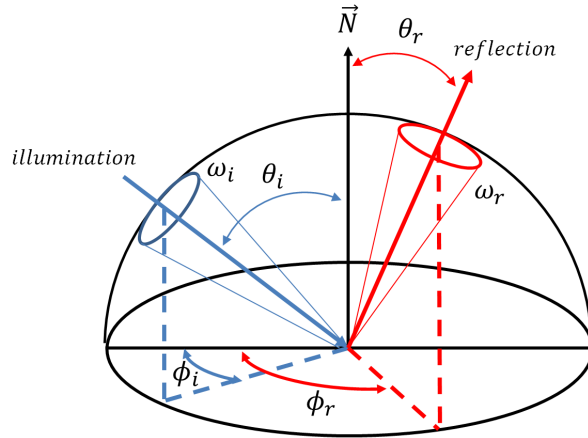


Figure 1.11: The illumination and reflection geometries of an infinitesimal area, defined by its surface normal vector.



### 1.3.2 The phase angle

An angle that is sometimes used to describe illumination and observation geometry is the phase angle,  $\beta$  [28]. Figure 1.12 shows the phase angle, where illumination and observation positions are denoted as  $P_i$  and  $P_o$ , respectively. The phase angle is the angle between the illumination and observation vectors, and lies within the plane defined by the two vectors [28].

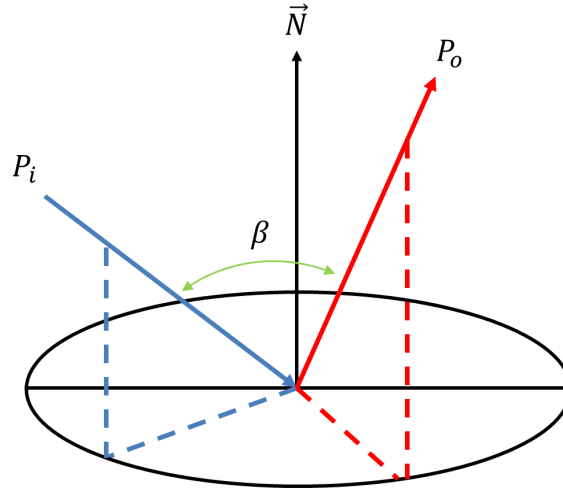


Figure 1.12: The phase angle.

The phase angle does not provide adequate information to describe complete illumination and observation geometry as it does not contain the orientation of the surface [28]. The phase angle is presented here as it is a quantity referred to throughout this thesis.

### 1.3.3 Definitions of radiometric terms

The *radiant flux*,  $\Phi$ , is defined as the rate of energy radiation through space in Watts (W). The incident flux density on a surface is the *irradiance*,  $E_i$ , and is determined using Equation 1.1.

$$E_i = \frac{d\Phi_i}{dA} \quad [\text{W m}^{-2}] \quad (1.1)$$

where  $\Phi_i$  is the incident flux, and  $A$  is the area of the surface in square metres ( $\text{m}^2$ ).

Conversely, *radiant exitance*,  $M_r$ , is the reflected flux density from the surface, shown in Equation 1.2.

$$M_r = \frac{d\Phi_r}{dA} \quad [\text{W m}^{-2}] \quad (1.2)$$

where  $\Phi_r$  is the reflected flux.

Neither the irradiance nor the radiant exitance provide directional information regarding the incident or reflected flux densities, respectively [26]. Direction is incorporated in the *radiance*, where the *incident radiance*,  $L_i$ , is defined to be the incident flux density as a function of the illumination polar angle,  $\theta_i$ , and the illumination source solid angle,  $\omega_i$ , in Figure 1.11. This incident radiance is described by Equation 1.3 [26], where the solid angle is in steradians (sr).

$$L_i = \frac{dE_i}{\cos \theta_i \cdot d\omega_i} = \frac{d\Phi_i}{dA \cdot \cos \theta_i \cdot d\omega_i} \quad [\text{W m}^{-2}\text{sr}^{-1}] \quad (1.3)$$

Conversely, Equation 1.4 defines the *reflected radiance*,  $L_r$ , to be the reflected flux density as a function of the reflection polar angle,  $\theta_r$ , and reflection beam solid angle,  $\omega_r$ , in Figure 1.11.

$$L_r = \frac{dM_r}{\cos \theta_r \cdot d\omega_r} = \frac{d\Phi_r}{dA \cdot \cos \theta_r \cdot d\omega_r} \quad [\text{W m}^{-2}\text{sr}^{-1}] \quad (1.4)$$

### 1.3.4 The spectral bidirectional reflectance distribution function

The bidirectional reflectance distribution function,  $f_r(\theta_i, \phi_i; \theta_r, \phi_r; \lambda)$  is defined by Nicodemus et al. [26] as “the ratio of the reflected radiance from a surface in a given direction to the incident radiance from a given direction, as a function of wavelength per unit steradian”. Schaepman-Strub [29] introduced the term spectral bidirectional reflectance distribution function (sBRDF) to highlight its dependency on wavelength,  $\lambda$ , emphasizing that it is a spectrometric quantity. This relationship is provided in Equation 1.5 [26, 29]. The sBRDF is a function of infinitesimal quantities, making its magnitude independent of surface size.

$$f_r(\theta_i, \phi_i; \theta_r, \phi_r; \lambda) = \frac{dL_r(E_i; \theta_i, \phi_i; \theta_r, \phi_r; \lambda)}{L_i(\theta_i, \phi_i; \lambda) \cdot \cos \theta_i \cdot d\omega_i} \quad [\text{sr}^{-1}] \quad (1.5)$$

Figure 1.13 provides the sBRDF of Sheldahl aluminized polyimide film for three illumination and reflection geometries. Note that the sBRDF is quite different for each geometry, despite  $\theta_r$  being equal to  $\theta_i$ . The fringing pattern

caused by thin-film interference shifts and changes magnitude as a result of a change in  $\theta_i$  [30].

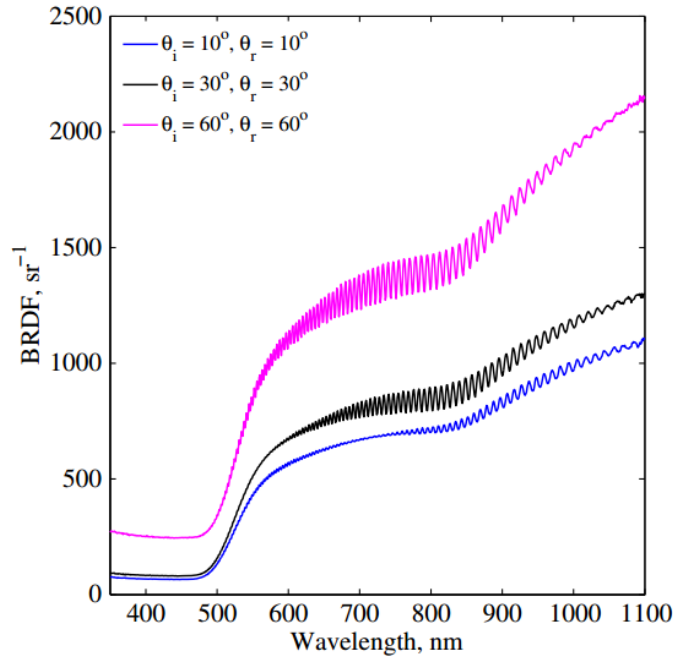


**Figure 1.13:** The sBRDF of Sheldahl aluminized polyimide film for three illumination and reflection geometries. (Source: Bédard, 2015)[30]

In theory, a material's sBRDF can possess an infinite number of values as it is a function of four illumination and reflection angles, and the wavelength of light. In practice this is not feasible as infinitesimal changes in the value of its variables cannot be measured.

### 1.3.5 The broadband bidirectional reflectance distribution function

The broadband bidirectional reflectance distribution function (BRDF),  $f_r(\theta_i, \phi_i; \theta_r, \phi_r)$ , a term first used by Bédard et al. [30], is derived from the sBRDF. It is produced by integrating the sBRDF over a wavelength range, making it a photometric quantity. Equation 1.6 provides the relationship be-

tween the BRDF and sBRDF [30].

$$f_r(\theta_i, \phi_i; \theta_r, \phi_r) = \sum_{\lambda_1}^{\lambda_2} f_r(\theta_i, \phi_i; \theta_r, \phi_r; \lambda) \cdot \Delta\lambda \quad [\text{sr}^{-1}] \quad (1.6)$$

An example of a BRDF is provided in Figure 1.14, taken from the same Sheldahl aluminized polyimide film for  $\theta_i = 10^\circ$ . Each of the BRDF's points is an integrated sBRDF. The BRDF has been normalized here, where the maximum value is equal to one. Note that the fringing that was contained in the sBRDF, a spectral phenomenon, may not be inferred from the BRDF.

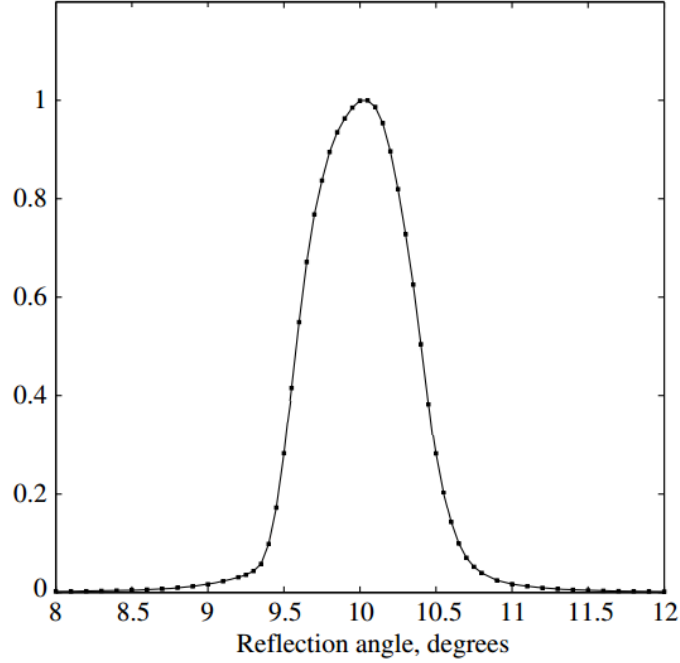


**Figure 1.14: The normalized BRDF of Sheldahl aluminized polyimide film, for  $\theta_i = 10^\circ$ . (Source: Bédard, 2015)[30]**

The BRDF has been used in many ways by different authors, often with confusion. Bédard [30] adopted the naming convention of *spectral* and *broadband* BRDF to promote their differentiation. In keeping with this convention, the spectral BRDF is denoted as sBRDF and the broadband BRDF as BRDF for the remainder of this thesis.

### 1.3.6 Colour-filtered BRDFs

Colour-filtered BRDFs are produced by multiplying the Bessel [13] filter transmittance functions, shown in Figure 1.5, by the sBRDF and integrating the products. This mathematical relationship is shown in Equation 1.7:

$$f_r(\theta_i, \phi_i; \theta_r, \phi_r)_{colour} = \sum_{\lambda_1}^{\lambda_2} T_{colour}(\lambda) \cdot f_r(\theta_i, \phi_i; \theta_r, \phi_r; \lambda) \cdot \Delta\lambda \quad [\text{sr}^{-1}] \quad (1.7)$$

where  $T_{colour}(\lambda)$  is a colour-filter transmittance function.

### 1.3.7 Colour ratios

Colour ratios are calculated using Equation 1.8, where one colour-filtered BRDF is divided by another, in order to visualize their relationship and relative changes.

$$Ratio_{colour_1/colour_2} = \frac{f_r(\theta_i, \phi_i; \theta_r, \phi_r)_{colour_1}}{f_r(\theta_i, \phi_i; \theta_r, \phi_r)_{colour_2}} \quad (1.8)$$

Three examples of colour ratios are provided in Figure 1.15. These are associated with the normalized BRDF of the Sheldahl aluminized polyimide film for  $\theta_i = 10^\circ$ . The ratios depicted here include blue to red ( $B/R$ ), blue to visible ( $B/V$ ), and visible to red ( $V/R$ ), however, inclusion of the I-band allows for more.

### 1.3.8 Reflection components

Reflection by all materials may be modelled using a combination of three components. These include the specular component, the directional-diffuse component, and the uniform-diffuse reflection component [31]. Figure 1.16 shows how each of these components are related to each other and the incident light ray. The specular component polar angle,  $\theta_s$ , is equal to and located in the same plane as  $\theta_i$ , on the opposite side of  $\vec{N}$ ; the directional-diffuse component is lobe-like, with the specular component located near its axis of symmetry; and the uniform-diffuse component is hemispherical.

Equation 1.9 [31] provides the mathematical relationship for this model, with  $\rho$  being defined as the *reflectance*, the fraction of energy reflected with respect to the total incident energy [32]:

$$\rho = \rho_{sp} + \rho_{dd} + \rho_{ud} \quad [\text{unitless}] \quad (1.9)$$

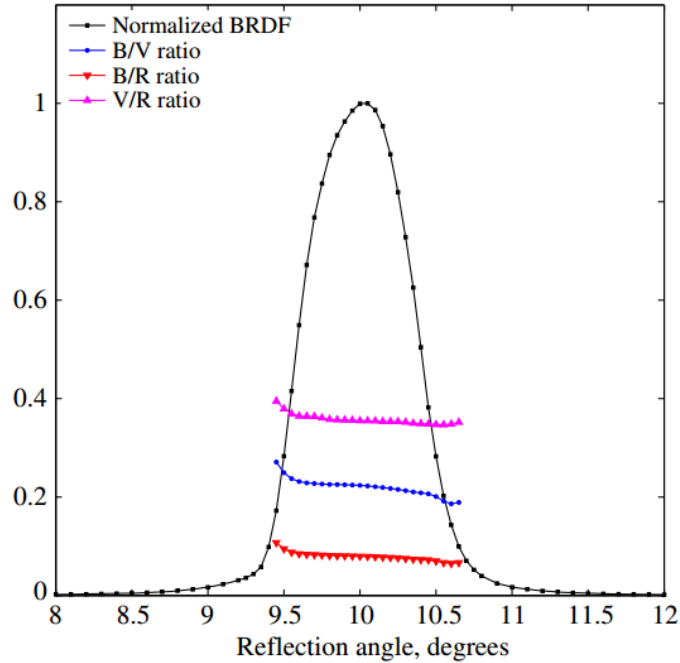


Figure 1.15: Three colour ratios of Sheldahl aluminized polyimide film, associated with the normalized BRDF for  $\theta_i = 10^\circ$ . (Source: Bédard, 2015)[30]

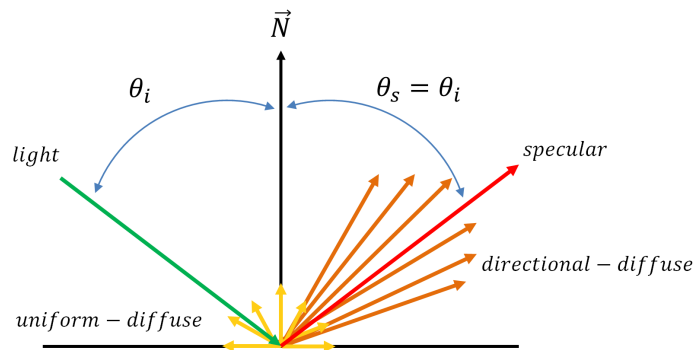
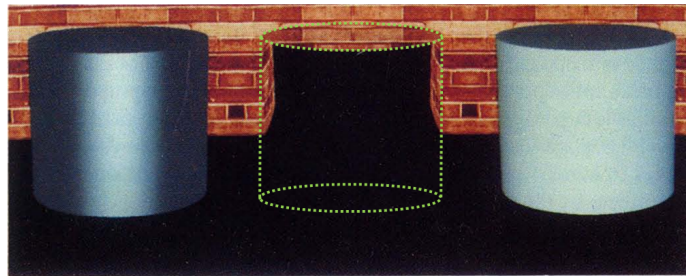


Figure 1.16: The reflection of incident light is a combination of three individual components: the specular, directional-diffuse, and uniform-diffuse.

where  $\rho_{sp}$  is the specular component,  $\rho_{dd}$  is the directional-diffuse component, and  $\rho_{ud}$  is the uniform-diffuse component. These components are presented as they provide a qualitative description of reflectance at various points around the reflecting area, and will be referred to throughout this thesis.

Highly polished or smooth surfaces, such as silver mirrors, have greater specular components. Dull and rough surfaces, such as ceramics, have greater uniform-diffuse components. Most surfaces have a directional-diffuse component where reflected light tends towards the specular direction [33]. These surfaces have a roughness that is larger than the wavelength of light, meaning they are not optically smooth. Figure 1.17 shows how these three components are observed in an object's overall reflection. An ideal specular reflector is the most difficult to observe and will typically appear invisible unless observed within the specular region, as depicted by the specular cylinder.



**Figure 1.17:** Three cylinders corresponding to the three reflection components. From left to right: the directional-diffuse, specular, and uniform-diffuse. Note that the light source is located behind the observer. The specular cylinder does not directly reflect light from the source to the observer, however, the background is mirrored by the top and sides. An outline of the specular cylinder is provided for visualization. (Source: He, 1991)[31]

### 1.3.9 Shadowing and masking

*Shadowing* and *masking* are seen with surfaces that are optically rough [31]. Shadowing is the prevention of a surface from being illuminated by a blocking of the illumination source. Masking is the prevention of a reflected beam from being observed by a blocking of the surface, which can be achieved in two ways: the first is macroscopically by object extremities, such as the solar panels of a spacecraft, while the second is microscopically through surface roughness. Both shadowing and masking effects are shown in Figure 1.18.

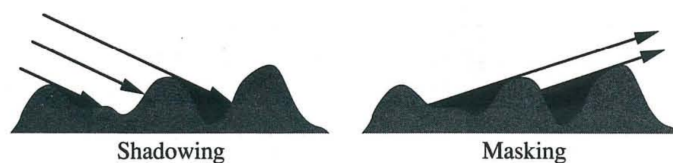


**Figure 1.18: Shadowing and masking of a rough surface. (Source: He, 1991)[31]**

Shadowing and masking effects should be considered when analyzing the reflection properties of a material or object. Depending on the illumination and reflection geometry, these effects can significantly change the results. Neither of these effects are modelled during this research project, however, they are referred to throughout the thesis, and their incorporation into future work is suggested.



## 1.4 Optical ground truth characterization of spacecraft

The optical ground truth characterization of a spacecraft, hereafter referred to as its *ground truth*, is the collection of *a priori* knowledge consisting of its physical dimensions, material composition, and reflectance characteristics [21]. This characterization is obtained in a laboratory, and can be photometric or spectrometric in nature [21, 22]. It serves as a basis for which all reflectance measurements of the spacecraft in Earth orbit will be compared [14].

The method to obtain a spacecraft’s ground truth is to illuminate the entire subject with a collimated light source and take measurements using a far-field camera [22]. Performed in a controlled environment, this allows for the closest recreation of the conditions in which the actual spacecraft will be illuminated and observed while in orbit. Three difficulties present themselves when attempting to obtain an optical ground truth characterization in this manner [14]:

1. Measurements must be made for as many different orientations as possible to reproduce the expected illumination and reflection geometries in orbit.
2. Larger spacecraft are more difficult to illuminate uniformly with a collimated light source as well as observe with a far-field detector.
3. Access to a subject prior to launch can be difficult to obtain, particularly with respect to short mission timelines.

A method to produce the synthetic ground truth of a spacecraft, thereby avoiding the disadvantages of the laboratory characterization listed above, requires measurement of the reflection properties of its component materials. This process is shown in Figure 1.19, where measurements are being taken directly from the spacecraft, however, separate material samples may also be used. Once the material reflectance characteristics are determined they can be applied to computer models to generate a synthetic spacecraft ground truth [21]. This avoids all of the difficulties of the laboratory characterization method as it is easier to manipulate the orientation of small material samples, uniformly illuminate them with a collimated light source, observe them with a far-field sensor, and obtain unhindered access for their analysis. Two disadvantages present themselves with this method. The first is that computer models do not possess the physical flaws of actual spacecraft, such as panels that are not perfectly flush to surfaces, and will therefore not be included. The second is that some materials, such as MLI, are non-uniformly crinkled and their simulated representation will contain uncertainty. Both of

#### 1.4. Optical ground truth characterization of spacecraft

---

these disadvantages are avoided by a laboratory characterization of the actual spacecraft.



**Figure 1.19: (a) The FORMOSAT III spacecraft arranged for optical ground truth characterization, and (b) determining the reflectance characteristics of the solar cells for an unspecified illumination and observation geometry. (Source: Abercromby, 2006)[21]**

The accuracy of a synthetic ground truth depends on the realistic representation of material reflectance for all variations in illumination and observation geometry, across all optical wavelengths of light. The sBRDF meets this requirement as it is a function of illumination and reflection geometry, as well as wavelength. A comprehensive spacecraft material sBRDF database would therefore allow for the production of synthetic optical ground truth characterizations for a significant number of RSOs, allowing for interpretation of their photometric light curves to determine surface composition.

## 1.5 Aim of the research project

The work that is presented in this thesis was conducted to produce a system that could accurately model the reflectance of spacecraft, essentially synthesizing their ground truth. This type of system is necessary so that it is possible to effectively interpret the limited photometric measurements that are made of spacecraft, without requiring their complete optical ground truth characterization before launch. Such a system could also be used as a predictive tool to plan observation missions.

The approach to developing this system was to use triangular-faceted computer-aided design (CAD) models and the sBRDFs of homogeneous materials to synthesize overall spacecraft sBRDF. More precisely, this research project focussed on the synthesis of a spacecraft's ground truth, represented by its overall sBRDF, given *a priori* knowledge of its physical characteristics and material composition. This would allow for the production of BRDFs, colour-filtered BRDFs, and colour ratios. These are quantities that can be interpreted for spacecraft characterization. Alternatively, they can also be used to further produce simulated broadband and colour-filtered light curves, quantities which are measured by optical telescopes, allowing for direct comparison.

The goal of the research project was to develop a system to produce a synthetic sBRDF of a spacecraft, and use this to simulate BRDFs and colour ratios; useful quantities to interpret the spacecraft's surface composition. To achieve this goal, the following objectives were established:

1. Extend limited measured sBRDFs into comprehensive look-up tables, establishing the foundation of a homogeneous material reflectance database.
2. Develop a scheme to represent complex spacecraft as a collection of triangular facets with defined properties.
3. Derive a mathematical algorithm to calculate the illumination and observation geometry of objects in simulation scenarios to produce their overall sBRDF.
4. Simulate BRDFs, colour-filtered BRDFs, and colour ratios using sBRDFs.

The ability of the synthetic ground truth system was assessed in two ways. First, a number of simple experiments were conducted to verify the sBRDF look-up tables, the accuracy of the mathematical algorithm, and the representation of three-dimensional models. The limitations of the system were also determined here. Next, the synthetic sBRDF of the Canadian Ad-

vanced Nanospace eXperiment (CanX)-1 engineering model (EM) was produced, which was then used to simulate the spacecraft's BRDF and colour ratios. All three quantities were interpreted to characterize the surface composition of the spacecraft. The synthetic sBRDF and simulated BRDF were validated through comparison with measurements taken of the CanX-1 EM in a controlled environment.

## 1.6 Thesis outline

The thesis is arranged as follows:

Chapter 2 outlines two characterization experiments. The first presents an experiment to obtain the spectrometric ground truth of the CanX-1 EM spacecraft, while the second outlines the determination of the sBRDFs of homogeneous spacecraft materials. Both experiments provided the impetus for this research project, and their conclusions were utilized when planning the approach to develop the synthetic spacecraft ground truth system. The results of both experiments are provided as they are incorporated into the modelling system, or are used for verification and validation as they present a basis of comparison for the simulated products.

Chapter 3 provides a literature survey of the attempts that have been made to synthesize the ground truth of spacecraft for the purpose of simulating photometric light curves, spectra, and radiometric imagery. Particular attention is paid to the BRDF models that were employed by these systems. The products of each attempt are assessed for accuracy, and the approach of each system is analyzed to determine which features should be incorporated in the system developed for this research project.

Chapter 4 presents the system to synthesize spacecraft ground truth, represented as an sBRDF. It begins by redefining and modifying specific angles, both to develop a comprehensive material sBRDF look-up table and to allow for its access. This is followed by the method to develop these look-up tables using limited measured sBRDF data. An outline of the system architecture is then presented. The mathematical algorithm to synthesize overall spacecraft sBRDF is then derived, employing triangular-faceted CAD models and a colour-material definition system. The chapter concludes by describing the simulation of BRDFs, colour-filtered BRDFs, and colour ratios.

Chapter 5 contains a series of experiments designed to verify the ability of the synthetic spacecraft sBRDF system. First, access of the proper measured sBRDF look-up tables, as well as calculation of illumination and observation geometry is confirmed. An assessment of the comprehensive sBRDF look-up tables to represent material reflectance characteristics is then conducted. Next, proper facet contribution to overall model reflectance is verified. An experiment to determine the effects of a conversion required to use in-plane sBRDF data for off-plane observations is then presented. Finally, BRDFs of three-dimensional objects are simulated to verify that these models are accurately represented.

Chapter 6 presents two simulation scenarios that recreate the laboratory characterization of the CanX-1 EM, in order to validate the ability of the

system to model spacecraft ground truth. The sBRDFs for multiple phase angles of one of the spacecraft's sides are first presented, followed by the BRDF for a fixed-phase scenario. Simulated quantities are interpreted to determine the surface composition of the spacecraft, and are compared to quantities that were measured in a controlled environment. This establishes the validity of the synthetic ground truth system towards producing quantities that are useful for unresolved spacecraft characterization.

Chapter 7 concludes the thesis with a summary of key findings. It also provides a list of suggestions for future work in modelling the reflectance of spacecraft, with the goal of producing more accurate synthetic ground truths, thereby enhancing the ability to characterize the surface composition of objects for SSA.

## 2 Spacecraft Ground Truth and Homogeneous Material Characterization

This chapter presents two characterization experiments that provided the impetus for this research project. The first section outlines the spectrometric characterization of a spacecraft in a controlled environment, thereby establishing its ground truth. This experiment is included as it depicts the key considerations that must be made to synthesize spacecraft ground truth, and contains results that will be used as a basis of comparison with those produced in Chapter 6 by the developed synthetic sBRDF system. The second section presents the measured sBRDFs of several homogeneous spacecraft materials obtained using a goniospectrometer. The measurements will be used to develop the first comprehensive entries in a material reflectance database, which will be utilized to synthesize the ground truth of a spacecraft. This experiment will be repeated in Chapter 5 to validate the accuracy of the synthetic spacecraft ground truth system, and subsequent production of BRDFs and colour ratios.

### 2.1 Spectrometric characterization of the CanX-1 EM

In 2014 Bédard and Lévesque [22] conducted a spectrometric characterization of the CanX-1 EM as part of a research project aimed at furthering the use of reflectance spectroscopy for the purposes of SSA. The aim of the experiment was to develop and test a spacecraft characterization procedure and data analysis method, in order to better understand the requirements for such a characterization before a spacecraft's launch. This characterization would establish the spacecraft's ground truth, against which all in-Earth-orbit obser-

vations could be compared. This section provides a synopsis of this experiment including a description of the spacecraft, the characterization setup, and key results and conclusions related to this research project. The conclusions are considered when planning a system to accurately synthesize spacecraft ground truth, and the results are used for comparison with the developed system's products in Chapter 6.

### 2.1.1 The CanX-1 EM

The CanX Program was developed by the Space Flight Laboratory (SFL) at the University of Toronto Institute for Aerospace Studies (UTIAS), attempting to test pico-scale spacecraft in space [34]. The CanX-1 was the first spacecraft of the program, having a size of approximately  $10 \text{ cm}^3$  and a mass of 1 kg [34]. The CanX-1 EM, shown in Figure 2.1, was chosen for characterization by Bédard and Lévesque [22] as it was an actual spacecraft, and the simple cubic design allowed for straightforward interpretation of measurements.

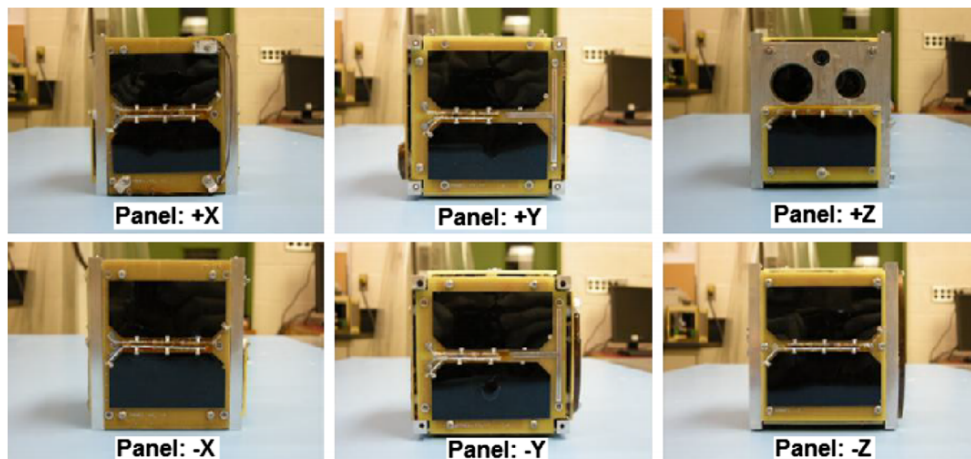


**Figure 2.1:** The six sides of the CanX-1 EM. (Source: Bédard, 2014)[22]

Five sides of the spacecraft were dominated by two Emcore triple-junction photovoltaic (TJPV) cells and possessed 6061-T6 aluminum alloy launch rails. The sixth side, labelled as +Z, only had one solar cell while the remainder of this side was comprised of an aluminum panel. The voids on the +Z side were the location of complimentary metal-oxide-semiconductor (CMOS) sensors on the actual spacecraft; however, they were not present in the EM.



### 2.1.2 Experimental setup

The experimental setup was designed to obtain both broadband and spectrometric reflectance of the CanX-1 EM for a range of phase angles. The spacecraft was placed on a turntable that could be rotated a full  $360^\circ$ , in increments of  $1^\circ$ , and was illuminated by a collimated light source. A CCD camera was used to obtain photographic images of the spacecraft which functioned to interpret the spectrometric measurements as well as produce broadband photometric light curves. A portable spectrometer, with a band ranging from 350 nm to 2500 nm, was co-located with the CCD camera. Figure 2.2 depicts the characterization setup including the subject, illumination source, and sensors.

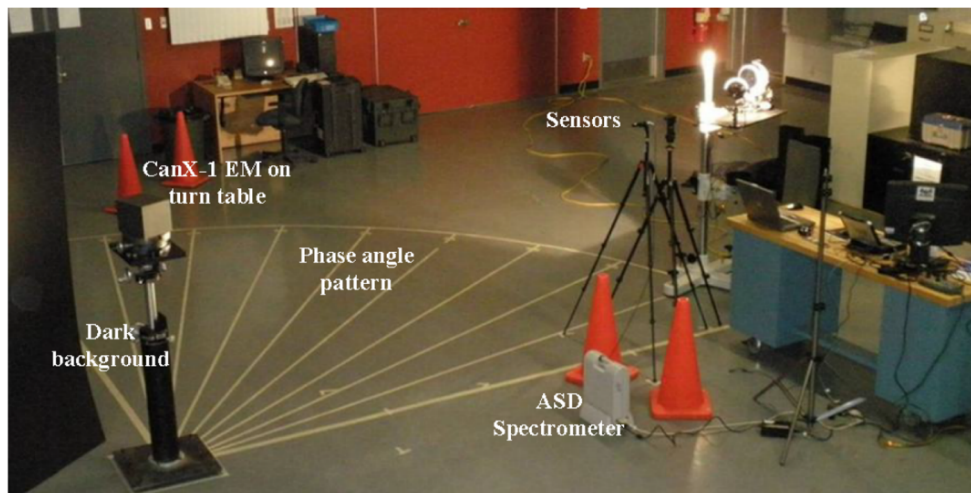


**Figure 2.2:** The setup of the CanX-1 EM, illumination source, and spectrometric sensor. (Source: Bédard, 2014)[22]

The setup was designed with the intention of acquiring as many of the illumination and observation geometries that would be presented when observing the spacecraft using a telescope [22]. This would allow for a direct comparison of measurements made of the CanX-1 EM in the laboratory to those of the CanX-1 in orbit.

### 2.1.3 Experimental procedure

The *reflectance factor*, defined by Nicodemus et al. [26] as “the ratio of the radiant flux reflected from a sample surface to that which would be reflected into the same reflected-beam geometry by a loss-less perfectly [Lambertian]

standard surface irradiated in exactly the same way as the sample”, was chosen to spectrometrically characterize the CanX-1 EM. Equation 2.1 provides the mathematical expression for this quantity [26]. Note that calculation of the reflectance factor removes data concerning the relationship between illumination angle and reflectance magnitude, essentially normalizing the result.

$$R(\lambda) = \frac{d\Phi_r(\theta_i; \theta_r; \lambda)}{d\Phi_{r,Lambert}(\theta_i; \theta_r; \lambda)} \quad [\text{dimensionless}] \quad (2.1)$$

The reflectance of the spacecraft was expected to be highly specular, exhibiting minimal directional-diffuse and uniform-diffuse components due to the dominance of its surface by the solar cells [22]. Measurements were therefore acquired for each phase angle where reflection was detected, in spacecraft rotation increments of 1°. Reference measurements of a diffuse Spectralon panel were taken for the same geometries where reflection was detected to calculate the reflectance factor.

#### 2.1.4 CanX-1 EM characterization results

Broadband light curves were produced by integrating the mean intensity of each spacecraft image for a particular phase angle, yielding a series of photometric counts [22]. Figure 2.3 provides an example of a broadband photometric light curve for a phase angle of 10°, where the spacecraft was rotated about the  $z$ -axis. The initial rotation of the spacecraft and the order in which the sides were observed were not described.

Based on the photometric light curves Bédard and Lévesque [22] concluded that the CanX-1 EM was a specular reflector due to the sharp peaks separated by minimal signal. The images showed that the TJPV cells were responsible for these peaks. Secondly, the varied widths of the peaks indicated that the solar cells were not perfectly flat, nor flush to the spacecraft body. This was also evident in the images, as shown in Figure 2.4. While not discussed by the authors, this was likely also the cause of the variation in peak magnitude. Finally, the 90° separation of the photometric peaks revealed that the CanX-1 EM was cubic.

Only the TJPV cells and the 6061-T6 aluminum alloy were detected in the spectrometric data. All measurements taken within the specular region of the Emcore TJPV cells exhibited a fringing pattern which shifted towards shorter wavelengths with an increase in phase angle [22]. Figure 2.5 shows this shift for three spectral features, located between 600 nm and 800 nm, as the phase angle was increased from 5° to 90°.

## 2.1. Spectrometric characterization of the CanX-1 EM

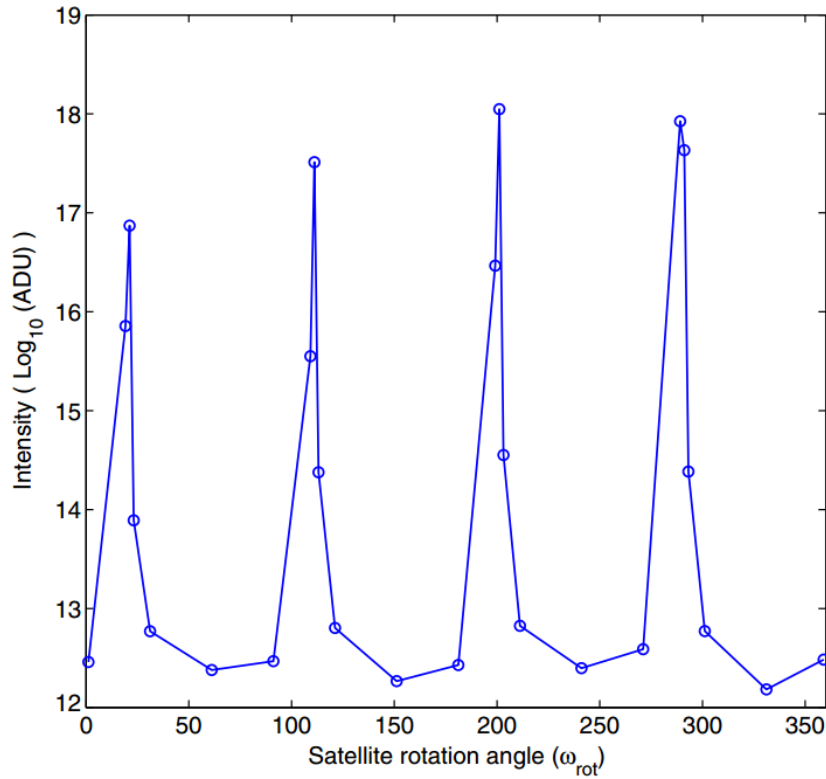


Figure 2.3: A broadband photometric light curve of the CanX-1 EM for a phase angle of  $10^\circ$  and spacecraft rotation of  $360^\circ$ . (Source: Bédard, 2014)[22]

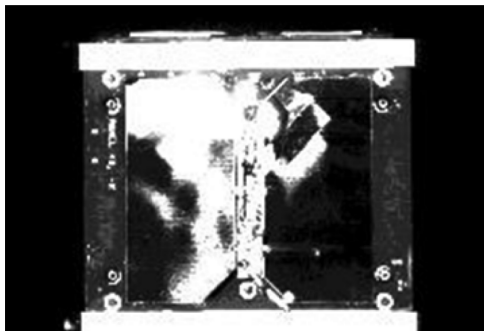
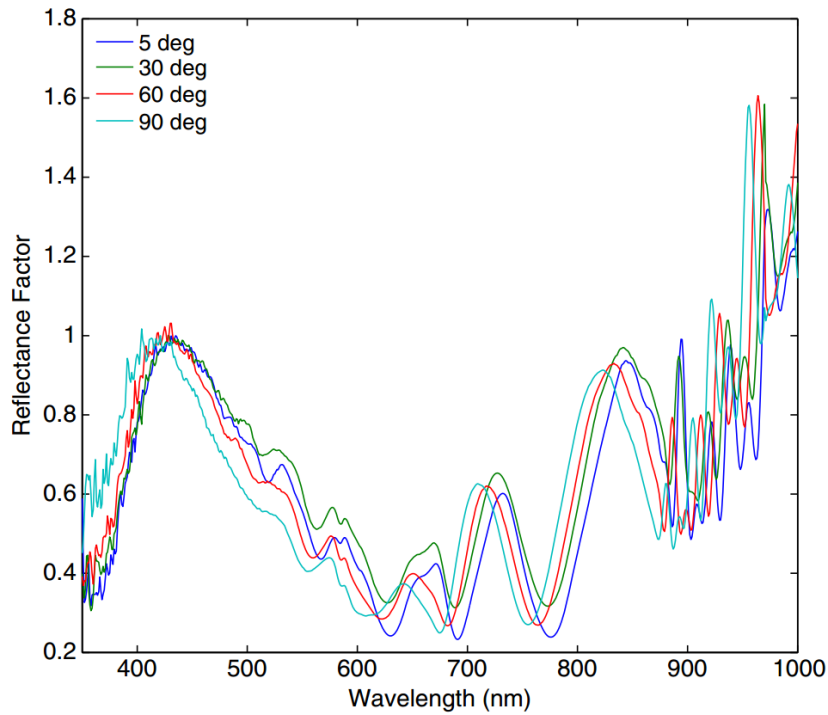


Figure 2.4: A broadband image of the CanX-1 EM, where the solar cell's reflection indicates it is not perfectly flat nor flush. (Source: Bédard, 2014)[22]



**Figure 2.5: Reflectance factor of the +X side of the CanX-1 EM for four phase angles. (Source: Bédard, 2014)[22]**

Aluminum was detected within the measured spectra outside of the specular region of the TJPV cells, particularly for the +Z side, as evidenced by a broad absorption feature near 800 nm [22]. The aluminum could not be detected within the specular region of the solar cells, nor was there an indication as to whether the spectral feature shifted with a change in phase angle.

Based on the characterization of the CanX-1 EM, Bédard and Lévesque [22] concluded that spacecraft reflectance is more complicated than previously thought. The shape of reflected spectra are not constant for spacecraft, and consideration of illumination and observation geometry is critical, as evidenced by the spectral features of the Emcore TJPV cells in this experiment. Therefore, in order for spectrometric measurements of spacecraft in orbit to be compared to ground truth data, the illumination and observation geometries of all reflecting spacecraft panels need to be considered. Any changes in intensity associated with illumination angle were lost due to the nature of the reflectance factor, leaving the utility of this quantity for spectrometric characterization in question.

### 2.1.5 Consideration for spacecraft ground truth synthesis

The CanX-1 EM spectrometric characterization experiment is presented here for two reasons. First, important considerations that must be made in order to accurately synthesize the ground truth of spacecraft were highlighted. Second, this experiment produced results that can be used as a basis of comparison to assess the validity of a system to synthesize the ground truth of a spacecraft.

A spacecraft's spectrum is the product of a number of factors including its surface material composition and the illumination and observation geometry of its panels. In order for spectra to be accurately synthesized the shape of the spacecraft must be known, including the distribution of materials on each of its surfaces. Also, knowledge of the spectral reflectance characteristics of each of its materials is required, including how these characteristics change as illumination and observation geometry varies. A system to produce the synthetic ground truth of a spacecraft therefore needs to be able to calculate the geometries of all panels and determine their material composition. A comprehensive database of the spectral reflectance of homogeneous materials is required for this system to generate the spacecraft's overall spectrum. The reflectance factor is not suitable for spacecraft ground truth characterization as intensity is not proportional to illumination angle within this quantity. The homogeneous material spectral reflectance database should contain a quantity that maintains this relationship.

This experiment is a great candidate to assess the validity of synthetic spacecraft ground truth systems as it is relatively straightforward to repeat. The CanX-1 EM is simple in shape and composition which makes it easy to model. Its panels, while containing the same materials, vary their relative abundance and orientation which will allow for attempts at differentiation between their synthetic spectra. Definition of the illumination and observation positions only requires an angular separation and a radial distance from the spacecraft, which rotates around a single axis. The validity of a synthetic spacecraft ground truth system can be established by comparing its products with the spectrometric and broadband photometric light curves that were measured during the CanX-1 EM characterization.

## 2.2 Spectrometric characterization of homogeneous spacecraft materials

An analysis of the sBRDFs of homogeneous materials commonly found on spacecraft surfaces was performed by Bédard et al. [30] in 2015. This research was conducted to better understand how material spectra changed as a function of illumination and observation geometries. This section provides a synopsis of that study, including a description of the goniospectrometer used to obtain material sBRDFs, and key results and conclusions related to this research project. Some of the sBRDFs that were collected as part of this analysis were the initial entries into a comprehensive material sBRDF database utilized by the synthetic spacecraft ground truth system developed for this research project. The results of this experiment are also used for the interpretation of synthetic sBRDFs, broadband BRDFs, and colour ratios in Chapters 5 and 6.

### 2.2.1 Homogeneous spacecraft materials

A total of 10 material samples, comprising 4 spacecraft material classes, were spectrometrically characterized during this study. The material classes included solar cell, aluminum, white paint, and MLI. Only four material samples are presented here including Azure 3G30A and Emcore TJPV cells, 6061-T6 aluminum alloy, and Lord Aeroglaze 276A reflective white low-outgassing paint, as they demonstrate reflectance behaviours related to this thesis. The latter three materials are incorporated into the comprehensive material sBRDF database developed in Chapter 4, which is utilized to synthesize spacecraft ground truth.

### 2.2.2 Experimental setup

Bédard et al. [30] used a goniospectrometer to characterize homogeneous material samples. The apparatus included a fixed collimated light source, an armature-mounted spectrometric sensor on one rotary stage, and a second rotary stage on which samples were situated. The rotary stages could be positioned at angles with an accuracy of  $0.05^\circ$ . The goniospectrometer was designed so that the sensor was in the plane defined by the position of the light source and the centre of the sample, itself located at the centre of the illumination beam. Samples were mounted so that the plane of the illuminated surface was intersected by the rotation axis of both rotary stages, ensuring that illumination and observation angles would share a common vertex point

on the sample. The conceptual representation of the device is shown in Figure 2.6. This setup allowed for the acquisition of the sBRDF over a wide range of illumination and observation geometries, intending to observe how this reflectance quantity changed with variations in these angles.

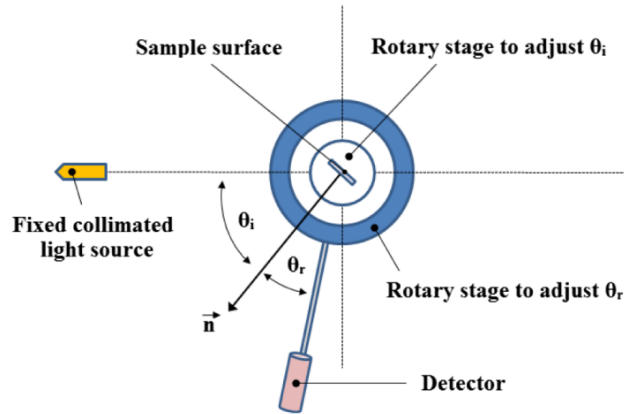


**Figure 2.6:** A conceptual goniospectrometer setup. (Source: Bédard, 2015)[30]

### 2.2.3 Experimental procedure

Reflectance spectroscopy was used to spectrometrically characterize the homogeneous spacecraft materials, with the collimated light source being the reference that was divided out of the observed spectra. Material samples were observed for three  $\theta_i$  values:  $10^\circ$ ,  $30^\circ$ , and  $60^\circ$ . Measurements were obtained across the range of  $\theta_r$  that exhibited reflectance, in increments that depended on the rate of change of the intensity. All measurements were made in the same plane since the two azimuth angles,  $\phi_i$  and  $\phi_r$ , were respectively  $0^\circ$  and  $180^\circ$ , as measured from the direction of the illumination position.

### 2.2.4 Homogeneous spacecraft material characterization results

The results of the spectrometric characterization experiment are presented in two sections. The first contains the material sBRDFs and provides an analysis of their nature. The broadband BRDFs and colour ratios of each material are then provided for later reference.

### The nature of sBRDFs

Measurements of the Azure 3G30A TJPV cell's sBRDF, for three phase angles, are presented in Figure 2.7. The spectral features shifted towards shorter wavelengths with an increase in  $\theta_i$ . Bédard et al. [30] noted this was true for all solar cell samples, and was consistent with results of the spectrometric characterization of the CanX-1 EM. Also noted was the increase in magnitude with increase in  $\theta_i$ . This effect was not observed in the spacecraft characterization experiment due to the nature of the reflectance factor, which normalizes the magnitudes of all reflectance spectra, further suggesting its limited utility.

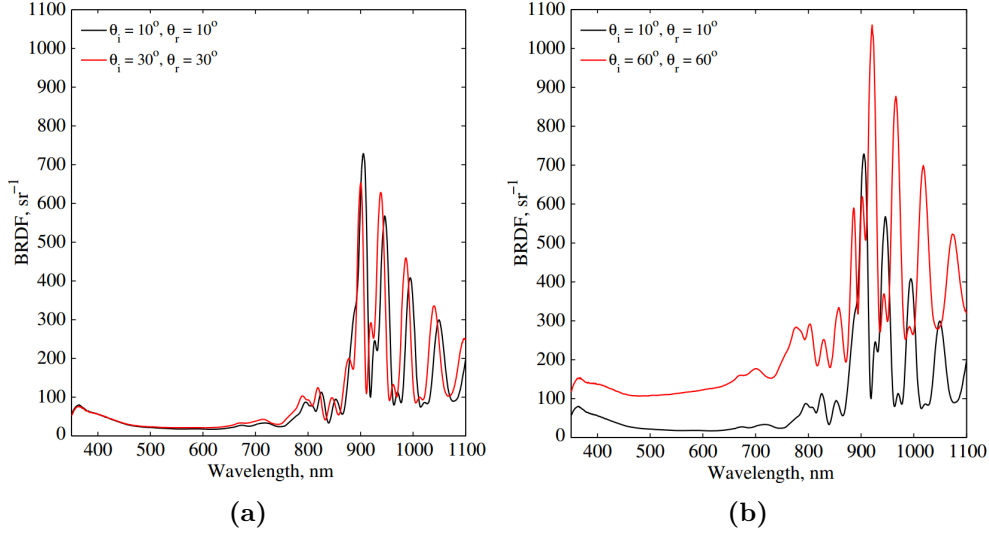


**Figure 2.7:** The sBRDF of Azure 3G30A TJPV cell for  $\theta_i = \theta_r = 10^\circ$  and (a)  $\theta_i = \theta_r = 30^\circ$  (b)  $\theta_i = \theta_r = 60^\circ$ . (Source: Bédard, 2015)[30]

The sBRDFs of 6061-T6 aluminum alloy and Lord Aeroglaze 276A reflective white low-outgassing paint are presented for three phase angles in Figure 2.8. Figure 2.8a depicts an absorption feature at 800 nm which is characteristic of aluminum [30]. The white paint's reflectance is fairly uniform across all wavelengths. Similar to the solar cells, reflectance increased with an increase in  $\theta_i$ .

A comparison of sBRDF measurements of the Azure and Emcore cells, for  $\theta_i = \theta_r = 30^\circ$ , is presented in Figure 2.9. While both of these samples are of the solar cell class, both the spectral features and amount of reflectance is characteristic of their respective materials. One reason for the low reflectance of the Emcore cell was its condition, which when compared to the Azure cell,



## 2.2. Spectrometric characterization of homogeneous spacecraft materials

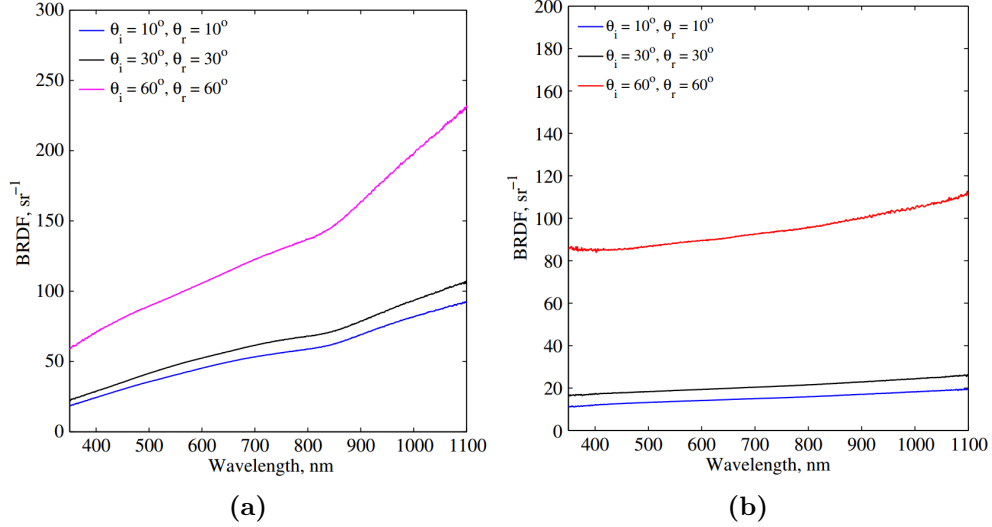


**Figure 2.8: The sBRDF of (a) 6061-T6 aluminum alloy, and (b) Lord Aeroglaze 276A reflective white low-outgassing paint, for three illumination and observation geometries. (Source: Bédard, 2015)[30]**

was significantly degraded [30]. A comparison of degraded Emcore versus pristine Emcore was not conducted. Regardless, based on the unique spectral profiles, Bédard et al. [30] concluded that differentiation of samples within the same material class was possible.

### Normalized broadband BRDFs and colour ratios

Considering the variations in the colour ratios near the edges of the SED of the collimated light source, it was decided that the material colour ratios were unreliable when the normalized BRDF was below 0.2, and were not calculated for this range. Figure 2.10a depicts the normalized BRDF and colour ratios of the Emcore TJPV cell for  $\theta_i = 30^\circ$ . Since the BRDF had a width of approximately  $1^\circ$  it was confirmed to be a specular reflector. The asymmetric nature of the colour ratios were attributed to the degraded surface condition of the solar cell. The colour ratios of all other solar cell samples, which were in better visual condition, exhibited a more U-shaped pattern [30]. The Emcore cell colour ratios presented a relatively similar shape and magnitude for all three measured  $\theta_i$  values, in relation to the BRDF.

The same quantities for the Lord Aeroglaze 276A reflective white low-outgassing paint, for  $\theta_i = 60^\circ$ , are shown in Figure 2.10b. This material is less

2.2. Spectrometric characterization of homogeneous spacecraft materials

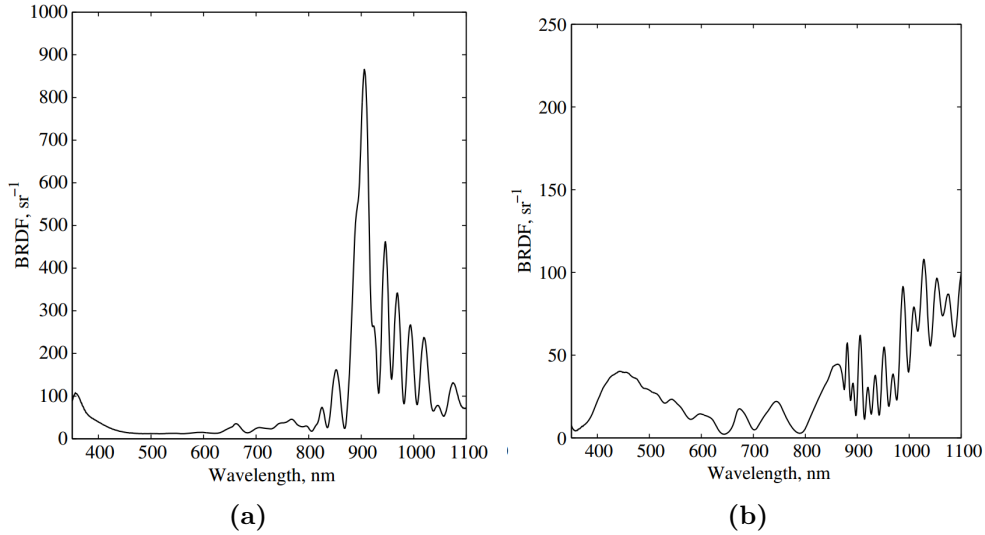


Figure 2.9: The sBRDF for  $\theta_i = \theta_r = 30^\circ$  of two TJPV cells. (a) Azure 3G30A, and (b) Emcore. Note the different vertical scales. (Source: Bédard, 2015)[30]

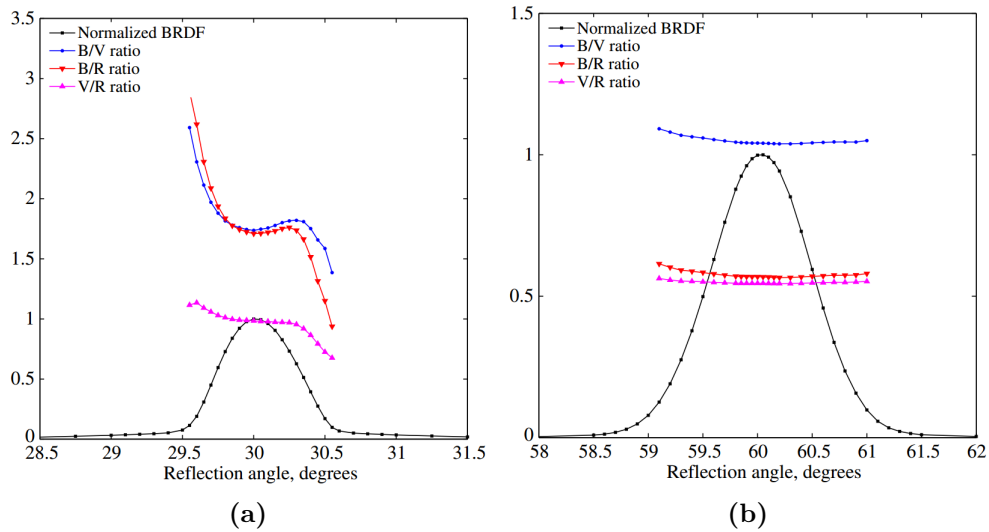


Figure 2.10: The normalized BRDF and colour ratios of (a) Emcore TJPV cell for  $\theta_i = 30^\circ$ , and (b) Lord Aeroglaze 276A reflective white low-outgassing paint for  $\theta_i = 60^\circ$ . (Source: Bédard, 2015)[30]

specular as its BRDF has a width of approximately  $3^\circ$ . The colour ratios are uniform across the entire BRDF and behave similarly for all three measured  $\theta_i$  values like those of the solar cell.

The normalized BRDFs and colour ratios of the 6061-T6 aluminum alloy for all three  $\theta_i$  values are presented in Figure 2.11. This is the least specular material as the widths of its BRDFs are the greatest of the three. Note that with an increase in  $\theta_i$  the BRDF width decreases and the slope increases. The colour ratios were similar for each  $\theta_i$  and relatively uniform across the BRDF [30].

### 2.2.5 Consideration for spacecraft ground truth synthesis

The spectrometric characterization of homogeneous materials is presented here for three reasons. First, the nature of material sBRDFs and how they change with illumination and observation geometry was demonstrated. Next, the measured sBRDFs were used to develop a comprehensive material reflectance database, intended to be used by the synthetic spacecraft ground truth system. Finally, the results provide a basis of comparison to assess the validity of said system.

Material sBRDFs change with illumination and observation geometry. Increasing  $\theta_i$  causes intensities to increase, and for some materials, the spectral features to shift towards shorter wavelengths. A single sBRDF may not be used to represent an entire material class as individual samples exhibit their own distinct sBRDF. A system to produce synthetic spacecraft ground truth should therefore utilize a comprehensive reflectance database containing the sBRDFs of the spacecraft's component materials.

The sBRDFs of Emcore TJPV cell, 6061-T6 aluminum alloy, and Lord Aeroglaze 276A reflective white low-outgassing paint were measured during the homogeneous material spectrometric characterization. These will be developed into the required comprehensive look-up tables utilized to synthesize the ground truth of spacecraft.

Similar to the spacecraft characterization experiment in Section 2.1, this experiment is also relatively straightforward to repeat and will be used to validate the sBRDF look-up tables and synthetic spacecraft ground truth system. As with the CanX-1 EM experiment, definition of the illumination and observation positions requires an angular separation and a radial distance from the sample, which rotates around a single axis. All results provide a basis of comparison for validation of the system developed for this research project.

## 2.2. Spectrometric characterization of homogeneous spacecraft materials

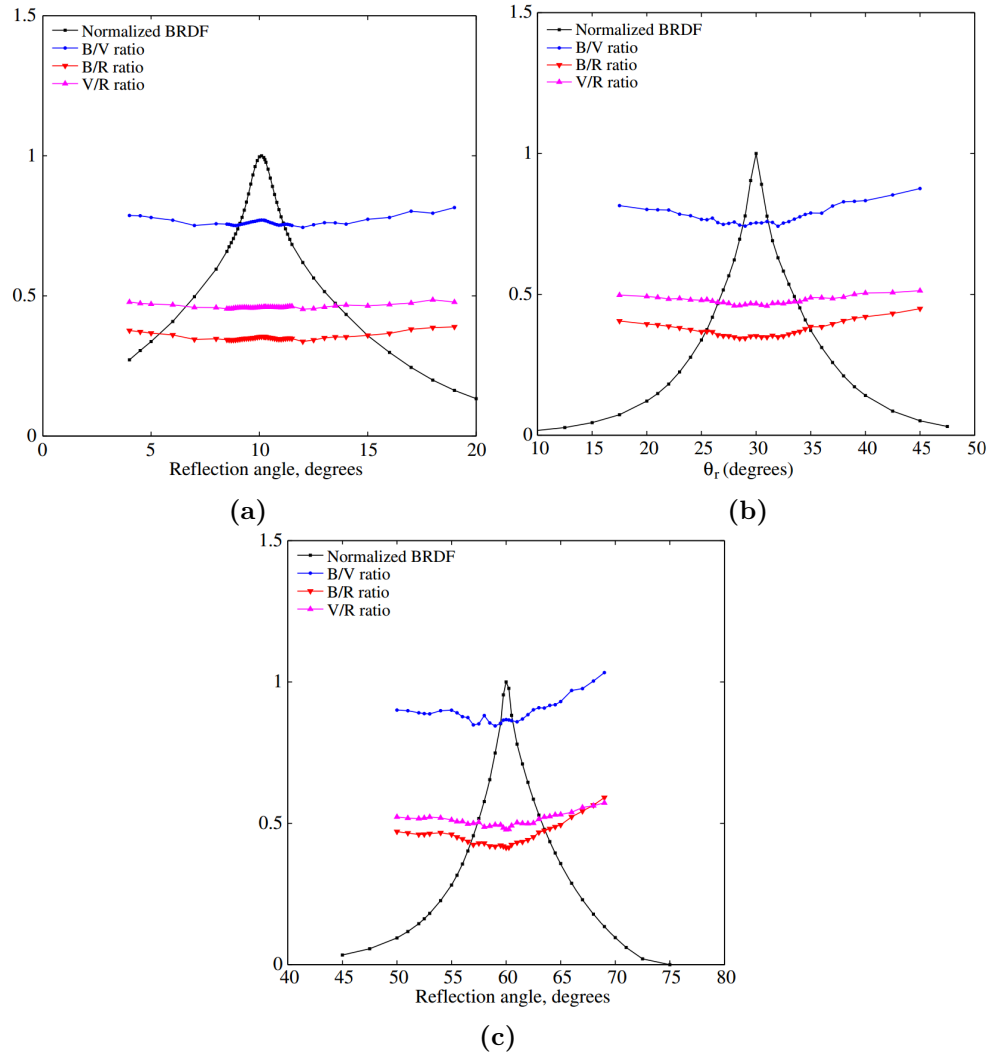


**Figure 2.11:** The normalized broadband BRDF and colour ratios of 6061-T6 aluminum alloy for (a)  $\theta_i = 10^\circ$ , (b)  $\theta_i = 30^\circ$ , and (c)  $\theta_i = 60^\circ$ . (Source: Bédard, 2013)[30]

# 3 Literature Survey

This chapter presents an overview of previous attempts to produce simulated imagery and physical quantities for the purposes of unresolved spacecraft characterization. These attempts were studied to determine the best approach to model spacecraft reflectance. The first section of this chapter defines three BRDF model categories and provides examples of each. It should be noted that none of these BRDF models were used as a part of this research project. They are presented only to develop an understanding of their function and because they are referred to when analyzing previous attempts of spacecraft reflectance modelling. Features and products of these systems are investigated in order to determine which approach should be taken to develop an accurate synthetic spacecraft ground truth system, the objective of this research project. The chapter concludes by presenting the approach to develop said system, and is followed in Chapter 4.

## 3.1 BRDF models

The number of BRDF model examples provided in this section are only the ‘tip of the iceberg’, though they do provide a conceptual basis for the variety available. Most BRDF models have been developed to describe the reflectance of a specific type of material and must therefore be combined with others to represent the overall reflectance of objects composed of multiple materials. The few BRDF models described in detail in this section were chosen as they were employed in previous attempts to simulate spacecraft reflectance, which are described in Section 3.2. See the synopsis produced by Montes and Ureña [32] for a more complete analysis of BRDF models.

Material BRDFs are incredibly complex and require considerable system resources when implemented in computer algorithms [35]. BRDF models have been developed in order to simplify these functions, making them more efficient to use. The properties that are desirable in a model are those that make the

model realistic and reliable, described in Table 3.1 [32].

Property	Description
Physically plausible	No physical laws, such as the conservation of energy, are broken
Expressive	Parameters allow for adjustment of the model
Usable	Able to represent multiple materials
Realistic	Close to BRDF functions that are exhibited in nature
Efficient	Computationally-conservative
Accurate	All components of reflection are represented without oversimplification

**Table 3.1: The desired properties of BRDF models.**

A significant number of BRDF models have been developed, predominantly for use in the field of computer graphics [31–33, 35–37]. They can be organized into three general categories: theoretical, experimental, and empirical.

### 3.1.1 Theoretical BRDF models

*Theoretical* BRDF models use physical laws to simulate the propagation of light. They require greater computational power when rendering scenes as a result [32]. Figure 3.1 provides a visualization of the many theoretical BRDF models and their sub-classification. Three of these models are described here, specifically chosen as they are utilized by systems presented later in this literature survey.

The first theoretical BRDF model is that of an *ideal-diffuse*, or *Lambertian* surface. It models a reflection type that has the same value for all incident and radiant directions. This type of reflection is shown in Figure 1.16 as uniform-diffuse. Light will be reflected equally in all directions by a Lambertian surface regardless of the direction from which it is incident. Equation 3.1 provides the formula for this BRDF model, where  $\rho_{ud}$  is the uniform diffuse reflectance [32].

$$f_r(\theta_i, \phi_i; \theta_r, \phi_r) = \frac{\rho_{ud}}{\pi} \quad [\text{sr}^{-1}] \quad (3.1)$$

A surface that only exhibits this type of reflection does not occur in nature, however, it most closely resembles materials where subsurface scattering, the

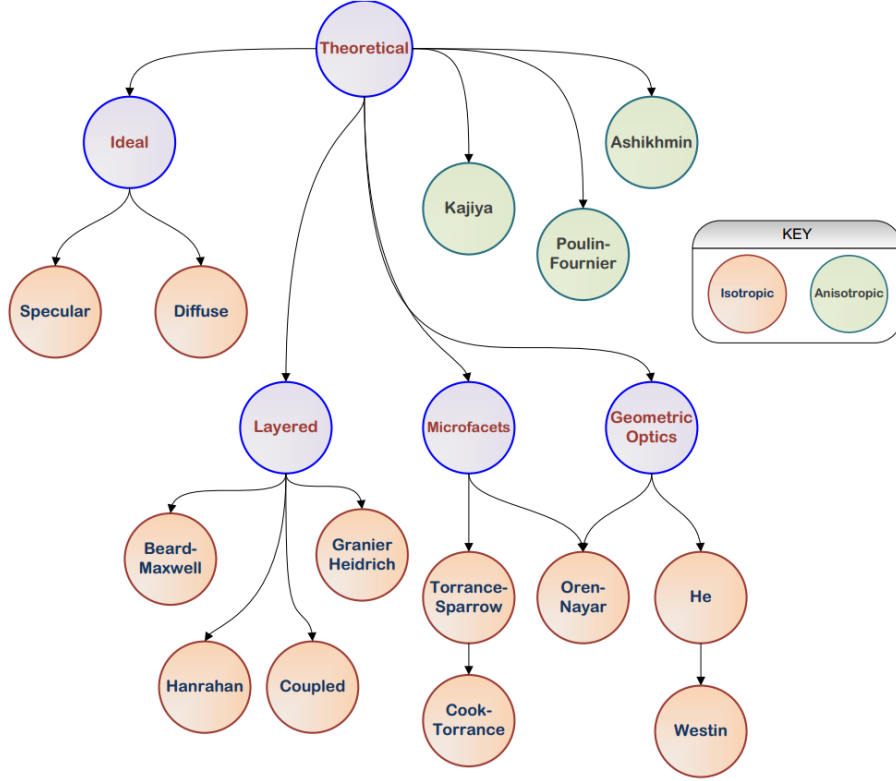


**Figure 3.1: A flow chart depicting all developed theoretical BRDF models. (Source: Montes, 2012)[32]**

scattering of light within the body of the material, dominates [33]. Most BRDF models use a Lambertian term to account for this effect [33]. This model is wavelength-independent and *isotropic*, signifying that the reflectance properties are identical in all directions.

The law of reflection describes how light is reflected by surfaces that are considered *ideal-specular*. Light will only be reflected in a direction that is in the same plane as and equal to  $\theta_i$ , and on the opposite side of  $\vec{N}$ . This second theoretical BRDF model is represented by a Dirac delta distribution,  $\delta$ , shown in Equation 3.2, where  $\rho_{sp}$  is the specular reflectance [32]:

$$f_r(\theta_i, \phi_i; \theta_r, \phi_r) = \rho_{sp}(\theta_i, \phi_i) \cdot \delta(\theta_i, \phi_i; \theta_r, \phi_r) \quad [\text{sr}^{-1}] \quad (3.2)$$

and  $\delta$  is expressed as:

$$\delta(\theta_i, \phi_i; \theta_r, \phi_r) = \begin{cases} \infty & \text{if } \theta_i = \theta_r \text{ and } \phi_i = 180^\circ - \phi_r \\ 0 & \text{else} \end{cases} \quad (3.3)$$

The wave nature of light allows for the existence of ideal specular reflectors in nature. This occurs when the surface roughness is smaller than the wavelength of light as it is considered optically smooth [33]. Accordingly, this model breaks down when the surface roughness is comparable to wavelength. Similar to Lambertian surfaces, this model is wavelength-independent and isotropic.

The final theoretical BRDF model presented here is the *Beard-Maxwell*, described by Equation 3.4, intended to specifically simulate painted surfaces by considering the combined contribution of a specular component produced by the top layer (the paint),  $f_{sp}$ , and a subsurface scattering component,  $f_{ss}$ , of the material below [36]:

$$f_r(\theta_i, \phi_i; \theta_r, \phi_r; \lambda) = f_{sp}(\theta_i, \phi_i; \theta_r, \phi_r; \lambda) + f_{ss}(\theta_i, \phi_i; \theta_r, \phi_r; \lambda) \quad [\text{sr}^{-1}] \quad (3.4)$$

where  $f_{sp}$  is expressed as:

$$f_{sp}(\theta_i, \phi_i; \theta_r, \phi_r; \lambda) = R_x(\beta_{1/2}) \cdot \frac{D(\vec{h})}{\cos(\theta_i) \cdot \cos(\theta_r)} \cdot SM(\theta_r, \phi_r, \vec{h}, \tau, \nu) \quad [\text{sr}^{-1}] \quad (3.5)$$

and  $f_{ss}$  is given by:

$$f_{ss}(\theta_i, \phi_i; \theta_r, \phi_r; \lambda) = \frac{2 \cdot \rho_v \cdot f(\beta_{1/2}) \cdot g(\theta_{\vec{N}})}{\cos(\theta_i) + \cos(\theta_r)} \quad [\text{sr}^{-1}] \quad (3.6)$$

where  $\vec{h}$  is the half vector located halfway between the illumination and reflection vector,  $\beta_{1/2}$  is the half-phase angle located between the half vector and illumination vector,  $x$  can be  $s$  or  $p$  for either polarization of light,  $R_x(\beta)$  is the Fresnel reflectance,  $D(\vec{h})$  is a micro-facet surface normal vector distribution function,  $SM(\theta_r, \phi_r, \vec{h}, \tau, \nu)$  is a shadowing and masking function,  $\rho_v$  is the maximum reflectance of the surface as viewed from the surface normal vector, and  $f(\beta)$  and  $g(\theta_{\vec{N}})$  are parameter functions that account for the possibility of specular reflection in the lower material. The model, as presented here, is in a global coordinate system, where the surface normal vector,  $\vec{N}$ , is at an angle,  $\theta_{\vec{N}}$ , to the global  $z$ -axis. Note that  $\tau$  and  $\nu$  are surface roughness characteristics, and along with  $\rho_v$ , are measured quantities [36].



The Beard-Maxwell model is wavelength-dependent as the index of refraction of the layered material, contained within the Fresnel reflectance, determines the direction in which light is scattered within. Due to consideration of the polarization of incident light, the model is isotropic. This model is known to decrease in accuracy for materials that are more specular [23] due to the subsurface scattering component [36]. The point at which this model breaks from measured results could not be found in the published literature and was not pursued as it was not used in this research project.

### 3.1.2 Experimental BRDF models

The second BRDF model category is *experimental*, depicted in the flow chart in Figure 3.2. Experimental BRDFs are those that have been acquired using a gonioreflectometer [37] or goniospectrometer [10]. These devices vary the illumination and observation geometries on a material sample to determine its reflectance properties. A gonioreflectometer uses a movable light source and photometer to achieve the four degrees of freedom required to measure BRDFs. A goniospectrometer works in much the same way but employs a spectrometer, allowing it to measure sBRDFs.

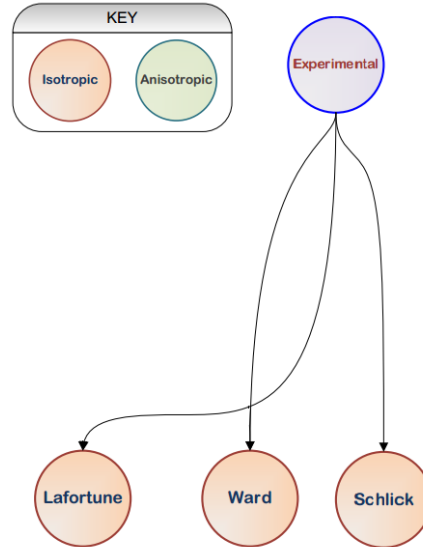


**Figure 3.2:** A flow chart depicting all developed experimental BRDF models. (Source: Montes, 2012)[32]

Long periods of time and complex setups are needed to acquire compre-

hensive experimental BRDFs of a single surface. These challenges are only compounded when measuring anisotropic materials since light is reflected differently depending on sample orientation [37].

### 3.1.3 Empirical BRDF models

*Empirical* BRDF models are designed to mimic a specific kind of reflection in a simple and computationally-conservative way. Based on experimental observations, they do not consider the physical laws responsible for reflection [32]. These models are presented in Figure 3.3 and contain some overlap with those in the experimental model category.

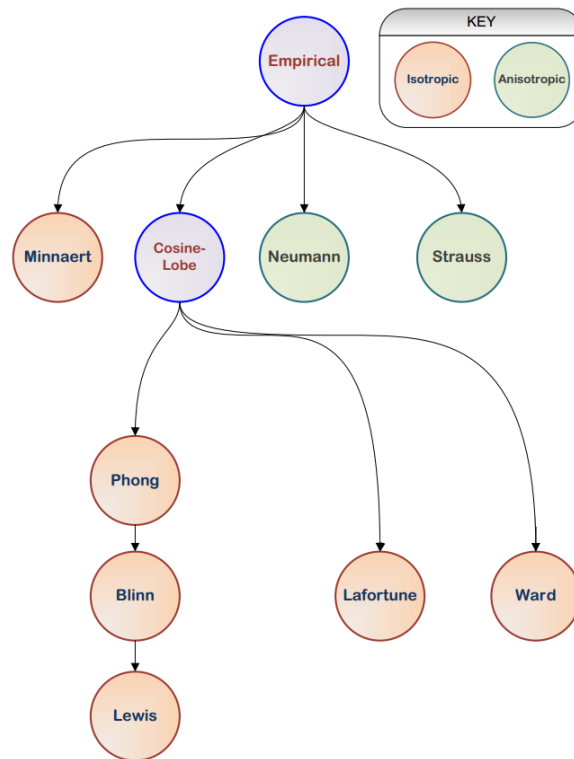


**Figure 3.3:** A flow chart depicting all developed empirical BRDF models. (Source: Montes, 2012)[32]

Ward [37] developed the first empirical BRDF model by fitting it to BRDFs obtained using a gonireflectometer. The resulting anisotropic BRDF model

is shown in Equation 3.7:

$$f_r(\theta_i, \phi_i; \theta_r, \phi_r) = \frac{\rho_{dd}}{\pi} + \rho_{sp} \cdot \frac{1}{\sqrt{\cos \theta_i \cos \theta_r}} \cdot \frac{e^{-\tan^2 \delta (\cos^2 \phi / \alpha_x^2 + \sin^2 \phi / \alpha_y^2)}}{4\pi \alpha_x \alpha_y} \quad (3.7)$$

where  $\rho_{dd}$  is the directional-diffuse reflectance,  $\alpha_x$  and  $\alpha_y$  are the standard deviations of the surface slope in the  $x$ - and  $y$ -directions,  $\delta$  is the angle between the half vector  $\vec{h}$  and the surface normal vector  $\vec{N}$ , and  $\phi$  is the azimuth angle of the half vector projected onto the surface plane, measured from the  $x$ -axis [37].

This model was developed by Ward to be used to describe reflectance measured by a gonireflectometer and is therefore wavelength-independent. It is considered computationally economical as it is relatively simple and models the BRDF of many isotropic and anisotropic materials [37].

As stated at the beginning of this section, these BRDF models are presented here as the understanding of their function is required in the following section. They are not utilized by the synthetic spacecraft ground truth system developed for this research project.

## 3.2 Previous attempts to model spacecraft reflectance

This section outlines several previous attempts to model the reflectance of spacecraft. It begins by describing two examples that use computer graphics rendering software to simulate light curves. Two modular systems specifically developed for spacecraft characterization used by the US scientific community are then provided. Lastly, a Canadian model that utilizes a numerical computing environment is described. Each model is assessed for its ability to accurately model spacecraft reflectance by analyzing its respective products. The approach of more successful systems was considered to develop the synthetic spacecraft ground truth system for this research project.

### 3.2.1 Simulating light curves using computer rendering software

In computer graphics the term *rendering* refers to the production of an image or scene from a description of the objects contained, including their material properties [35]. Most current cinemagoers are aware of the use of “computer-generation” to create photorealistic scenes and effects that would be difficult to achieve physically and financially. The possibility exists for this type of software to synthesize spacecraft reflectance. Two attempts to simulate light curves using computer graphics packages are presented, namely the employment of OpenSceneGraph by Früh [38] and the utilization of LuxRender by Arnold [39].

#### Früh and OpenSceneGraph

The first attempt at simulating spacecraft light curves using computer animation software was completed by Früh [38]. Light curves of simple Lambertian objects were simulated by rendering and animating these objects using OpenSceneGraph, an open-source 3D graphics toolkit [40]. Scenes were rendered with a light source representing the Sun and objects were located in a GEO ring with zero inclination. Observations were made in the same plane as this ring. Light curves were generated by integrating the object’s illuminated panels and calculating its visual magnitude based on its size and distance from the observer.

A cube, cylinder, and crinkled MLI structure were constructed for simulation, all modelled with a Lambertian BRDF. Only the cube, with a side length of 2 m, is presented here as it relates to this research project. The cube

was animated to rotate on its axis parallel to the observation plane with a period of 49 minutes. The phase angle was defined as  $90^\circ$  in the  $xy$ -plane and  $45^\circ$  in the  $xz$ -plane. The original orientation of the cube was not described. The resulting light curve is presented in Figure 3.4.

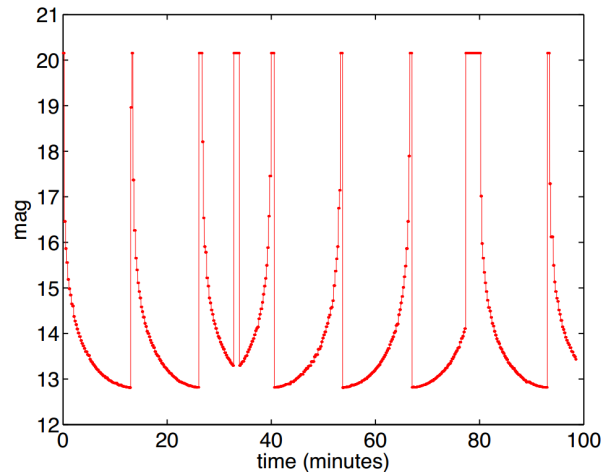


**Figure 3.4: The simulated light curve of a Lambertian cube with a rotation period of 49 minutes shown as visual magnitude versus time. Note that a lower visual magnitude indicates a brighter object. (Source: Früh, 2010)[38]**

It is unclear as to why the visual magnitude of the light curve appears to be bound between 13 and 20, or what can account for the sharp changes between these two values, as this was not discussed. Neither of these phenomena are typical of a cube's light curves as was shown by the characterization of the CanX-1 EM in Figure 2.4. The cube does exhibit four peaks in brightness within 49 minutes, from approximately the 35- to 80-minute mark, due to its rotational period, as expected.

The model by Früh [38] is able to produce light curves of simple objects possessing a Lambertian BRDF. The unexpected phenomena in these light curves leaves uncertainty in their validity. Light curves were not produced using more complex subjects with multiple BRDFs which would be required for spacecraft models. It is unclear if instantaneous spacecraft spectra could be extracted from OpenSceneGraph. Based on this analysis the utility of this software to accurately synthesize spacecraft reflectance remains in question. That said, its ability to produce visual magnitude is an attribute that should be considered when simulating light curves as this is a quantity that can be

directly compared to optical measurements.

#### **Arnold and LuxRender**

The second attempt at simulating light curves using computer animation software was completed by Arnold [39]. The rendering engine used was LuxRender, considered to be “unbiased and physically-based [as it] does not introduce systematic error into the radiance approximation and uses full spectra for internal calculations” [41]. Images were generated by rendering a scene in which a solar spectrum was attached to a distant light source and propagated through an atmosphere-less medium in order to accurately model the Sun-spacecraft-observer geometry.

LuxRender’s output format is Red-Green-Blue (RGB)-defined photorealistic images, intended for display on a computer monitor. Brightness data had to be extracted from these images for light curves to be produced. The RGB values were converted to Hue-Saturation-Lightness (HSL), where only the pixel *lightness*, associated with the magnitude of the pixel’s dominant wavelength of light, was used to define the total flux. All spectral data was lost as a result.

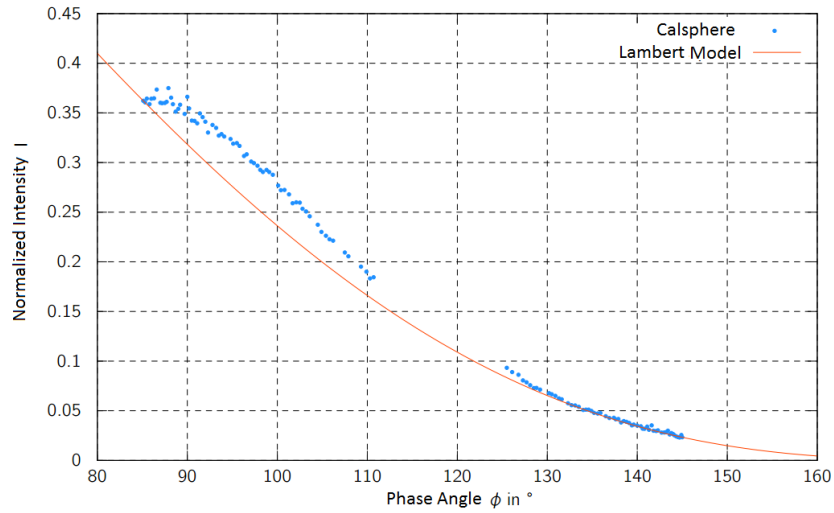
A light curve function of a Lambertian sphere was initially fit to the normalized measured intensity of a spherical satellite, the Calsphere-4A, to establish the Lambertian nature of the spacecraft. Figure 3.5a shows the result of this fit. Next, the normalized simulated intensity of a rendered Lambertian sphere with similar characteristics as Calsphere-4A was plotted alongside the same light curve function, provided in Figure 3.5b.

There is agreement between the function and observed intensities of Calsphere-4A, indicating that it does represent a Lambertian sphere. Similar agreement with the rendered BRDF model was not obtained. This was due to a contrast-clipping effect built into the LuxRender software, which optimizes images for viewing on a computer screen.

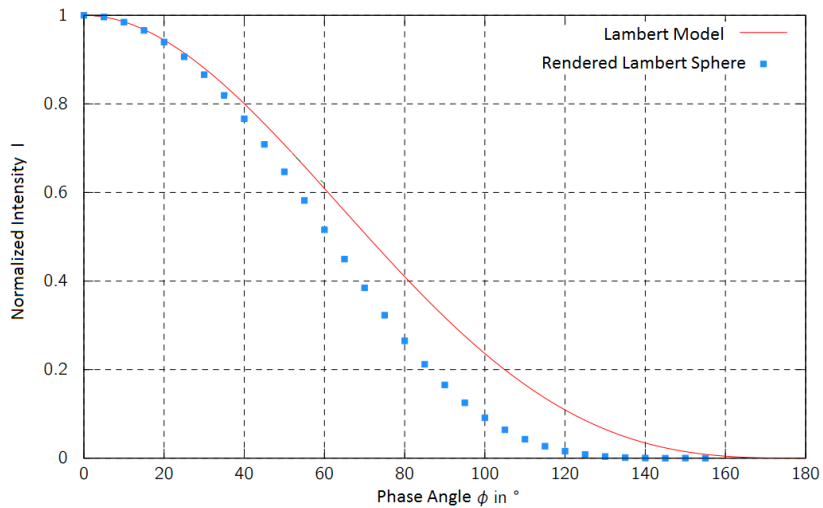
While Arnold [39] went on to simulate light curves of spheres using a variety of BRDF models, representing different materials and coatings, it was clear that LuxRender is unsuitable for the modelling of spacecraft reflectance and further analysis was not required. The results are not spectral in nature as they are produced specifically for visualization on computer screens and the accuracy of data after conversion and extraction is questionable.

Simulating light curves using computer animation software does not appear promising after analysis of these two attempts. These software packages possess a steep learning curve, require overly complex scene setups, and are intended to be used for artistic purposes, producing imagery that while ap-

### 3.2. Previous attempts to model spacecraft reflectance



(a)



(b)

**Figure 3.5:** (a) A comparison of the normalized intensity as a function of phase angle of Calsphere-4A with that predicted by a Lambertian light curve function, and (b) a comparison of the normalized intensity as a function of phase angle of a rendered Lambert sphere versus the same function. Note the different ranges of the horizontal scale. (Source: Arnold, 2011)[39]

pearing photorealistic does not contain useful spectral data. The production of light curves as a function of visual magnitude is possible using synthetic spacecraft ground truth, however, this is not required for this thesis. This product will be considered for future expansion of the system developed for this research project.

#### **3.2.2 Simulating spacecraft reflectance using TASAT**

The Time-domain Analysis Simulation for Advanced Tracking (TASAT) system was designed at the US Air Force Research Laboratory (AFRL) to simulate tracking and imaging systems to assess system performance and design [42]. It is a modular set of routines that model ground-based and space-based systems, considering the relative geometry between the illumination source, target, and observer, as well as the correct absolute radiometry, atmospheric effects, and sensor capabilities [23]. TASAT is capable of producing physically-accurate images of complicated subjects such as CAD models, provided knowledge of the BRDFs of their surface materials.

It should be noted that TASAT is not available in the public domain. While unavailable to the author, its existence provides proof of concept for the appropriate design and function of a spacecraft reflectance modelling system. The lack of availability also implies that the validity of TASAT has not been subjected to peer review and details regarding its strengths and weaknesses are not known.

TASAT has been used to model spacecraft reflectance in multiple studies, two of which are provided here. These include the generation of spacecraft spectra using material class reflectance by Luu et al. [6] and the identification of spacecraft materials from unresolved spectra by Hall et al. [43].

#### **Luu and generating spacecraft spectra using material class reflectance**

Luu et al. [6] used TASAT to generate a spacecraft's spectra using its CAD model and material class reflectance data. The materials included in this study were a collection of solar cells, white paints, aluminum, and MLI. Their reflectance was modelled by averaging the spectral traces obtained from four different sources including the TASAT satellite materials database, the Environmental Research Institute of Michigan, the AFRL Satellite Assessment Center, and Jorgensen [44]. The spectral traces of thirty solar cells, ten white paints with different finishes, and eight aluminum samples with different fin-



ishes, along with their means and standard deviations, are shown in Figure 3.6. The spectral traces of MLI were also presented but are not included here.

The reflectance of the Galaxy V spacecraft was observed seven times over the course of one evening. A TASAT simulation was run for the same scenario using a CAD model of the satellite and the averaged material reflectances. A comparison of normalized results is provided in Figures 3.7a and 3.7b. Particular attention needs to be made when comparing the two plots as their axes are scaled differently.

The measured Galaxy V reflectance spectra vary over time. Some observations exhibit spectral features that are absent in others. The TASAT simulated spectra are devoid of these features. It is difficult to visually determine how closely the simulated and measured spectra agree due to their presentation and no quantitative analysis was provided. There is little variation between the simulated spectra and there are no differentiating spectral features. This makes it difficult to tell that there are seven spectra located in Figure 3.7b.

The model developed by Luu et al. [6] is inaccurate as it relies on a limited material reflectance database. This database is comprised of averaged spectral traces representing entire classes as opposed to individual materials. As was shown in Section 2.2 each material's reflectance contains characteristic spectral features which are lost by being averaged with others. Also, the reflectance quantity presented in Figure 3.6 will not vary with changes in spacecraft orientation as it is not a function of illumination and observation geometry. This is inaccurate as intensities change and spectral features may shift with changing illumination angle. Based on this analysis it is clear that this system does not accurately model the reflectance of spacecraft, however, its demonstration of the use of CAD models and production of high fidelity spectra are both desired features that were incorporated into the the system developed for this research project.

#### **Hall and the production of range-normalized light curves**

Hall et al. [43] investigated the possibility of identifying spacecraft surface materials using unresolved multi-band optical observations. The observations were simulated using TASAT to produce results similar to those expected from ground-based optical sensors.

The Beard-Maxwell model was empirically fit to material BRDFs contained in the TASAT database. Figure 3.8 depicts the BRDF plots of white paint and aluminum for a wavelength of 600 nm and an undefined illumination angle. A plot of MLI was also presented but is not included here. The

### 3.2. Previous attempts to model spacecraft reflectance

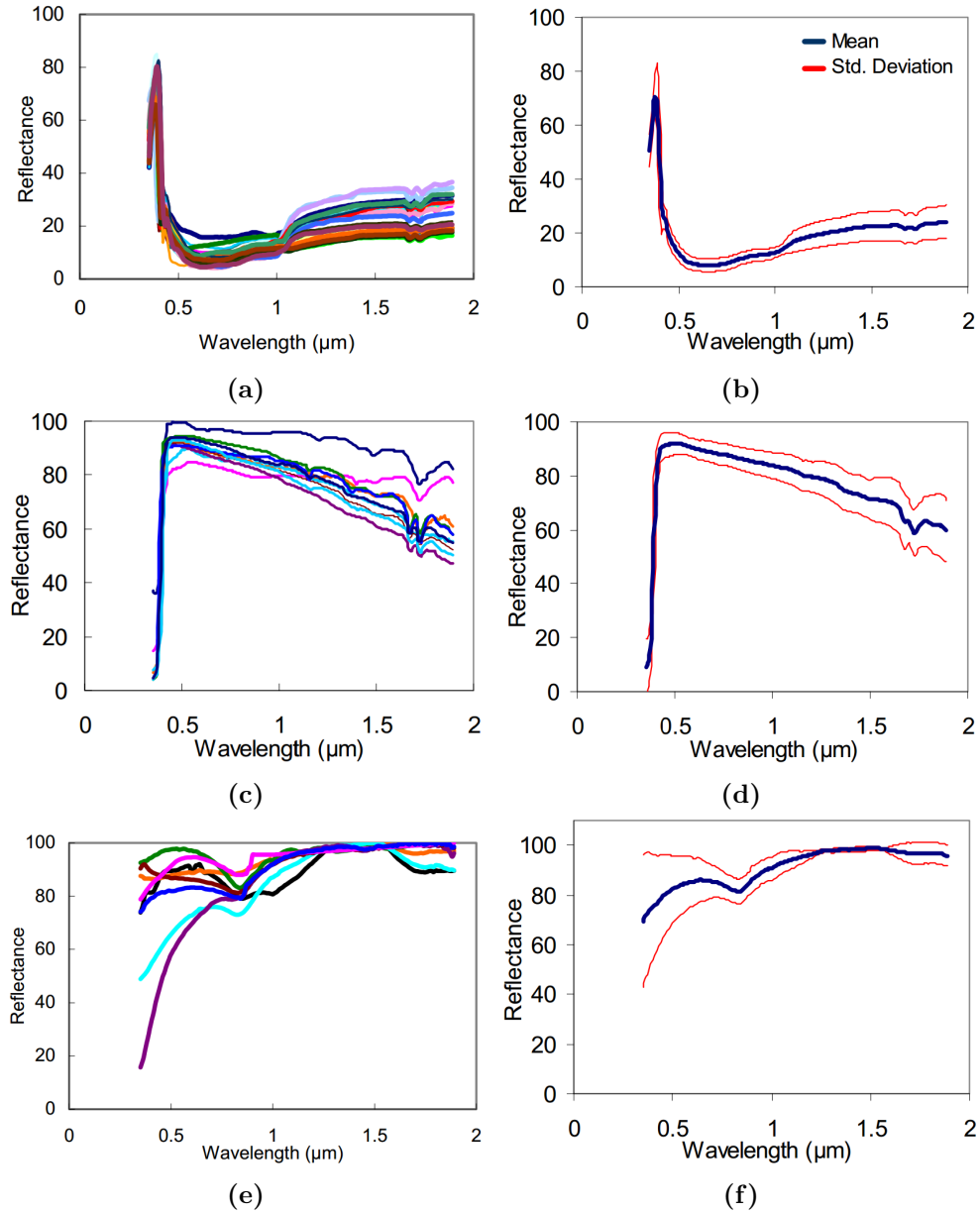
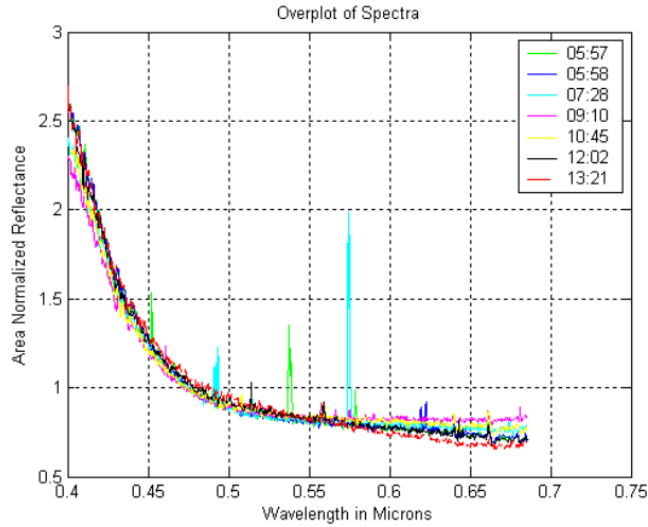
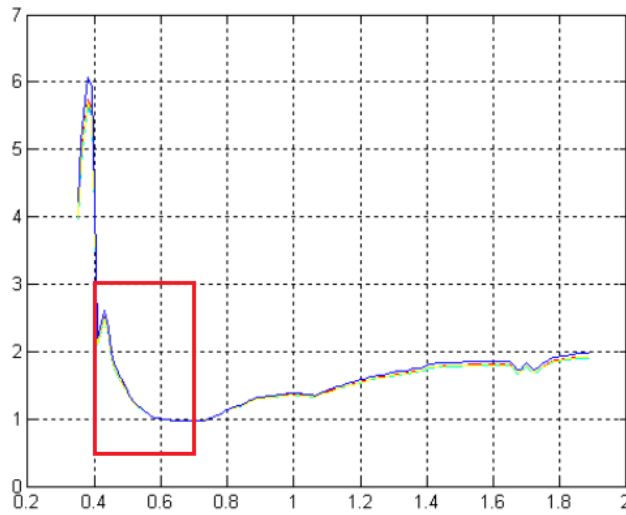


Figure 3.6: Spectral traces of (a) solar cells, (c) white paints, (e) and aluminum. The mean spectral traces of these materials and their standard deviation are shown adjacent in (a), (d), and (f), respectively. (Source: Luu, 2003)[6]

### 3.2. Previous attempts to model spacecraft reflectance



(a)



(b)

**Figure 3.7:** (a) Seven observed reflectances as a function of wavelength of Galaxy V in March 2003, normalized and overlaid. (b) The simulated TASAT spectra for the same seven observation scenarios of Galaxy V. The highlighted region is that of the plot in (a). (Source: Luu, 2003)[6]

### 3.2. Previous attempts to model spacecraft reflectance

hemispherical reflectance of each material is also shown for a wavelength between 400 nm and 1200 nm though discontinuities are present. These were unexplained, and their presence suggests inaccurate reflectance data. Further investigation was not conducted as it was not relevant to this research project. It is unclear how BRDFs and hemispherical reflectance were used in this study, though Hall et al. [43] stated that “the importance of the wavelength-dependent BRDF cannot be overemphasized.” There was no mention of how many geometries were contained within the TASAT material BRDF database suggesting the Beard-Maxwell model was fit to the single BRDF in Figure 3.8.

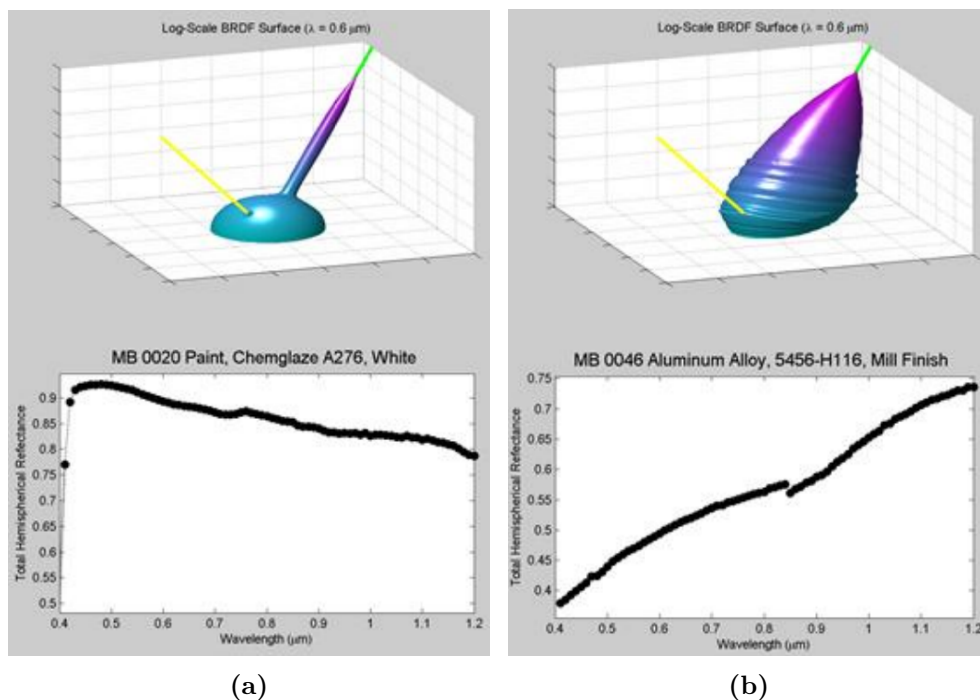


**Figure 3.8: The Beard-Maxwell BRDF models for a wavelength of 600 nm and unknown illumination angle, and hemispherical reflectance of (a) white paint, and (b) milled aluminum. (Source: Hall, 2012)[43]**

Range-normalized light curves were simulated for six wavebands using a CAD model of a box-wing satellite comprised of a tube pointing to nadir and solar panel struts aligned with the spacecraft velocity vector. Figure 3.9a shows the simulated light curve in the 800 nm band in range-normalized stellar magnitudes as seen from the Air Force Maui Optical Site (AMOS) observatory.

The amount of reflected optical flux, known as the optical cross-section (OCS), of each waveband is shown in Figure 3.9b.

The magnitude of the satellite’s OCS varied differently for each waveband over time. This is a result of the changing spacecraft orientation as it followed its orbit and is indicative of the geometric consideration of the Beard-Maxwell model. The fidelity of the spectra is low as the optical region is divided into nine wavebands. Actual observations of a spacecraft in a similar scenario were not provided leaving the accuracy of the produced light curve in question.

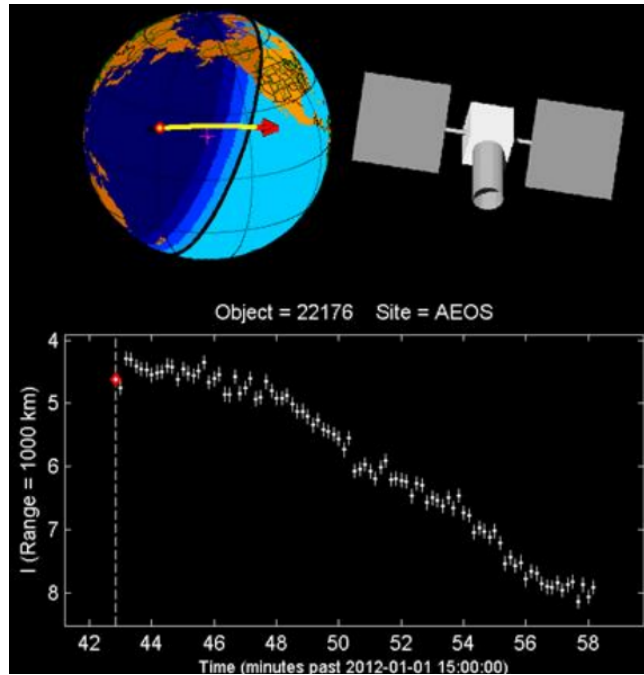
The model by Hall et al. [43] remains invalidated. The change in OCS with change in spacecraft illumination and observation geometry indicates that intensities change and spectral features shift with changing illumination angle, as was shown in Section 2.2. Its material database is spectral as it is based on the Beard-Maxwell BRDF model, however, it is unclear how many measurements the TASAT material database contained with which to fit this model. This leaves uncertainty with regards to the spectral feature behaviour associated with the illumination angle. In addition, the resulting spacecraft spectra possess low fidelity and would not be useful for material characterization, when compared to the spectral features in the material sBRDFs in Section 2.2. Based on this analysis it is unclear whether this model accurately models the reflectance of spacecraft.

These two examples have demonstrated TASAT’s limited ability to model spacecraft reflectance as it relates to this research project. The most apparent weakness of the system lies in its material BRDF database which has not been subjected to peer review. Its use of spacecraft CAD models and production of spectra are two features that should be considered when developing a synthetic spacecraft ground truth system.

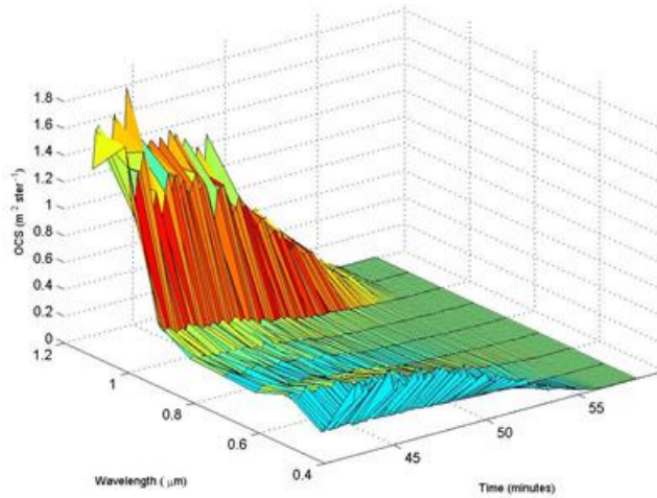
#### 3.2.3 Producing radiometric images using DIRSIG

Another software package that has been used to model spacecraft reflectance is the Digital Imaging and Remote Sensing laboratory’s Image Generation (DIRSIG) system, developed by the Digital Imaging and Remote Sensing laboratory at the Center for Imaging Science. DIRSIG produces radiometric images that are spectral in nature with radiance ranging from the visible to long infrared [45]. It is a collection of data input files and sub-models originally designed to simulate remote-sensing imagery, emphasizing the inclusion of radiometric processes that affect spectral image formation. DIRSIG is capable of rendering images of arbitrarily complicated surface shapes such as CAD models given the BRDFs of their component materials.

### 3.2. Previous attempts to model spacecraft reflectance



(a)



(b)

Figure 3.9: (a) The ground track, spacecraft CAD model, and range-normalized light curve in the 800 nm band. (b) The multi-band OCS values for nine bands and a 20 min timescale. (Source: Hall, 2012)[43]

### 3.2. Previous attempts to model spacecraft reflectance

DIRSIG obtains spacecraft two-line-element (TLE) files from Analytical Graphics, Inc. (AGI)'s Satellite Tool Kit (STK) software in order to construct scenarios. Component articulation data is also included, allowing for the movement of solar panels to track the Sun or a communications dish pointing to a ground station.

DIRSIG is not available in the public domain as users must be employees of a US government organization or contractor, or attending universities performing related research, and must also attend a training class [46]. Again, due to limited access, the implication is made that the validity of DIRSIG has not been subjected to peer review, and details regarding its strengths and weaknesses are not known.

An example of modelling spacecraft reflectance using DIRSIG was recently published by Bennett et al. [47]. Material BRDFs, measured in a Lockheed Martin laboratory, were empirically fit to the Ward BRDF model. The measured BRDF of a solar cell along with its fitted Ward model are presented in Figure 3.10. Models of gold kapton, silver scrim MLI, and optical solar reflector (OSR) were also presented but not included here. The Ward model does not appear to accurately represent the measured BRDF of the solar cell. It is also questionable if the Ward BRDF kept its wavelength-dependance as it is presented as a function of degrees-off-specular, leaving the spectral nature of the modelled material BRDFs unknown. Bennett et al. [47] indicated that in order to better represent material reflectance they “are working toward using [BRDF] measurements directly without having to use a fit model”, though further details were not provided.

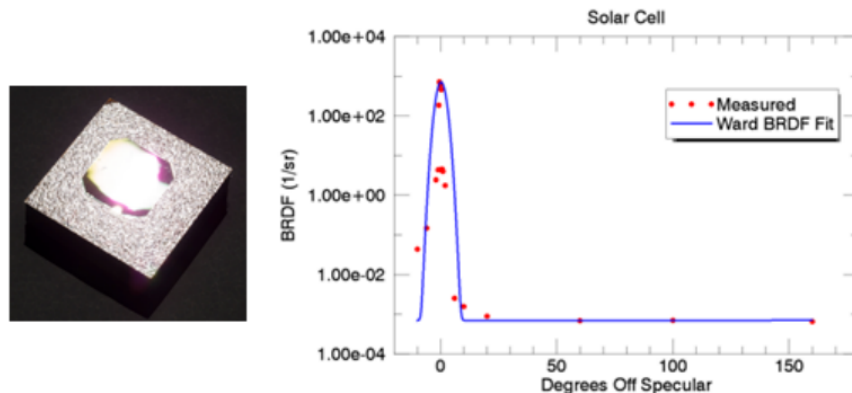
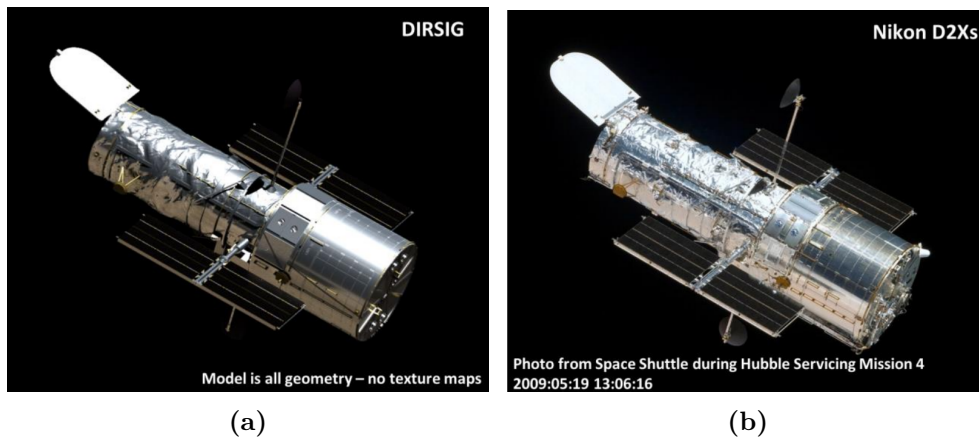


Figure 3.10: The Ward BRDF model fit to the measured BRDF of a solar cell. (Source: Bennett, 2014)[47]

### 3.2. Previous attempts to model spacecraft reflectance

A faceted engineering-quality CAD model of the Hubble Space Telescope (HST) was used to demonstrate DIRSIG’s ability to produce radiometrically-accurate images. Applying material definitions to the flat surfaces was standard, however, wrapping and wrinkling the MLI was accomplished using a “collision” mesh and randomizing the displacement of individual facets [47]. A generated radiometric image of this model is shown in Figure 3.11a along with a photo taken from a space shuttle during the fourth Hubble servicing mission in Figure 3.11b [47].



**Figure 3.11: The HST seen in a (a) DIRSIG generated image, and (b) photo. (Source: Bennett, 2014)[47]**

The use of DIRSIG by Bennett et al. [47] provided qualitative verification of the system’s capability to model spacecraft reflectance to produce radiometric images. Unfortunately, no spectra were produced as part of the simulation leaving its quantitative accuracy unvalidated. It is unclear whether spectra could be produced by DIRSIG in its current form. The modelling of MLI wrinkling should be considered for the construction of spacecraft CAD models as it appears to mimic the physical nature of the material quite well. The future goal of using directly-measured BRDFs instead of fitting them to models is the most noteworthy conclusion reached during this study and was a strong influence for the reasoning to avoid using BRDF models during the research project. Based on this analysis it remains unclear whether this model accurately models the reflectance of spacecraft, however, its feature to import TLEs should be considered for incorporation into the synthetic spacecraft ground truth system.



### 3.2.4 Light curve simulation in a numerical computing environment

The final model that is presented was developed by Scott et al. [48] to simulate light curves of unresolved spacecraft performing on-orbit servicing in the GEO belt. This system is based in Matlab, a numerical computing environment, and simulates light curves using triangular-faceted CAD models and ephemeris data from STK.

The measured BRDFs of six materials for normal incidence illumination were obtained from the AFRL's unpublished materials database [49]. These are shown in Figure 3.12 and do not appear spectral in nature. As they were unpublished their validity remains in question. Regardless, these were fit to an unspecified cosine-lobed BRDF model. It is unclear which of the materials were applied to the simple box-wing satellite CAD model used for simulation.

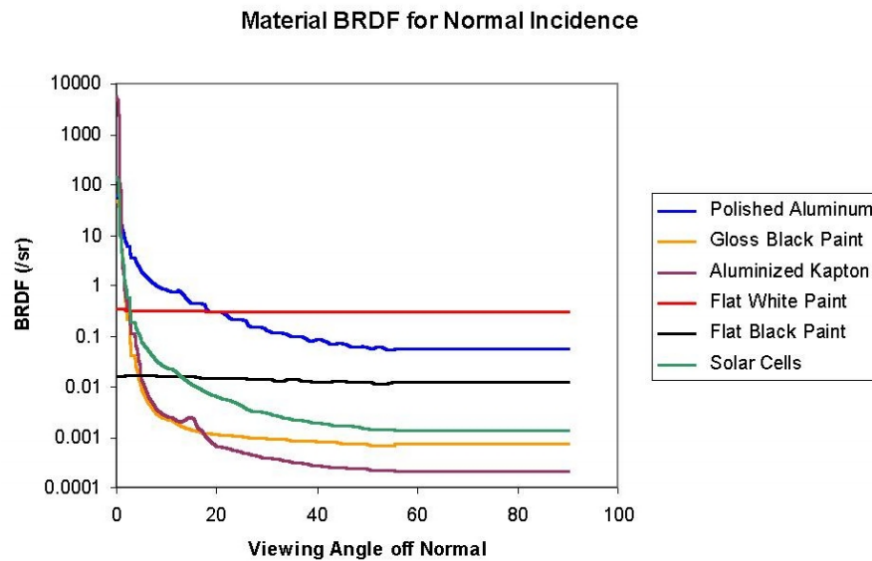


**Figure 3.12: Six material BRDFs for normal incidence. (Source: Ackermann, 2005)[49]**

Figure 3.13a presents a simulated light curve for an observation of the model at minimum phase angle, depicting solar panel glint. A measured light curve of M-Sat 1, a similarly-shaped spacecraft, is provided in Figure 3.13b for comparison. Note the difference in units on the horizontal axis. Unfortunately, observations at minimum phase angle are difficult to obtain as the spacecraft is shadowed by the Earth. The shape of the observed light curve is vaguely

seen in the simulated one, however, the glint is absent. No other light curves were simulated that could be used to further analyze the model.

While the validity of the system itself remains in question due to the unknown nature of the BRDFs and BRDF model, Scott et al. [48] have demonstrated that it is possible to model spacecraft reflectance in a numerical computing environment. This system is able to utilize spacecraft CAD models, STK ephemeris data, and material BRDFs to simulate light curves. Based on this analysis its approach was the most appealing and was therefore a strong influence towards the development of the synthetic spacecraft ground truth system for this research project.

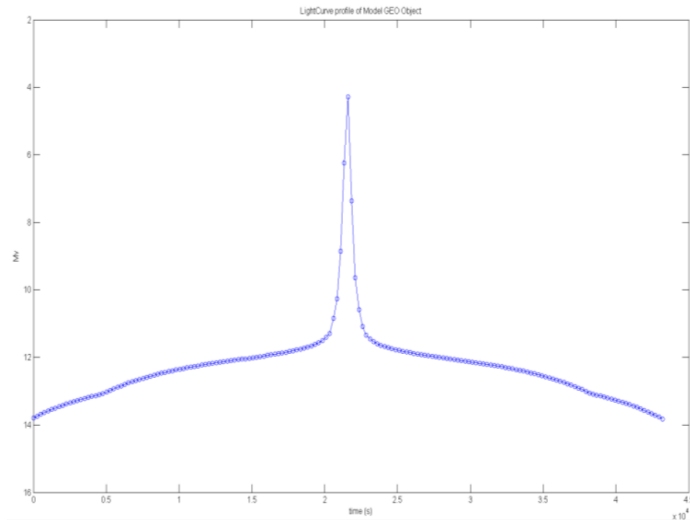
#### **3.2.5 Approach for a system to produce synthetic spacecraft ground truth**

This section has outlined a number of systems attempting to model spacecraft reflectance. Unfortunately, most of them have been shown to be limited in this capability for a number of reasons. The credibility of most systems was negatively impacted as they were presented without adequate description. Fortunately, the lessons learned from their shortcomings were used to develop an approach to achieve the goal of this research project: to produce synthetic spacecraft ground truth.

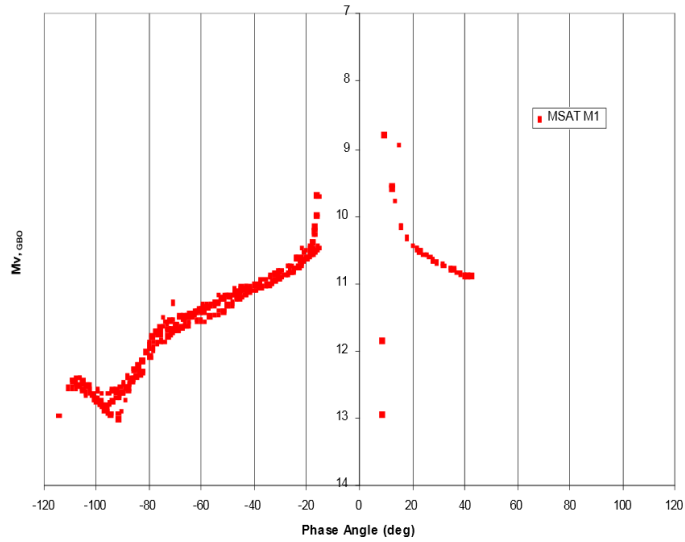
Almost all of these systems fell short on their ability to accurately represent the reflectance of materials. The material BRDFs they used were not fully understood, not spectral, or fit to empirical BRDF models that oversimplified the relationship with illumination and observation geometry. Systems must have access to a comprehensive BRDF database, containing characteristic spectral features and how they change with geometry, for all simulated materials. Therefore, in order to accurately synthesize spacecraft ground truth for this research project, it was decided that the measured sBRDFs of homogeneous spacecraft materials would be used as the foundation for a comprehensive database and the use of BRDF models would be avoided.

One common feature of most systems was the use of CAD models to represent spacecraft. While their composition was not typically discussed in detail, one study specifically mentioned that the CAD model was comprised of triangular facets. Upon review it was determined that the use of triangular facets would enable spacecraft to be represented by three-dimensional matrices, allowing for the system to be based in a numerical computing environment. It was also discovered that this was a common output format of most CAD software packages. The use of triangular-faceted models was chosen as the most effective approach to represent spacecraft.

### 3.2. Previous attempts to model spacecraft reflectance



(a) (Source: Scott, 2011)[48]



(b) (Source: Scott, 2008)[8]

Figure 3.13: (a) Simulated light curve depicting solar panel glint, and (b) measured light curve of M-Sat 1. Note the difference in units on the horizontal axes.

### 3.2. Previous attempts to model spacecraft reflectance

---

Finally, the products of the systems analyzed here include radiometric and photo-realistic images, photometric light curves, and spacecraft spectra. The objective of this research project is to produce synthetic ground truth of spacecraft, represented by their sBRDF. Accomplishing this will allow for the production of BRDFs, colour-filtered BRDFs, colour ratios, reflectance spectra, and spectrometric light curves. All of these quantities are useful for the purposes of unresolved spacecraft characterization. Due to the fact that the simulation of imagery is not useful for optical SSA, this will not be attempted.

# 4 The Synthetic Spacecraft sBRDF System

This chapter presents the system used to produce a spacecraft’s synthetic sBRDF, a quantity useful for ground truth characterization, and the subsequent production of BRDFs and colour ratios. It begins by making additions and changes to predefined terms, angles, and equations as required for the development of a comprehensive material reflectance database and sBRDF-synthesizing mathematical algorithm. A description of the development of material sBRDF look-up tables using measured data is provided, followed by the representation of spacecraft using triangular-faceted CAD models. Finally, the creation of scenes, synthesis of overall spacecraft sBRDF, and the production of BRDFs and colour ratios is explained.

## 4.1 Redefinition and modification of angles

The angles defined in Section 1.3.1 required some modifications for the purposes of this research project. Most important was the introduction of the *observer*, the perspective for which the spacecraft sBRDF was being synthesized. This section first redefines some reflection angles as observation angles. It then presents the modification of some angles to promote the development of the comprehensive material sBRDF database and system that relied upon it. A modified sBRDF as a function of these new angles is then presented.

### 4.1.1 Redefining reflection angles

Light is reflected in multiple directions, considering the different reflection components, meaning there can be multiple values of the reflected polar and azimuth angles,  $\theta_r$  and  $\phi_r$ , for a single illumination vector. Since the objective was to synthesize the overall sBRDF of a spacecraft as viewed by an observer the reflection vector was substituted with an observation vector. This resulted

in only one  $\theta_o$  and one  $\phi_o$  for the observation vector. The reflection angles were relabelled as observation angles, denoted by a subscript  $o$ , in order to account for this change. The illumination and observation angles of interest to this research project are shown in Figure 4.1.

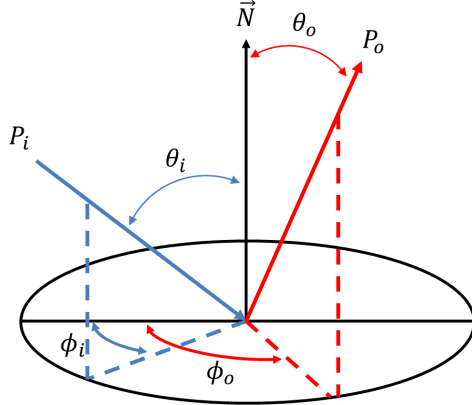


**Figure 4.1: The illumination and observation angles of interest to this research project.**

Note that the solid angles,  $\omega_i$  and  $\omega_o$ , are not required for this algorithm since the sBRDF is not dependant on them. They are used to determine the amount of flux impinging on the surface or being collected by the detector, respectively. These are both quantities that are not of interest to this research project. Their incorporation is suggested as future work, allowing for the production of spectrometric light curves.

#### 4.1.2 Modifying the illumination and observation angles

The set of illumination and observation angles required two modifications. These were necessary to develop a comprehensive sBRDF look-up table using limited laboratory measurements, and for the mathematical algorithm of the synthetic sBRDF system to access this database.

The first modification was made to the illumination and observation azimuth angles,  $\phi_i$  and  $\phi_o$ . The calculation of both angles requires the definition of an axis in the surface plane from which both are measured. This axis may be arbitrarily defined making the azimuth angles relative. The difference between them,  $\Delta\phi$ , is therefore a more useful quantity and is calculated using

Equation 4.1.

$$\Delta\phi = \phi_o - \phi_i \quad (4.1)$$

This *difference-in-azimuth* angle is shown in Figure 4.2 and is indicative of whether  $\theta_o$  is in the plane defined by  $\theta_i$ . A  $\Delta\phi$  value of  $0^\circ$  or  $180^\circ$  means  $\theta_o$  is in-plane, while all other values indicates that it is off-plane. All material sBRDF measurements in Section 2.2 were made with a  $\Delta\phi$  value of  $180^\circ$  as  $\theta_o$  was in-plane and on the opposite side of  $\vec{N}$  from  $\theta_i$ .

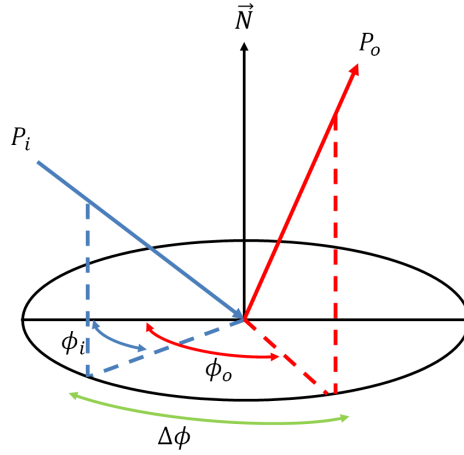


**Figure 4.2:** The difference between the illumination and observation azimuth angles,  $\Delta\phi$ .

The second modification was to convert  $\theta_o$  to the equivalent *angle-off-specular*,  $\theta_{os}$ , assuming that  $\theta_o$  is in-plane. This assumption is maintained for the remainder of the thesis, however, in real-world scenarios  $\theta_o$  is often off-plane. The angle-off-specular is shown in Figure 4.3. The conversion is performed using Equation 4.2, where  $\theta_i$  is equivalent to the polar angle of the specular component of reflection. Note that  $\Delta\phi$  determines how  $\theta_{os}$  is calculated.

$$\theta_{os} = \begin{cases} -(\theta_o + \theta_i) & \text{if } \Delta\phi = 0^\circ \\ (\theta_o - \theta_i) & \text{if } \Delta\phi = 180^\circ \end{cases} \quad (4.2)$$

A negative value of  $\theta_{os}$  therefore indicates that the phase angle,  $\beta$ , is less than  $2\theta_i$ , and a positive value indicates that  $\beta$  is greater than this value.

After making these two modifications, the sBRDF is redefined as a function of the new angles,  $f_r(\theta_i; \theta_{os}; \Delta\phi; \lambda)$ .

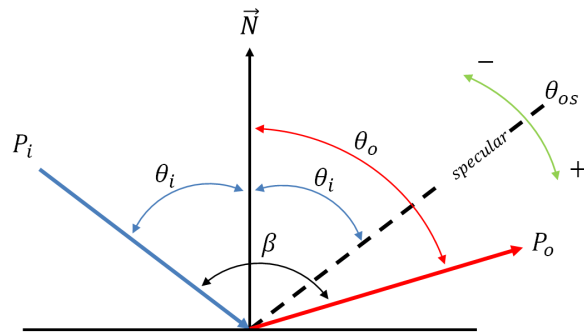


**Figure 4.3:** The relationship between  $\theta_i$ ,  $\theta_o$ , and  $\theta_{os}$ .  $\beta$  is included for interpretation. Note that all angles depicted here are in the same plane.



## 4.2 A material reflectance database

This section explains how the measured material sBRDFs were developed into a reflectance database containing comprehensive look-up tables that would be used by the synthetic spacecraft sBRDF system. This format eliminated the necessity to use one of the defined BRDF models in Section 3.1 which have demonstrated limitations in past attempts at modelling spacecraft reflectance. This ensured that material reflectance properties were maintained while meeting the desired properties outlined in Table 3.1. This section describes the original sampling of the material sBRDFs and how the look-up tables were developed for all  $\theta_i$  and  $\theta_{os}$ , thereby establishing them as “comprehensive” for the purposes of this research project.

### 4.2.1 Measured material sBRDFs

A total of nine measured sBRDFs were obtained from the experiment performed by Bédard et al. [30] outlined in Section 2.2. These included three of 6061-T6 aluminum alloy, three of Emcore TJPV cell, and three of Lord Aeroglaze 276A reflective white low-outgassing paint. The illumination angles, observation angle ranges, and observation angle increment ranges,  $\Delta\theta_o$ , for these measurements are shown in Table 4.1.

Material	$\theta_i$ [°]	$\theta_o$ [°]	$\Delta\theta_o$ [°]
6061-T6 aluminum alloy	10	3.0 – 30.0	0.1 – 1.0
	30	5.0 – 47.5	0.5 – 2.5
	60	40.0 – 72.5	0.1 – 2.5
Emcore TJPV cell	10	8.00 – 11.90	0.05 – 0.10
	30	28.00 – 32.00	0.05 – 0.25
	60	58.00 – 62.00	0.05 – 0.25
Lord Aeroglaze 276A reflective white low-outgassing paint	10	4.00 – 16.00	0.05 – 1.00
	30	22.00 – 38.00	0.05 – 1.00
	60	53.00 – 67.00	0.05 – 1.00

**Table 4.1: Illumination angles, observation angle ranges, and observation angle increment ranges for the nine measured material sBRDFs.**

The observation angles were distributed so the material sBRDF was measured across the entire reflected beam with no observed reflectance outside

of this range. The observation angle increments between measurements were adjusted so that more detail was obtained near specular. The highest observation angle resolution was achieved for the Emcore TJPV cell as it was a highly specular reflector while the lowest observation angle increment was achieved for the aluminum which was less specular.

#### 4.2.2 Developing comprehensive look-up tables from measured material sBRDFs

Initially, the measured material sBRDFs needed to be completed for all  $\theta_o$ . The smallest observation angle increment was used with the Emcore TJPV cell, where  $\Delta\theta_o = 0.05^\circ$ . A linear interpolation of all measured sBRDFs was performed with the same increment in order to maintain this fidelity. The interpolation was conducted for all wavelengths and  $\theta_i$  contained in the nine measured sBRDFs.

Next, the sBRDFs were converted from being a function of  $\theta_o$  to  $\theta_{os}$  using Equation 4.2, where  $\Delta\phi = 180^\circ$ . These were set to zero outside of the measured ranges, from  $\theta_{os} = -90^\circ$  to  $90^\circ$ . This range was chosen since the three materials did not exhibit measurable uniform-diffuse components. Should the sBRDF of a material with a strong uniform-diffuse component be developed into a comprehensive look-up table, this range must be increased as this type of material could theoretically exhibit reflectance at  $\theta_{os}$  of  $-180^\circ$  when  $\theta_i$  was near  $90^\circ$ . Figure 4.4 shows the measured sBRDF of aluminum for one illumination polar angle and wavelength, along with the linear interpolation, as functions of  $\theta_{os}$ .

The conversion of  $\theta_o$  to  $\theta_{os}$  was performed as  $\theta_{os}$  is a function of  $\theta_i$ , while  $\theta_o$  is independent of  $\theta_i$ . This meant that the converted sBRDFs were a function of  $\theta_i$  for each angle-off-specular and wavelength. The sBRDFs for all  $\theta_i$  could then be determined using a cubic spline fit, a built-in Matlab [50] function, with a range of  $0^\circ$  to  $90^\circ$  and a  $1^\circ$  interval. Figure 4.5 shows the linearly-interpolated sBRDF of aluminum for one angle-off-specular and wavelength, along with the spline fit, as functions of  $\theta_i$ . This spline fit was conducted for all wavelengths and  $\theta_{os}$  contained in the nine linearly-interpolated sBRDFs.

A consequence of the extrapolation achieved by the spline fit was an sBRDF increase below  $10^\circ$  and above  $60^\circ$ . It was shown in Section 2.2 that sBRDF magnitude increases with an increase in  $\theta_i$  leaving the increase below  $10^\circ$  in question as this does not agree with laboratory measurements. Conversely, while an increase is expected above  $60^\circ$ , the rate at which it does so is questionable. A better spline fit, and more confident extrapolated data, could be achieved if sBRDFs were measured for more  $\theta_i$ , particularly above  $60^\circ$ , and

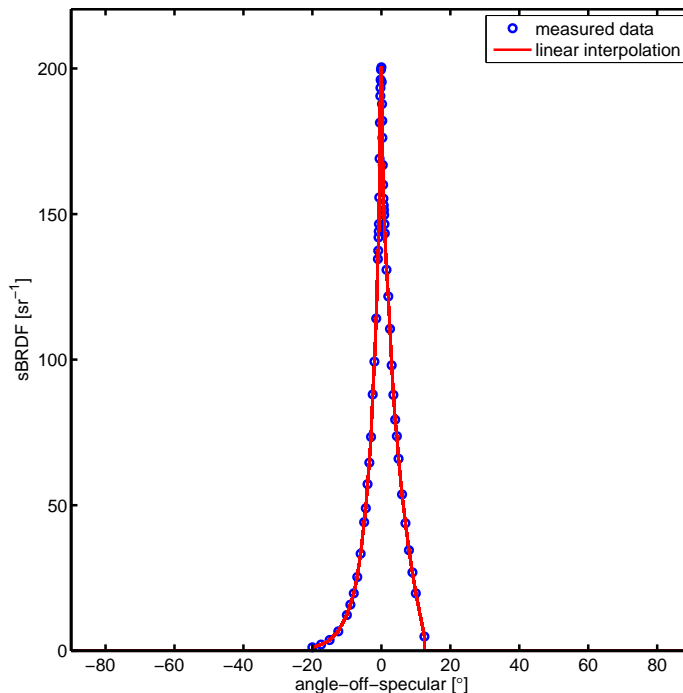


**Figure 4.4:** The measured sBRDF and linear interpolation of 6061-T6 aluminum alloy as a function of angle-off-specular for  $\theta_i = 60^\circ$  and  $\lambda = 950$  nm.

should be considered when developing future material databases. A spline fit using sBRDF measurements from seven  $\theta_i$  values, not shown here, depicted a much greater increase in reflectance above  $60^\circ$  than is shown in Figure 4.5. For the purposes of this research project it was determined that the sBRDFs resulting from splines fit to three  $\theta_i$  values would produce sufficiently accurate results.

When the linearly-interpolated sBRDFs were spline fit to determine their values for all  $\theta_i$ , the  $\Delta\phi$  values for some sBRDFs whose  $\theta_i$  values were smaller than the width of the reflected beam became  $0^\circ$ . As an example, 6061-T6 aluminum alloy exhibited reflectance for  $\theta_{os} = -7^\circ$  in all three measured sBRDFs. The spline fit maintained reflectance for all  $\theta_i$  where  $\theta_{os} = -7^\circ$ . This meant that for this angle-off-specular, when  $\theta_i < 7^\circ$ ,  $\theta_o$  and  $\theta_i$  were on the same side of  $\vec{N}$ , and  $\Delta\phi$  had a value of  $0^\circ$ .

The linear interpolation, conversion of angles, and subsequent spline fit resulted in three look-up tables, one for each material sBRDF. Each was

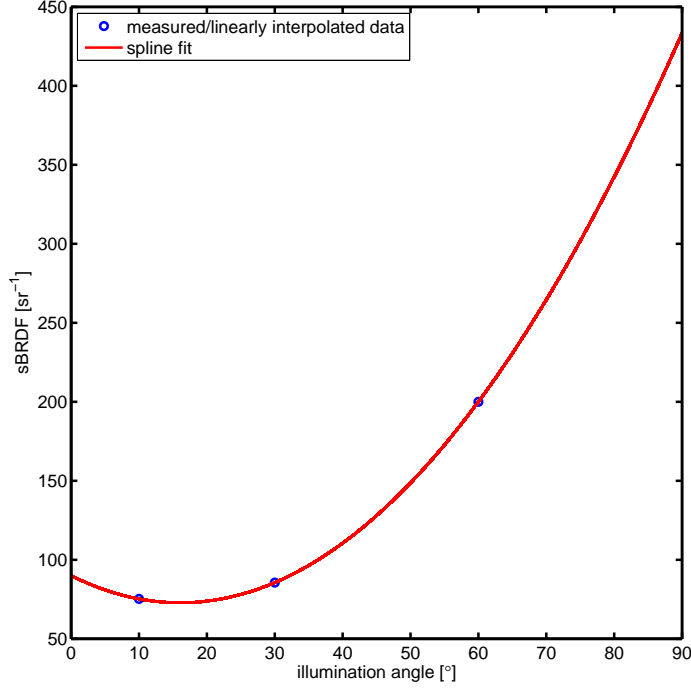


**Figure 4.5:** The linearly-interpolated sBRDF and spline fit of 6061-T6 aluminum alloy as a function of illumination angle for  $\theta_{os} = 0^\circ$  and  $\lambda = 950$  nm.

defined for a  $\theta_i$  range of  $0^\circ$  to  $90^\circ$ , for a  $\theta_{os}$  range of  $-90^\circ$  to  $90^\circ$ , and for  $\Delta\phi = 0^\circ$  and  $180^\circ$ , thereby establishing them as “comprehensive” for the purposes of this research project. The linear interpolation and spline fit preserved the spectral features characteristic of their respective materials as they maintained all measured sBRDFs. These three comprehensive look-up tables are the first entries into a material reflectance database.

Finally, due to the order in which the linear interpolation and spline fit were performed, the following algorithm needed to be followed by the synthetic spacecraft ground truth system to obtain the correct sBRDF from within the structure of the look-up table:

$$\text{material} \rightarrow \theta_{os} \rightarrow \theta_i \rightarrow sBRDF(\lambda)$$

### 4.3 Triangular facets, colour-material definitions, and CAD models

A number of CAD models were created to validate the synthetic spacecraft sBRDF system and subsequent production of BRDFs and colour ratios. Based on the literature review it was decided that these models would be comprised of triangular facets. This section describes the developed mathematical representation of these facets and outlines the colour-material definition system.

#### 4.3.1 Triangular facets

All CAD models used by this system are represented by a collection of triangular facets whose characteristics are defined by matrices. Facet vertices are defined by a  $3 \times 3$  matrix that describes their position in a three-dimensional coordinate system. The facet itself is defined by a  $1 \times 3$  matrix that orders the connection of the vertices and the surface normal vector is defined by a  $1 \times 3$  unit vector. The colour of each facet is defined by a  $1 \times 3$  matrix that provides RGB values. These matrices, along with examples, are provided in Table 4.2. The facet represented by these matrices is shown in Figure 4.6.

Matrix	Name	Description	Example
$V$	Vertices	3D Cartesian coordinates	$\begin{bmatrix} 0 & 0 & 0 \\ 0 & 0.5 & 0.5 \\ 0 & 0.5 & -0.5 \end{bmatrix}$
$F$	Facet	Vertex connection order	$[1 \ 2 \ 3]$
$N$	Surface normal	Unit vector	$[1 \ 0 \ 0]$
$C$	Colour	Facet RGB values	$[1 \ 0 \ 0]$

**Table 4.2: The four matrices of a CAD model facet.**

This format was chosen as most of this data is contained in the STereoLithography (STL) files that are commonly exported by CAD software packages. Matlab can import these files using a simple script and visualize them using its `patch` function. The models used for the research project were initially created using Autodesk's AutoCAD software and exported in American Standard Code for Information Interchange (ASCII) STL format. It should be noted that STL files do not natively incorporate colour and so

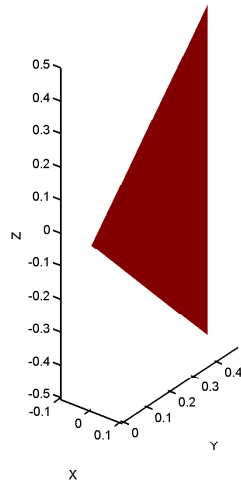


**Figure 4.6:** The facet represented by the matrices in Table 4.2

RGB data had to be manually added to these files after export from the CAD software.

### 4.3.2 Colour-material definition

A facet's material composition is defined by the RGB values contained in its  $C$  matrix. This definition system was chosen as there are millions of possible RGB combinations, making it possible to represent just as many materials, allowing for unrestricted expansion of the comprehensive material reflectance database in the future. The synthetic spacecraft sBRDF system used a facet's colour to determine which material look-up table should be accessed. Table 4.3 shows the colour definitions of the three homogeneous materials used in this research project, which are maintained throughout this thesis.

### 4.3.3 CAD models

Seven CAD models were constructed for this research project, all of which are composed of triangular facets. Six are basic two- and three-dimensional objects, developed to validate the synthetic spacecraft sBRDF system and subsequent production of BRDFs and colour ratios. These are presented in the experiments in Chapter 5. The seventh is a mock-up of the CanX-1 EM spacecraft, presented in Chapter 6, used to reproduce the spacecraft characterization experiment presented in Section 2.1.

Material	RGB Values	Colour
6061-T6 aluminum alloy	[1 0 0]	red
Emcore TJPV cell	[0 0 1]	blue
Lord Aeroglaze 276A reflective white low-outgassing paint	[1 1 1]	white

**Table 4.3: The RGB values and colour definitions of the homogeneous materials.**

## 4.4 System architecture for synthetic spacecraft sBRDF

Synthetic spacecraft sBRDFs were produced within a Matlab-based modular system, currently unnamed. Figure 4.7 provides an overview of the system architecture. Required inputs were a triangular-faceted CAD model, colour-material definitions, scenario parameters, and a database comprised of comprehensive sBRDF look-up tables for each of the model's materials. The products of this system were the sBRDF, BRDF, colour-filtered BRDF, and colour ratios, as they have all demonstrated utility towards the characterization of unresolved spacecraft.

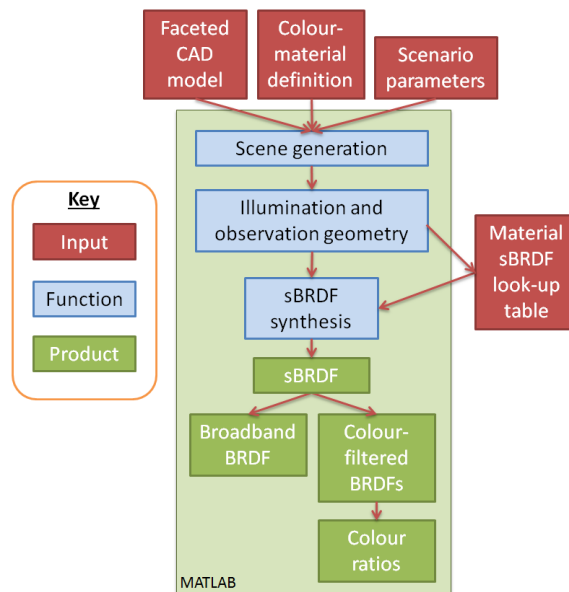


**Figure 4.7: The architecture of the Matlab-based synthetic spacecraft sBRDF system.**

This system was designed so that additional modules could be easily incorporated, thereby increasing its ability to accurately synthesize the ground truth of spacecraft and use it to produce quantities useful for characterization. For example, modules that position and orient the spacecraft in Earth orbit incorporate the Sun's spectrum and solid angle as subtended from the spacecraft, add atmospheric effects, and model detector performance would produce results that simulated those that are collected by ground-based sensors. The



order in which these packages are developed depends on the intended use of the system. The addition of a module to synthesize a spacecraft's polarization of light is currently being considered as this quantity's utility for spacecraft characterization is currently being investigated.

At this point descriptions of the faceted CAD model, colour-material definition, and look-up table have already been provided. The remaining sections in this chapter will outline the Matlab-based mathematical algorithm in Figure 4.7 that has not yet been derived.

## 4.5 Scene generation

In the world of computer-graphics rendering, a *scene* is any collection of objects, light sources, and viewing perspective [35]. A scene including a CAD model and illumination and observation position was required for a spacecraft sBRDF to be synthesized. Scenes were generated by initially placing and orienting a CAD model and the illumination and observation positions into a Cartesian coordinate system. This section describes how the CAD models were placed and oriented, and the definition of the illumination and observation positions.

### 4.5.1 Placement and orientation of CAD models

CAD models were placed in the scene with their centroid at the origin of a Cartesian coordinate system. This was achieved by subtracting the centroid's coordinates from all vertex coordinates. The centroid was determined using Equation 4.3.

$$C = \begin{bmatrix} X \\ Y \\ Z \end{bmatrix} = \begin{bmatrix} \frac{MAX(x)+MIN(x)}{2} \\ \frac{MAX(y)+MIN(y)}{2} \\ \frac{MAX(z)+MIN(z)}{2} \end{bmatrix} \quad (4.3)$$

The assumption made for this research project was that a spacecraft would be rotated about its centroid during a characterization experiment. To mimic this a CAD model would be rotated about its centroid during simulations. This assumption will have to be revisited when producing synthetic sBRDFs for a spacecraft in Earth orbit as it will rotate about its centre of mass which will not necessarily be co-located with its centroid.

Rotation of the facets'  $V$  and  $N$  matrices result in a rotation of the entire model. This was achieved using Equation 4.4, known as Rodrigues' rotation formula [51]:

$$\vec{v}_{rot} = \vec{v} \cdot \cos \theta_{rot} + (\hat{k} \times \vec{v}) \cdot \sin \theta_{rot} + \hat{k} \cdot (\hat{k} \cdot \vec{v}) \cdot (1 - \cos \theta_{rot}) \quad (4.4)$$

where  $\theta_{rot}$  is the rotation angle, by Right-Hand-Rule, and  $\hat{k}$  is the rotation axis unit vector. This equation was chosen as most simulations performed for this research project only required a model rotation about the  $z$ -axis, to reproduce the rotation of the CanX-1 EM during its characterization. Figure 4.8 provides a visualization of the rotation of a CAD model where  $\theta_{rot} = -25^\circ$  and  $\hat{k} = [0 \ 0 \ 1]$ .

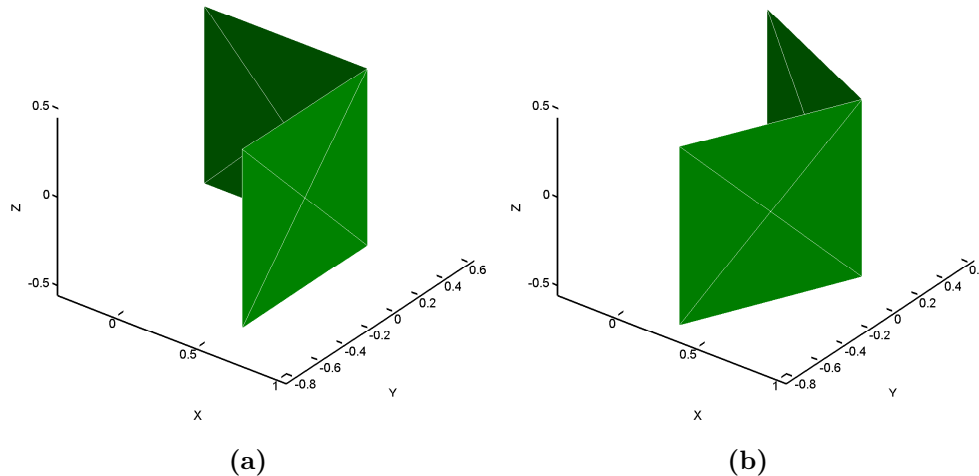


**Figure 4.8:** A CAD model (a) before, and (b) after a  $-25^\circ$  rotation about the  $z$ -axis.

#### 4.5.2 Illumination and observation positions

The illumination and observation positions were provided in spherical coordinates. This format was chosen as it mimicked the apparatus of both characterization experiments in Chapter 2, where the radial distance was uniform and the illumination source and detector were positioned at defined angles. They had to be converted into Cartesian coordinates using Equation 4.5 in order to be incorporated into the scene [50]:

$$P = \begin{bmatrix} x \\ y \\ z \end{bmatrix} = \begin{bmatrix} r \cdot \cos(\theta) \cos(\phi) \\ r \cdot \sin(\theta) \cos(\phi) \\ r \cdot \sin(\phi) \end{bmatrix} \quad (4.5)$$

where  $r$  is the distance from the origin,  $\theta$  is the azimuth angle measured from the positive  $x$ -axis in the  $xy$ -plane, and  $\phi$  is the elevation angle measured from the  $xy$ -plane as shown in Figure 4.9.

Note that the simulations performed during this research project kept the illumination and observation positions within the  $xy$ -plane. Figure 4.10 provides an example of illumination and observation position. Both are located in the  $xy$ -plane and at a radial distance of 5 units from the model centroid. The illumination position (blue) is located at an azimuth of  $45^\circ$ , while the observation position (red) is located on the  $+x$ -axis.

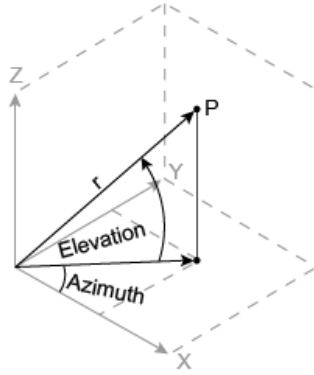


Figure 4.9: The spherical coordinate system. (Source: Matlab, 2015)[50]

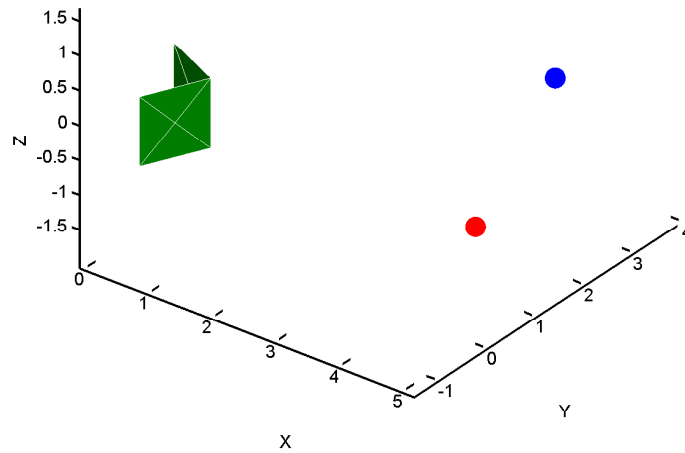


Figure 4.10: Illumination (blue) and observation (red) positions with a radial distance of 5 units, where the illumination azimuth is  $45^\circ$ , and the observation azimuth is  $0^\circ$ . The elevations of both positions are  $0^\circ$  as they are located in the  $xy$ -plane.

## 4.6 Mathematical algorithm for spacecraft sBRDF synthesis

The synthesis of overall spacecraft sBRDF, the quantity chosen to represent its ground truth, was accomplished using a geometric approach. First, the illumination and observation geometry of each facet was determined. All facets that were not both illuminated and observable were then eliminated. The sBRDFs of the remaining facets were obtained from the comprehensive material reflectance database using their respective  $\theta_i$ ,  $\theta_{os}$ ,  $\Delta\phi$ , and  $C$ . Next, each facet's contribution to the overall sBRDF was calculated using the area of its orthogonal projection to the observation position. Finally, all facet contributions were integrated and divided by the total area of their orthogonal projections to produce the overall sBRDF of the spacecraft.

### 4.6.1 Facet illumination and observation geometry

A facet's illumination and observation geometry was determined through a series of steps. First, the facet centroid was required as it was decided that this was the position at which  $\vec{N}$  would be located. The centroid of the facet,  $c$ , was calculated using Equation 4.6:

$$c = \begin{bmatrix} x \\ y \\ z \end{bmatrix} = \begin{bmatrix} \frac{x_1+x_2+x_3}{3} \\ \frac{y_1+y_2+y_3}{3} \\ \frac{z_1+z_2+z_3}{3} \end{bmatrix} \quad (4.6)$$

where  $(x_1, y_1, z_1)$ ,  $(x_2, y_2, z_2)$ , and  $(x_3, y_3, z_3)$  are the Cartesian coordinates of the facet's vertices. Next, the facet's illumination and observation vectors,  $\vec{v}_i$  and  $\vec{v}_o$ , were found by subtracting its centroid from the illumination and observation positions,  $P_i$  and  $P_o$ , as shown in Equation 4.7.

$$\begin{aligned} \vec{v}_i &= P_i - c \\ \vec{v}_o &= P_o - c \end{aligned} \quad (4.7)$$

The facet's illumination and observation polar angles,  $\theta_i$  and  $\theta_o$ , were determined using Equation 4.8. These are located between the facet's  $\vec{N}$ , and  $\vec{v}_i$  and  $\vec{v}_o$ , respectively. All facets with  $\theta_i > 90^\circ$  or  $\theta_o > 90^\circ$  were eliminated as they were not illuminated and observable.

$$\cos \theta = \frac{\vec{v}_1 \cdot \vec{v}_2}{|\vec{v}_1| \cdot |\vec{v}_2|} \quad (4.8)$$

The difference-in-azimuth angle,  $\Delta\phi$ , was also found for each facet using Equation 4.8. This angle is located between the orthogonal projections of  $\vec{v}_i$  and  $\vec{v}_o$ , as seen from the direction of  $\vec{N}$ . An orthographic transformation is required to determine this projection. Equation 4.9 shows how a two-dimensional orthogonal projection matrix,  $M_{2D}$ , is calculated [50]:

$$M_{2D} = T(\theta, \phi) \cdot M_{4D} \quad (4.9)$$

where  $M_{4D}$  is a matrix in homogeneous coordinates and  $T$  is the orthographic transformation matrix. This transformation matrix is a function of  $\theta$  and  $\phi$ , the azimuth and elevation of the viewing direction, and is shown in Equation 4.10.

$$T = \begin{bmatrix} \cos(\theta) & \sin(\theta) & 0 & 0 \\ -\sin(\phi) \cdot \sin(\theta) & \sin(\phi) \cdot \cos(\theta) & \cos(\phi) & 0 \\ \cos(\phi) \cdot \sin(\theta) & -\cos(\phi) \cdot \cos(\theta) & \sin(\phi) & 0 \\ 0 & 0 & 0 & 1 \end{bmatrix} \quad (4.10)$$

In order to calculate a facet's difference-in-azimuth angle, the  $\theta$  and  $\phi$  of each facet's transformation vector was the azimuth and elevation of its surface normal vector from the  $-y$ -axis and  $xy$ -plane, respectively, as this was required by Matlab's `viewmtx` function.

#### 4.6.2 sBRDF acquisition from material reflectance look-up tables

The material reflectance look-up tables were organized as a function of  $\theta_i$  and  $\theta_{os}$ . A facet's illumination and observation geometry was calculated as a function of  $\theta_i$  and  $\theta_o$ . Acquisition of a facet's material sBRDF from the look-up table therefore required a conversion of its  $\theta_o$  to  $\theta_{os}$ . A complication arose when this conversion was attempted using Equation 4.2.

The only two  $\Delta\phi$  values contained in the material reflectance database were  $0^\circ$  and  $180^\circ$ . It was quickly realized that a facet's calculated difference-in-azimuth angle,  $\Delta\phi_{calc}$ , would not be equal to either of these values under two circumstances. The first case was for facets whose  $\vec{N}$  was not parallel to the  $xy$ -plane, possessing a  $z$ -component that was not equal to zero. As the ultimate aim of this research project was to synthesize the sBRDF of the CanX-1 EM spacecraft where facets with these orientations would not exist, further consideration for this case was not pursued.

The second case where  $\Delta\phi_{calc}$  would not be equal to either  $0^\circ$  or  $180^\circ$  was for facets whose  $\vec{N}$  was parallel to the  $xy$ -plane, but whose  $\theta_o$  was not in the

same plane as  $\theta_i$ . During this research project this would be true for any facets whose centroids did not lie in the  $xy$ -plane, which contained both the illumination and observation positions. It was therefore necessary to convert these facets'  $\Delta\phi_{calc}$  to a  $\Delta\phi$  value that was contained in the comprehensive material look-up tables, allowing for sBRDF acquisition. The most straightforward way to perform this conversion was to use Equation 4.11.

$$\Delta\phi = \begin{cases} 0^\circ & \text{if } \Delta\phi_{calc} < 90^\circ \\ 180^\circ & \text{if } \Delta\phi_{calc} > 90^\circ \end{cases} \quad (4.11)$$

A visual representation of this conversion is provided in Figure 4.11. Upon review it was deemed reasonable to assume that as long as the facet's  $\theta_o$  was relatively small the material sBRDF would be close to the actual value. For the purposes of this research project it was decided that facet centroids would not lie farther than  $0.1^\circ$  from the  $xy$ -plane as measured from the observation position, roughly equating to a  $\theta_o$  of  $0.1^\circ$ . This would be achieved if the ratio of model-height to radial-distance-of-observation was approximately 1:100. The consequences of this conversion are assessed in one of the experiments to validate the synthetic spacecraft sBRDF system in Chapter 5. The incorporation of more  $\Delta\phi$  values into the look-up tables should be pursued in the future to eliminate the need for this conversion.

Finally, having performed this conversion it was possible to use Equation 4.2 to convert a facet's  $\theta_o$  to  $\theta_{os}$ , which was used in conjunction with its  $\theta_i$  and RGB colour values to obtain the correct sBRDF from the material reflectance database.

### 4.6.3 Synthesis of overall spacecraft sBRDF

The contribution of each facet to a spacecraft's overall sBRDF was determined by the area of its orthographic projection as viewed from the observation position. The facets were transformed into orthographic coordinates using Equation 4.9, where  $\theta$  and  $\phi$  were the azimuth and elevation of each facet's  $\vec{v}_o$  from its  $\vec{N}$ , respectively. Figure 4.12a shows a CAD model viewed from the observation position located on the  $+x$ -axis, while Figure 4.12b depicts the orthogonal projection.

Each facet's material sBRDF was multiplied by its orthographic area,  $a_{M_{2D}}$ , shown in Equation 4.12. This produced the facet's contribution to the overall sBRDF of the spacecraft:

$$f_r(\theta_i; \theta_{os}; \lambda)_{facet} = a_{M_{2D}} \cdot f_r(\theta_i; \theta_{os}; \lambda)_{material} \quad (4.12)$$

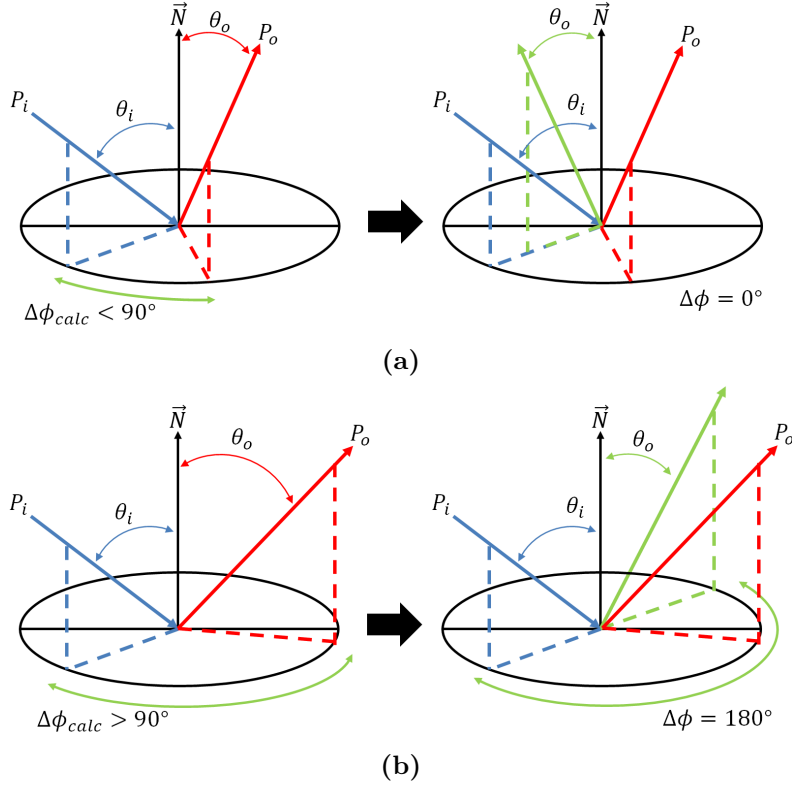


**Figure 4.11:** The conversion of a facet's  $\Delta\phi_{calc}$  to  $\Delta\phi$  for (a)  $\Delta\phi_{calc} < 90^\circ$  and (b)  $\Delta\phi_{calc} > 90^\circ$ .

where the area of a facet,  $a$ , is found using Equation 4.13 and  $A$ ,  $B$ , and  $C$  are the Cartesian coordinates of the facet's vertices.

$$a = \frac{1}{2} \sqrt{|\vec{AB} \times \vec{BC}|} \quad (4.13)$$

Finally, Equation 4.14 describes how the contributed sBRDFs of all facets were integrated and divided by the total orthographic area of the model:

$$f_r(\theta_i; \theta_{os}; \lambda)_{model} = \frac{\sum_{j=1}^n f_r(\theta_i; \theta_{os}; \lambda)_{facet,j}}{\sum_{j=1}^n a_{M_{2D}, facet,j}} \quad (4.14)$$

where  $n$  is the total number of the CAD model's triangular facets that were both illuminated and observable. The sBRDF was divided by the total orthographic area to normalize the result, ensuring that its magnitude was inde-



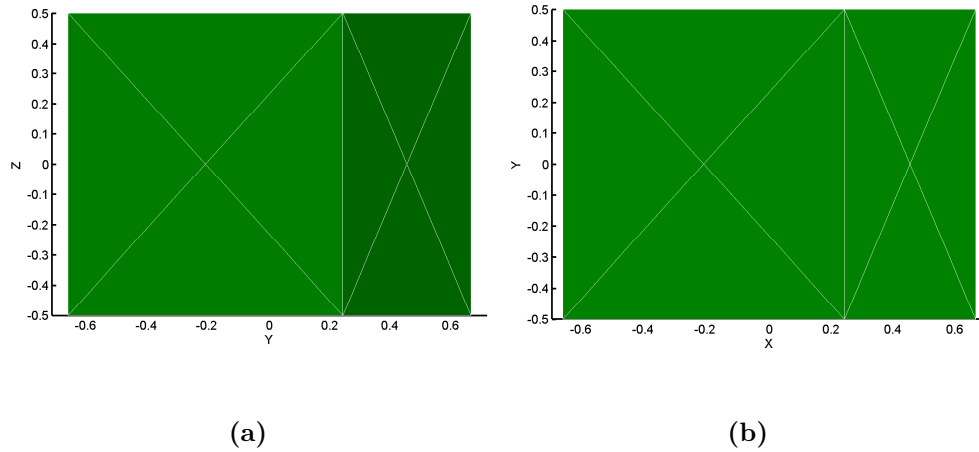


**Figure 4.12:** A CAD model (a) as viewed from the observation position located on the  $+x$ -axis, and (b) its orthogonal projection. The lack of shading in the orthogonal projection is due to its two-dimensional nature. Note the change in axes.

pendant of model size. The final product was the spacecraft's overall sBRDF for one illumination and observation geometry.

## 4.7 Producing BRDFs, colour-filtered BRDFs, and colour ratios

As sBRDFs are the basis for BRDFs, colour-filtered BRDFs, and colour ratios, the synthetic spacecraft sBRDFs could be used to produce these quantities. Each has utility towards characterization of unresolved spacecraft, as shown in Chapter 1. During a simulation, sBRDFs were synthesized for one spacecraft orientation and a range of illumination and observation positions. BRDFs were produced by integrating these sBRDFs over all wavelengths. Colour-filtered BRDFs were produced by first multiplying the sBRDFs by Bessel [13] BVRI colour filters and integrating the products. Finally, colour ratios were calculated by dividing one colour-filtered BRDF by the other. This section describes in detail the production of these quantities.

### 4.7.1 Producing BRDFs

BRDFs were produced by integrating the model's sBRDF over all wavelengths, for each generated sBRDF in a simulation. This relationship is presented in Equation 4.15. During this research project the model rotation was fixed during simulations and changes in orientation were accomplished solely by rotating  $P_i$  and  $P_o$  about the model's centroid in discrete angular steps,  $\Delta\theta$ .

$$f_r(\theta_i; \theta_{os})_{model} = \sum_{P_i, P_{o,1}}^{P_i, P_{o,2}} \sum_{\lambda=350nm}^{1100nm} f_r(\theta_i; \theta_{os}; \lambda)_{model} \cdot \Delta\lambda \cdot \Delta\theta \quad [\text{sr}^{-1}] \quad (4.15)$$

### 4.7.2 Producing colour-filtered BRDFs

Colour-filtered BRDFs were simulated by first multiplying the sBRDF by the four Bessel [13] colour-filters shown in Figure 1.5, resulting in four filtered sBRDFs. The products were then integrated over all wavelengths, similar to the BRDF. The colour-filtered BRDF is presented in Equation 4.16:

$$f_r(\theta_i; \theta_{os})_{model, colour} = \sum_{P_i, P_{o,1}}^{P_i, P_{o,2}} \sum_{\lambda=350nm}^{1100nm} T_{colour}(\lambda) \cdot f_r(\theta_i; \theta_{os}; \lambda)_{model} \quad [\text{sr}^{-1}] \quad (4.16)$$

where  $T_{colour}(\lambda)$  is a Bessel [13] filter.

### 4.7.3 Producing colour ratios

Colour ratios are a quantitative comparison of one colour-filtered light curve to another. Since this comparison is relative, a spacecraft's colour-filtered BRDF can be used instead. Colour ratios were produced by dividing one colour-filtered BRDF by the other, shown in Equation 4.17.

$$\text{Ratio}_{\text{colour}_1/\text{colour}_2} = \frac{f_r(\theta_i; \theta_{os})_{\text{model, colour}_1}}{f_r(\theta_i; \theta_{os})_{\text{model, colour}_2}} \quad (4.17)$$

Six colour ratios were produced for each simulation in this research project, as there were four colour-filters used. These included  $B/V$ ,  $B/R$ ,  $B/I$ ,  $V/R$ ,  $V/I$ , and  $R/I$ .

# 5 Verifying the Synthetic Spacecraft sBRDF System

The synthetic spacecraft sBRDF system must first be verified for ability before it can be used for unresolved spacecraft characterization. This chapter presents a series of simple experiments for the systematic verification of the spacecraft reflectance model. First, a verification that the proper material determination, illumination and observation geometry calculation, and look-up of measured sBRDF data is performed. Included in this verification is the accurate simulation of BRDFs and colour ratios. An analysis of the comprehensive sBRDF data is then conducted, along with BRDFs and colour ratios, to determine whether the material look-up tables modelled expected spectral features. Next, the facet contribution to overall sBRDF is assessed through an analysis of the orthographic area as viewed from the observation position. The effects of the conversion to change a facet's calculated difference-in-azimuth angle to one contained in the look-up tables are then assessed. Finally, simulated BRDFs of three-dimensional models are used to establish the ability of the system to represent more complex shapes. This series of experiments represents a comprehensive verification process by which all spacecraft reflectance modelling systems should be assessed.

## 5.1 Verification of sBRDF look-up and simulation of BRDFs

The most basic function of the spacecraft sBRDF system is to obtain material sBRDF data from a look-up table for a particular illumination and observation geometry. This section outlines an experiment whereby synthetic sBRDFs and the resulting BRDFs and colour ratios are assessed for accuracy.

### 5.1.1 Experiment aim and objectives

The aim of this experiment was to verify that the material sBRDFs, BRDFs, and colour ratios produced by the modelling system were correct. A comparison of synthetic sBRDFs would be made with those presented by Bédard et al. [30] in Section 2.2.4 for similar setup in order to do so. This would indicate that the algorithm was calculating the correct illumination and observation geometry to access the proper sBRDF look-up table, as well as verify that the simulation of BRDFs and colour ratios was accurate.

### 5.1.2 Experiment setup and procedure

The experiment was designed to mimic the homogeneous material characterization setup by Bédard et al. [30] outlined in Section 2.2. Three models were used to represent three material samples. The models were all sheets with a side length of 1 unit, comprised of four triangular facets with surface normal vectors pointed in the  $+x$ -direction. One of the models is shown in Figure 5.1. The materials included Emcore TJPV cell, 6061-T6 aluminum alloy, and Lord Aeroglaze 276A reflective white low-outgassing paint.

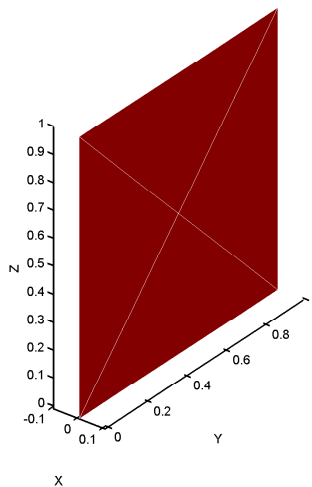


**Figure 5.1: A unit sheet of 6061-T6 aluminum alloy, comprised of four triangular facets.**

The samples were initially rotated to the required illumination angle, after which observations were made for a defined observation angle range. These angles were chosen to mimic the phase angles and reflection angle ranges shown in Figures 2.9b and 2.8. Observations were made in increments of

$\Delta\theta_o = 0.05^\circ$  from a radial distance of 1000 units from the centroid of the models. This distance was chosen as it would reduce error introduced by off-plane facets as suggested in Section 4.6.2. Note that for the purposes of this experiment the orthographic area of the sheet was not used to determine the overall sBRDF, as the calculation of the orthographic area had not yet been verified. Instead the area of the sheet was maintained as 1 unit<sup>2</sup>, ensuring that any observed changes in sBRDF magnitude were a direct result of illumination and observation geometry.

### 5.1.3 Results

The synthetic sBRDFs for all three samples are shown in Figure 5.2. Figure 5.2a contains the spectral features of Emcore TJPV cell, located between 600 nm and 800 nm. The prominent absorption feature characteristic of aluminum [52], located near 800 nm, is present in the synthetic 6061-T6 aluminum alloy sBRDF in Figure 5.2b. Finally, the characteristically uniform reflectance of white paint is shown in Figure 5.2c, the synthetic sBRDF of Lord Aeroglaze 276A reflective white low-outgassing paint. Reflectance was also shown to increase with an increase in  $\theta_i$  in Figures 5.2b and 5.2c.

The synthetic sBRDFs of the Emcore TJPV cell in Figure 5.2a, the 6061-T6 aluminum alloy in Figure 5.2b, and the Lord Aeroglaze 276A reflective white low-outgassing paint depict the same reflectance as the measured sBRDFs presented in Figures 2.9b, 2.8a, and 2.8b, respectively. These results show that the synthetic sBRDF system is able to identify a CAD model's component materials as well as calculate the correct illumination and observation geometries of its individual facets, which it uses to obtain the correct sBRDF from the comprehensive look-up tables.

The normalized BRDFs and associated colour ratios are provided in Figure 5.3. Note that the simulated colour ratios have been calculated where normalized BRDF values are less than 0.2, which was not performed by Bédard et al. [30] due to an unreliable light source. These are presented here to evaluate their behaviour and to provide a broader reference to evaluate simulated colour ratios.

The normalized BRDF of Emcore TJPV cell for all three  $\theta_i$  is approximately  $1^\circ$  wide indicating that the material is highly specular. Also, the colour ratios show that more light is reflected in the B-band than in the V or R. Both the width of the BRDF and the trend in the colour ratios are characteristic of Emcore TJPV cell. The normalized BRDF and associated colour ratios of 6061-T6 aluminum alloy, for  $\theta_i = 60^\circ$ , are presented in Figure 5.3b. The width of the BRDF indicates that the material is less specular. All three

5.1. Verification of sBRDF look-up and simulation of BRDFs

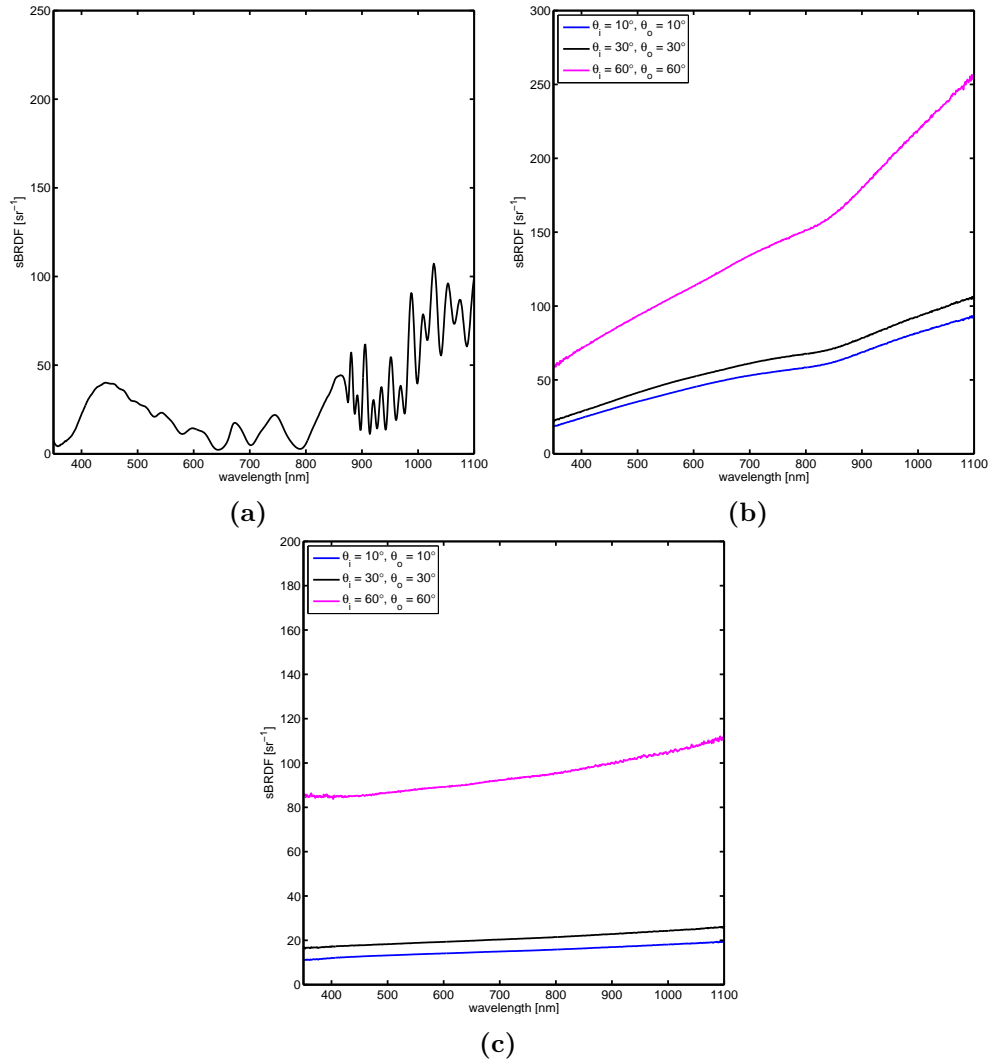


Figure 5.2: The synthetic sBRDF of a 1 unit<sup>2</sup> sheet of (a) Emcore TJPV cell for  $\theta_i = \theta_o = 30^\circ$ , and (b) 6061-T6 aluminum alloy, and (c) Lord Aeroglaze 276A reflective white low-outgassing paint for three illumination and observation geometries using measured sBRDF data.

colour ratios are relatively uniform across the BRDF, except where it is below 0.2. Both of these features are characteristic of aluminum. Finally, the normalized BRDF and associated colour ratios of Lord Aeroglaze 276A reflective white low-outgassing paint, for  $\theta_i = 60^\circ$ , are presented in Figure 5.3c. The simulated BRDF is less specular than the solar cell and more specular than the aluminum, which was expected. Also expected was the uniformity of the colour ratios across the BRDF.

The simulated BRDFs and associated colour ratios possess the same characteristics as the measured ones in Section 2.2.4 when the normalized BRDF is above 0.2, confirming their correct calculation. The colour ratios for BRDFs below this cutoff value appeared continuous and representative of their respective materials in all samples but one. The 6061-T6 aluminum alloy sample for  $\theta_i = 60^\circ$  exhibited unexpected phenomena for  $\theta_{os} > 12^\circ$ , shown in Figure 5.3b. Upon inspection of the measured data, it was discovered that the sBRDF contained negative values for these angles. As this is a physical impossibility the data was inaccurate. It was determined that this would contribute to uncertainty in the developed comprehensive material reflectance look-up table for 6061-T6 aluminum alloy in this  $\theta_{os}$  range. Peculiar phenomena are expected to appear in simulated BRDFs of CAD models containing aluminum facets for similar angles-off-specular as a result. The sBRDF of aluminum for  $\theta_i = 60^\circ$  could not be remeasured for this research project, though this should be performed in the future.

#### 5.1.4 Conclusion

This experiment has proven that the synthetic sBRDF system correctly identifies a CAD model's materials, accurately calculates the illumination and observation geometry of samples, and obtains the proper data from the comprehensive look-up table. The measured sBRDF of 6061-T6 aluminum alloy for  $\theta_i = 60^\circ$  and  $\theta_o > 72^\circ$  contained inaccurate data, and simulations with aluminum under similar angle-off-specular conditions will contain inaccurate phenomena.



5.1. Verification of sBRDF look-up and simulation of BRDFs

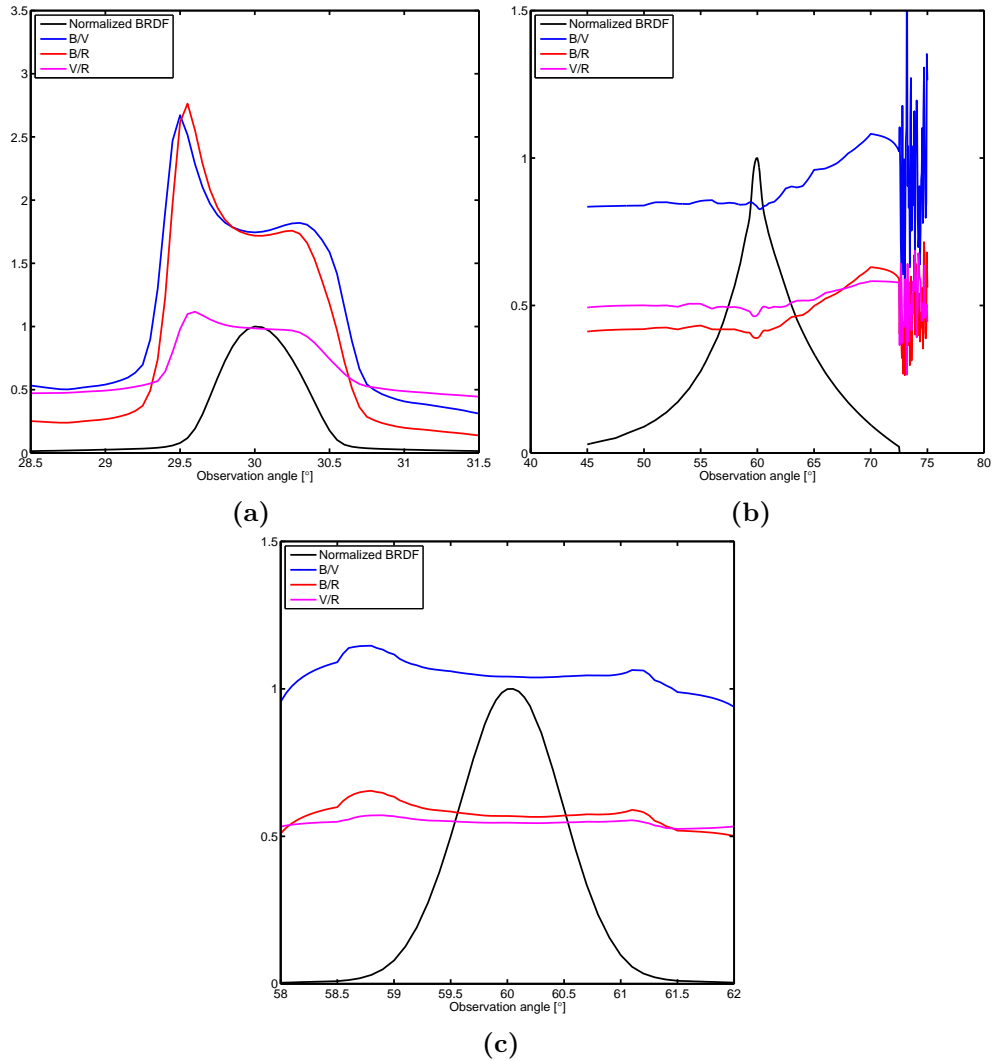


Figure 5.3: The normalized simulated BRDF and colour ratios of a 1 unit<sup>2</sup> sheet of (a) Emcore TJPV cell for  $\theta_i = 30^\circ$ , (b) 6061-T6 aluminum alloy for  $\theta_i = 60^\circ$ , and (c) Lord Aeroglaze 276A reflective white low-outgassing paint for  $\theta_i = 60^\circ$  using measured material sBRDF data.

## 5.2 Verification of sBRDF look-up tables developed using a cubic spline fit

The synthetic sBRDF system relies on comprehensive sBRDF look-up tables, developed using a cubic spline fit, to include all expected ranges of illumination and observation angles. This section outlines an experiment to verify that the synthetic sBRDFs and the resulting BRDFs and colour ratios exhibit phenomena that were observed in the original measured data.

### 5.2.1 Experiment aim and objectives

The aim of this experiment was to verify that the developed sBRDF look-up tables accurately modelled the reflection characteristics of their respective materials. A comparison of synthetic sBRDFs would be made with those presented in Section 5.1 for a number of phase angles to do so. This would indicate that the sBRDFs produced by the spline fit could be used with confidence to model material reflectance at illumination and observation geometries not characterized in the laboratory.

### 5.2.2 Experiment setup and procedure

The experiment was again designed to mimic the homogeneous material characterization setup by Bédard et al. [30] using the same three material unit sheet samples as in Section 5.1. Accordingly, the samples were initially rotated to the required illumination angle after which observations were made for a defined observation angle range. The simulation illumination angles were chosen to frame the illumination angles used to obtain the measured sBRDFs, ensuring that the sBRDF data accessed in the look-up tables was produced using the spline fit. The illumination angles were  $\theta_i = 5^\circ, 20^\circ, 45^\circ,$  and  $70^\circ$ . The observation angle ranges were chosen to show the entire simulated BRDF. As before, observations were made from a radial distance of 1000 units from the centroid of the models in increments of  $\Delta\theta_o = 0.05^\circ$ . Similar to the previous experiment the orthographic area of the unit sheet was not used to calculate the overall sBRDF to ensure that any observed changes in sBRDF magnitude were a direct result of illumination and observation geometry and not model orientation.

### 5.2.3 Results

The synthetic sBRDFs of all three samples are presented in Figure 5.4. In all three cases the characteristic spectral features of the materials are present. Those of Emcore TJPV cell shift towards shorter wavelengths with increasing illumination angle. There is also an increase in the intensity of sBRDF coinciding with an increase of illumination angle, starting at  $\theta_i = 30^\circ$ . There appears to be a decrease in sBRDF as illumination angle increases from  $\theta_i = 5^\circ$  to  $20^\circ$ .

The sBRDFs of all three materials synthesized using data produced by a spline fit exhibit characteristic spectral features which behave as expected with a change in illumination angle. The spectral features of solar cell shift while the aluminum feature remains in place. An increase in sBRDF magnitude, while also expected with an increase in illumination angle, is only observed for  $\theta_i > 30^\circ$ . Instead, the sBRDF intensity decreases as illumination angle increases from  $\theta_i = 5^\circ$  to  $20^\circ$ . This is due to the extrapolation by the spline fit used to develop the comprehensive sBRDF look-up tables. This consequence was suggested in Section 4.2.2 as the cubic spline only had three  $\theta_i$  values to be fit to. The sBRDF is expected to increase with an increase in illumination angle, contributing to the uncertainty of the magnitude of comprehensive sBRDFs below  $\theta_i = 30^\circ$ . Similarly, the rate of increase in sBRDF above  $\theta_i = 60^\circ$  is uncertain, though an increase is expected based on the empirical sBRDFs. Obtaining measured sBRDFs for more  $\theta_i$  values in the future will reduce this uncertainty.

The simulated BRDFs and colour ratios of solar cell and white paint, for  $\theta_i = 45^\circ$ , are shown in Figure 5.5. The solar cell BRDF exhibits high specularity while the white paint is less so.

The simulated BRDFs and colour ratios of aluminum, for  $\theta_i = 5^\circ, 20^\circ, 45^\circ$ , and  $70^\circ$ , are shown in Figure 5.6. The width of the BRDFs indicate that the material is a less specular reflector and the colour ratios are uniform across the BRDF. Both of these phenomena are characteristic of aluminum. In all of the simulations the BRDF curve does not appear smooth and exhibits rapid change or discontinuity, as in Figure 5.6d. Accordingly, the colour ratios depict rapid changes coinciding with the BRDF, including the same discontinuity. Note that these colour ratio anomalies have presented themselves due to the extension of the colour ratios beyond the BRDF cutoff value of 0.2.

The width of the BRDFs and the trends in colour ratios possess similar characteristics as those observed in the measured data. Only in the case of aluminum does the data produced by the cubic spline fit exhibit anomalies such as sudden changes in magnitude and discontinuities. These occur in the

## 5.2. Verification of sBRDF look-up tables developed using a cubic spline fit

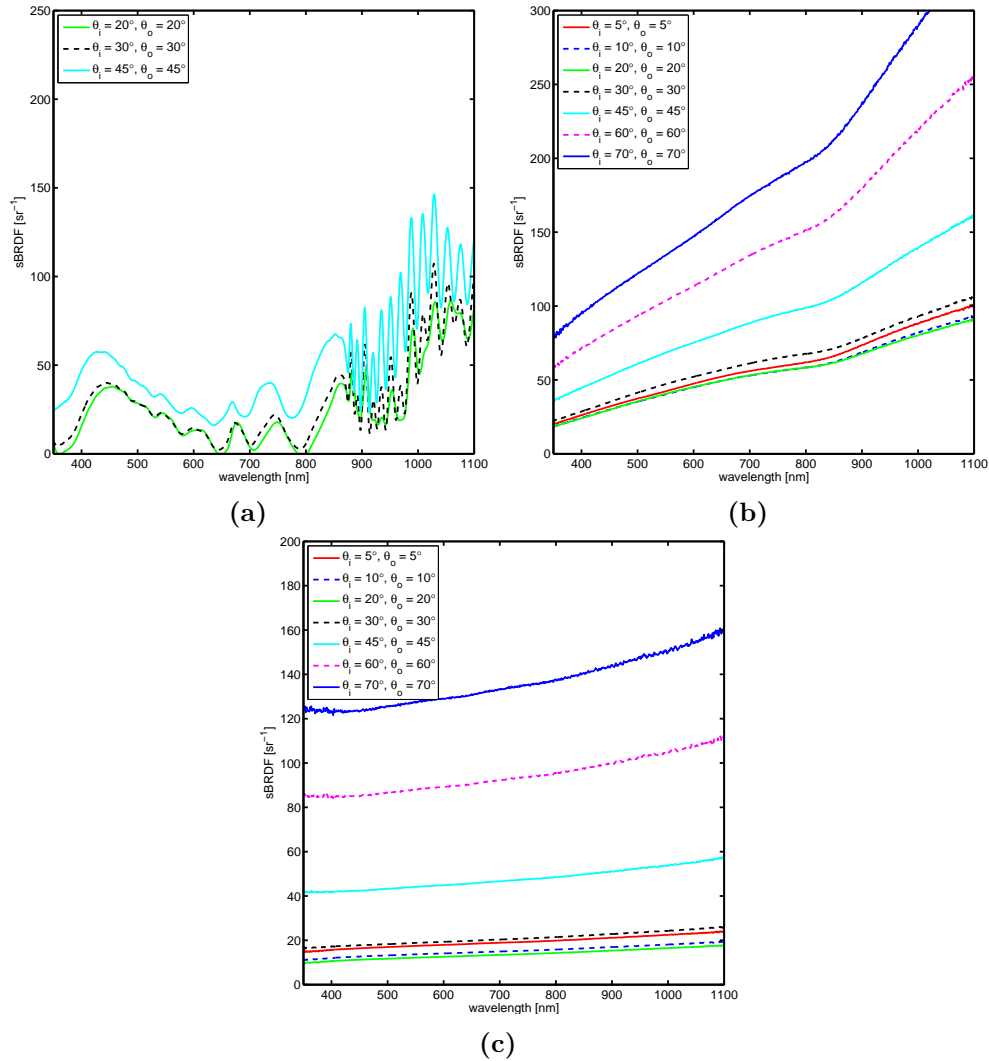


**Figure 5.4:** A comparison of the synthetic sBRDFs for phase angles using measured sBRDF data and phase angles using sBRDF data produced using a spline fit, for a 1 unit<sup>2</sup> sheet of (a) Emcore TJPV cell, (b) 6061-T6 aluminum alloy, and (c) Lord Aeroglaze 276A reflective white low-outgassing paint.

## 5.2. Verification of sBRDF look-up tables developed using a cubic spline fit

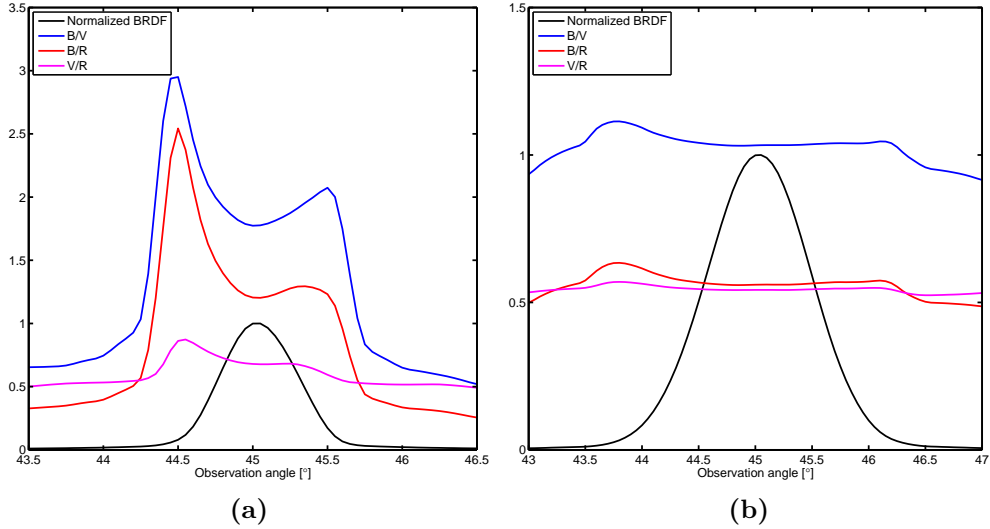


**Figure 5.5:** The simulated BRDF and colour ratios for a 1 unit<sup>2</sup> sheet of (a) Emcore TJPV cell, and (b) Lord Aeroglaze 276A reflective white low-outgassing paint for  $\theta_i = 45^\circ$ .

$\theta_{os}$  range where inaccurate data was present in the measured sBRDF, shown in Figure 5.3b. These anomalies are expected to present themselves in simulations where CAD models contain aluminum facets that are observed in this angle-off-specular range. Future work to acquire more accurate aluminum sBRDFs is encouraged so that these anomalies can be eliminated. Their presence for the remainder of the research project was considered allowable as their source is understood.

### 5.2.4 Conclusion

This experiment has established that the comprehensive sBRDF look-up tables developed using a cubic spline fit empirically model their respective material's reflection characteristics for all illumination and observation angles. They have maintained the spectral characteristics that were present in the measured material sBRDFs. This is true for Emcore TJPV cell and Lord Aeroglaze 276A reflective white low-outgassing paint, and shown by comparison with the synthetic sBRDFs of Section 5.1. The magnitudes of these sBRDFs below  $\theta_i = 30^\circ$  and above  $\theta_i = 60^\circ$  contain uncertainty due to the limited measured data with which to fit a spline curve. Comprehensive look-up tables developed using inaccurately measured sBRDFs similarly

## 5.2. Verification of sBRDF look-up tables developed using a cubic spline fit

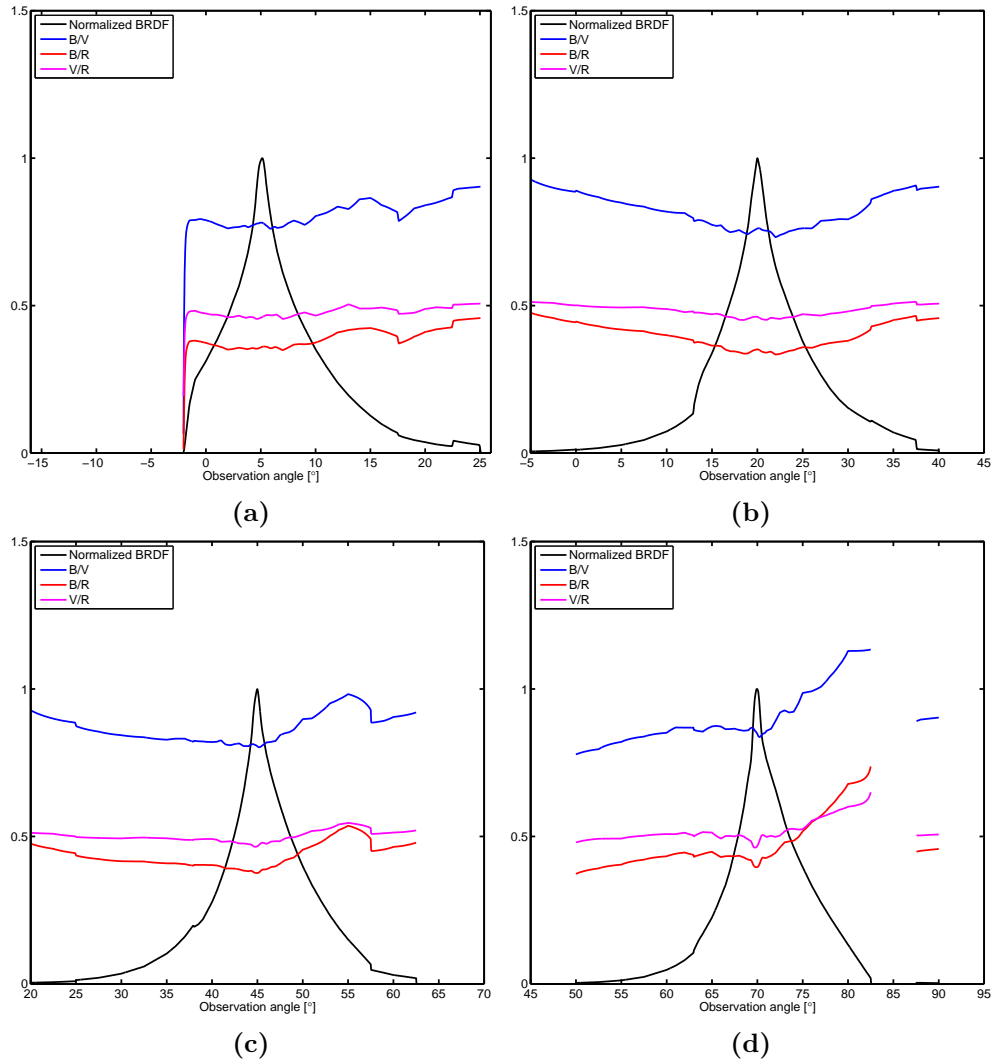


**Figure 5.6:** The simulated BRDF and colour ratios of a 1 unit<sup>2</sup> sheet of 6061-T6 aluminum alloy for (a)  $\theta_i = 5^\circ$ , (b)  $\theta_i = 20^\circ$ , (c)  $\theta_i = 45^\circ$ , and (d)  $\theta_i = 70^\circ$ .

## 5.2. Verification of sBRDF look-up tables developed using a cubic spline fit

maintained material spectral reflectance characteristics, however, these characteristics themselves were inaccurate. Aluminum BRDFs and colour ratios exhibit anomalies at greater angles-off-specular due to the inaccurate nature of the measured sBRDFs and new measurements should be made in the future to eliminate these anomalies.

## 5.3 Verification of facet contribution calculation

The aim of this research project is to synthesize the ground truth of the CanX-1 EM, represented by its overall sBRDF. This model contains multiple materials and their proportionality needs to be considered to model the spacecraft's reflectance. The system must therefore be able to determine the individual contribution of a CAD model's facets to the overall sBRDF, including their orthogonal projection to the observer. This section outlines an experiment to show that a model's individual facets, combined with its orthographic area as viewed from the observation position, was used to synthesize its overall sBRDF.

### 5.3.1 Experiment aim and objectives

The aim of this experiment was to verify that the individual contributions of a CAD model's facets were used in the synthesis of overall sBRDF, and to confirm that the sBRDF was not proportional to the size of the model as it is an infinitesimal quantity. Initially, a direct comparison of synthetic sBRDFs without the orthographic area calculation would be made with those that did to establish that this calculation did not affect spectral reflectance. Next, the synthetic sBRDFs of models of different sizes and compositions were compared for similar illumination and observation geometry to demonstrate that the sBRDF was only affected by model composition.

### 5.3.2 Experiment setup and procedure

Eight simulations were performed for this experiment. In the first two an Emcore TJPV cell unit sheet was used to simulate a BRDF for a phase angle range of  $\beta = 0^\circ$  to  $180^\circ$  from a radial distance of 1000 units from the centroid of the model in increments of  $2^\circ$ . This *all-phase-angle* simulation is depicted in Figure 5.7 where the illumination and observation positions begin co-located on the  $x$ -axis and rotate in opposite directions in the  $xy$ -plane. The first simulation was performed without the orthographic area calculation while the second was performed with this calculation. The sBRDFs and BRDFs from these simulations are expected to be similar as the orthogonal projection of the model does not affect the spectral features or magnitude of the sBRDF.

The next six simulations each used their own model. These included a unit sheet and half-sheet of Emcore TJPV cell, a unit sheet and half-sheet of 6061-T6 aluminum alloy, and a unit sheet and half-sheet combining the two. Figure 5.8 depicts the models that were a combination of both materials. All



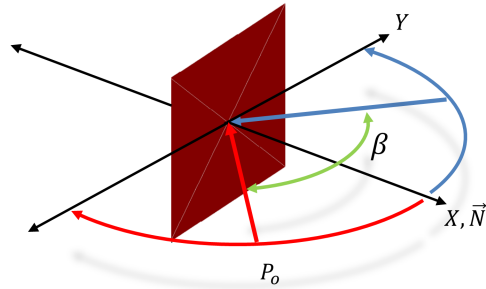


**Figure 5.7:** The all-phase-angle simulation scenario. Note that  $\beta = 2 \cdot \theta_i = 2 \cdot \theta_o$ .

simulation scenarios were for a phase angle of  $120^\circ$  from a radial distance of 1000 units from the centroid of the model. The sBRDFs of models of similar composition were expected to be the same as the size of the model does not affect its sBRDF. Also, the models of mixed composition were expected to present sBRDFs that were a proportional combination of the sBRDFs of their component materials.

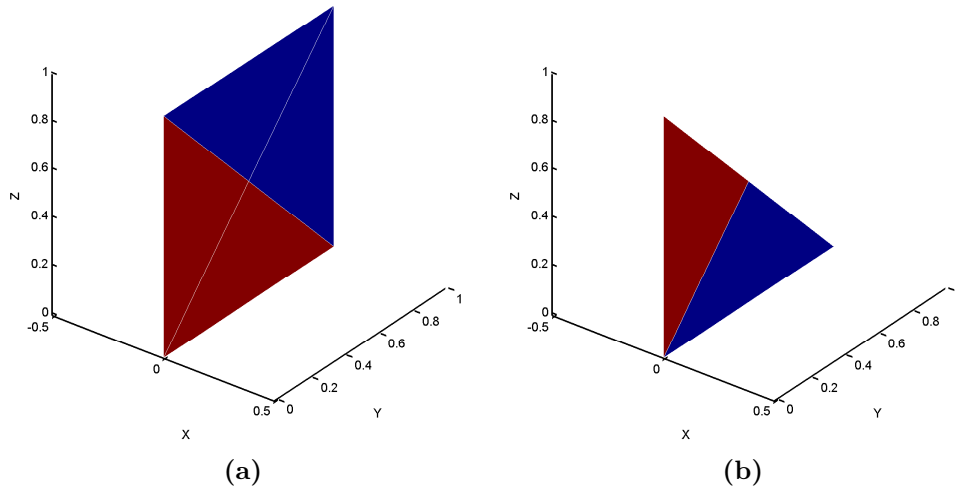


**Figure 5.8:** A (a) unit sheet, and (b) half-sheet composed of equal parts Emcore TJPV cell and 6061-T6 aluminum alloy.

### 5.3.3 Results

The sBRDF for an Emcore TJPV cell unit sheet without orthographic area calculation is shown in Figure 5.9a while the sBRDF of the same model with the calculation is shown in Figure 5.9b. Their similarity was expected as the model projection does not affect the spectral features or magnitude of the sBRDF.

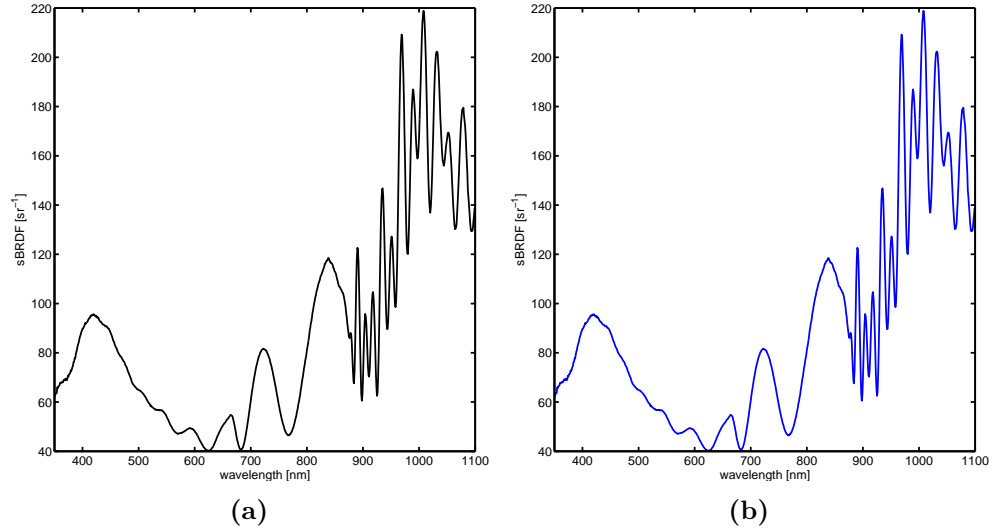


**Figure 5.9: The synthetic sBRDF for a phase angle of  $120^\circ$  of an Emcore TJPV cell unit sheet (a) without orthographic area calculation, and (b) with orthographic area calculation.**

The all-phase-angle simulated BRDFs of the same unit sheet with and without orthographic area calculation are presented in Figure 5.10. Unsurprisingly, as the sBRDFs are unaffected, so to are their subsequent BRDFs. The unchanged colour ratios are further evidence of this.

Finally, the synthetic sBRDFs for the three unit sheet models are shown in Figure 5.11a. The synthetic sBRDFs for the three half-sheet models are shown in Figure 5.11b.

The sBRDFs are the exact same for models of similar composition regardless of size. This was expected as the sBRDF is not a function of model size. The models composed of both materials present an sBRDF that is a proportional combination of the two. In this case, since each material composed half of the model, the overall sBRDF was the result of an even mixture of their respective sBRDFs for this illumination and observation geometry.

### 5.3. Verification of facet contribution calculation

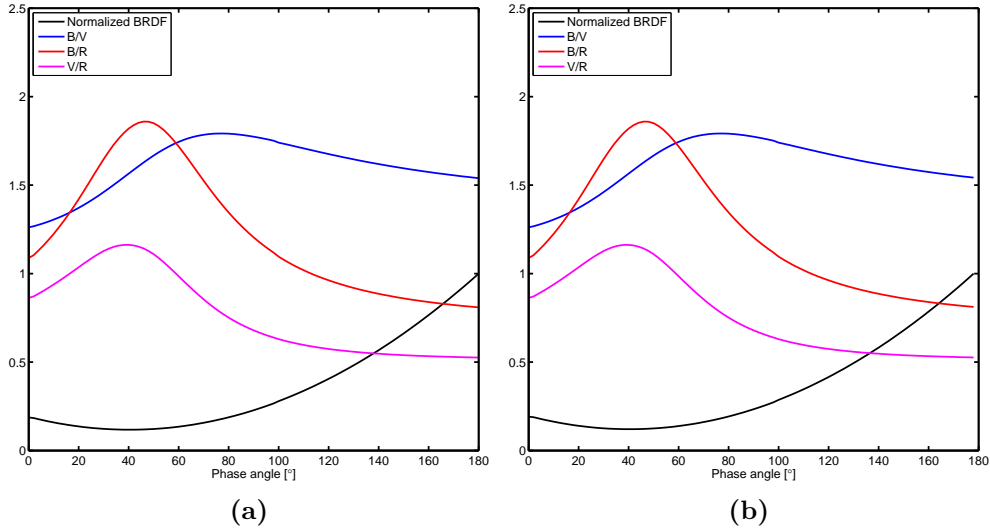


Figure 5.10: The simulated BRDF of an Emcore TJPV cell unit sheet (a) without orthographic area calculation, and (b) with orthographic area calculation for a phase angle range of  $\beta = 0^\circ$  to  $180^\circ$ .

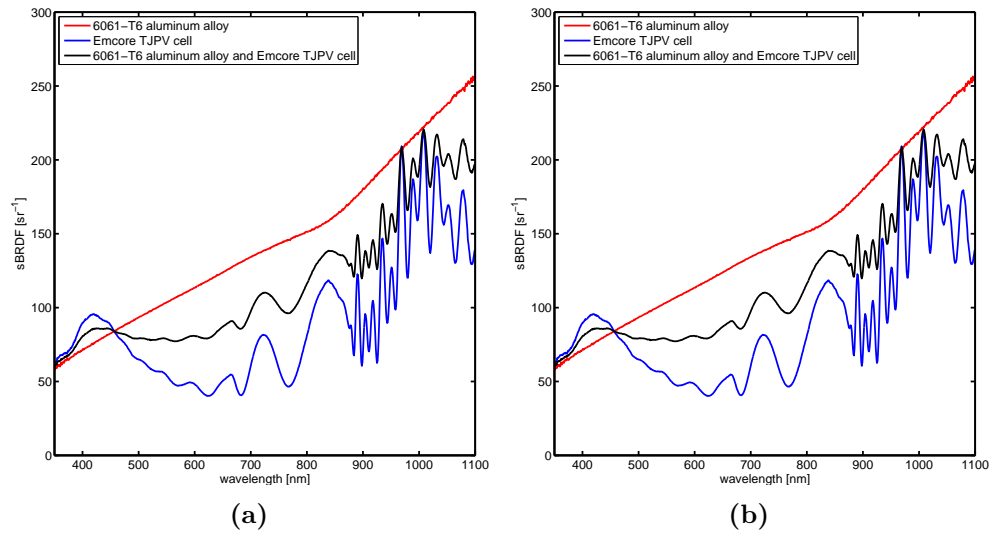


Figure 5.11: The synthetic sBRDFs for a phase angle of  $120^\circ$  of (a) three unit sheet models, and (b) three half-sheet models.

#### **5.3.4 Conclusion**

This experiment has verified that the orthographic area calculation does not affect the spectral features or magnitude of synthetic sBRDFs. It has also demonstrated the system's ability to calculate facet contribution and that overall sBRDF is unaffected by model size.

## 5.4 Assessment of effect of angle conversion for sBRDF look-up

The validity of the synthetic sBRDF system will be established by modelling the reflectance of the CanX-1 EM. Simulations using this spacecraft will contain facets that possess a  $\Delta\phi_{calc}$  value that is not equal those contained by the sBRDF look-up tables,  $0^\circ$  and  $180^\circ$ . These values occur when a facet's surface normal vectors are not parallel to, or its centroids are contained by, the  $xy$ -plane. The conversion described in Section 4.6.2 was implemented in order to use in-plane sBRDF data for these off-plane geometries. This section describes an experiment to assess the overall effect of this conversion during these simulations.

### 5.4.1 Experiment aim and objectives

The aim of this experiment was to assess how the  $\Delta\phi$  conversion required to access the sBRDF look-up table affected synthetic sBRDFs. A comparison of simulated BRDFs and colour ratios would be made, generated using models with facet centroids located either in the  $xy$ -plane or outside of this plane. Two simulation scenarios were defined to produce simulations to achieve this aim.

### 5.4.2 Experiment setup and procedure

This experiment consisted of four simulations conducted solely using a bow-tie CAD model. This model was an arrangement of two triangular facets of Emcore TJPV cell with longest side length of 1 unit. Figure 5.12 depicts this model in both a horizontal and vertical orientation. The synthetic sBRDF system placed a facet's surface normal vector at its centroid. Therefore, the  $\vec{N}$  of the facets of the bow-tie in Figure 5.12a are in the  $xy$ -plane, give them  $\Delta\phi$  values of  $0^\circ$  or  $180^\circ$ . This would allow the system to directly access the sBRDF look-up tables without the  $\Delta\phi$  conversion. Conversely, the  $\vec{N}$  of the facets of a bow-tie in Figure 5.12b are not in the  $xy$ -plane, therefore requiring the angle conversion to utilize the look-up tables. In order to minimize error introduced by the  $\Delta\phi$  angle conversion, the constraint of model-height to radial-distance-of-observation ratio of 1:100 was imposed as suggested in Section 4.6.2. Simulations were conducted with the observation position at a radial distance of 1000 units from the centroid of the model. As the model was located at a sufficient distance from the observation position, the BRDFs

for both orientations were expected to be similar, indicating that the  $\Delta\phi$  conversion was not introducing significant error to the synthetic sBRDF.

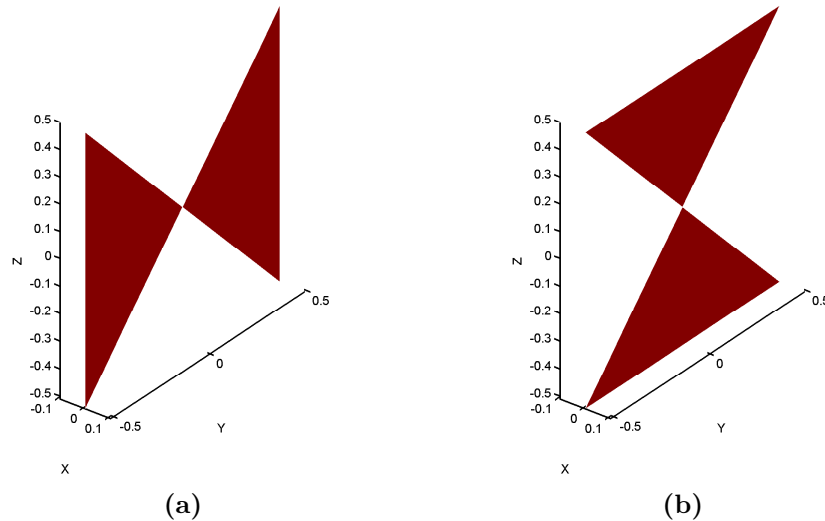


**Figure 5.12:** A bow-tie CAD model comprised of two triangular facets oriented (a) horizontally, and (b) vertically. Note that the facet centroids, the location of the surface normal vectors, are in the  $xy$ -plane for the horizontal model and off-plane for the vertical one.

Two scenarios were used to synthesize sBRDFs for the bow-tie in each orientation, producing a total of four simulations. The first scenario was *fixed-illumination*, where the illumination position was fixed on the  $+x$ -axis. The observation position swept across the axis in the  $xy$ -plane. This scenario is provided in Figure 5.13a. The second scenario was *fixed-observation*, where the observation position was fixed and the illumination position swept across the axis, shown in Figure 5.13b. In both simulations the non-fixed position rotated in increments of  $0.05^\circ$ .

### 5.4.3 Results

The fixed-illumination BRDFs and colour ratios of an Emcore TJPV cell bow-tie for horizontal and vertical orientation are shown in Figure 5.14. The only noticeable difference in BRDF is that the vertical orientation exhibits a plateau in magnitude where the most extreme off-plane facet observations were made, shown in Figure 5.14b. The colour ratios are the same where the normal-

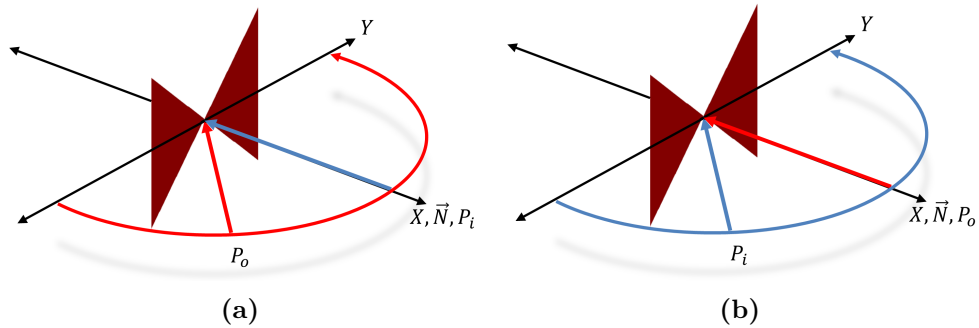


**Figure 5.13:** The (a) fixed-illumination, and (b) fixed-observation simulation scenarios.

ized BRDF is greater than 0.2. Beyond this value the colour ratios possess characteristic differences.

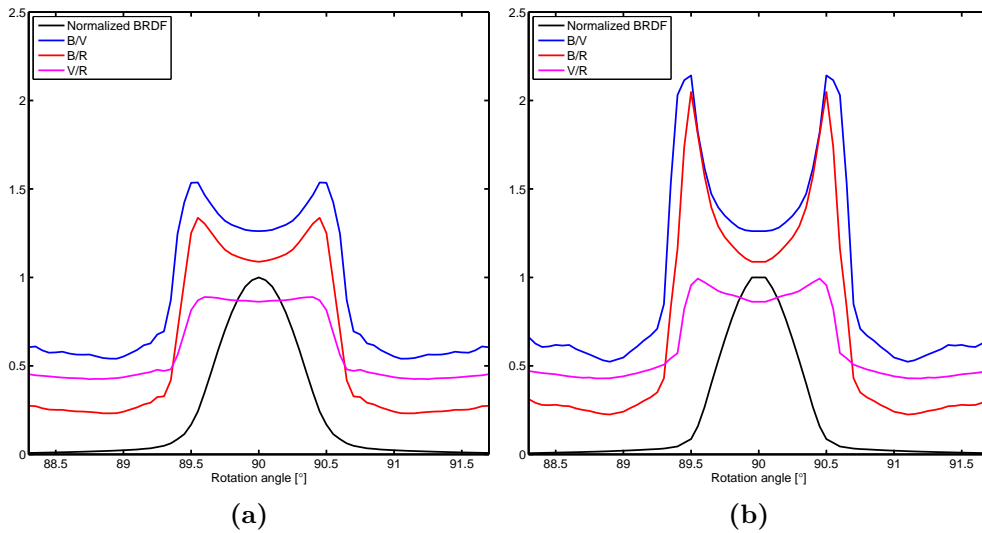


**Figure 5.14:** The normalized BRDFs and associated colour ratios for an Emcore TJPV cell bow-tie simulated with fixed-illumination and oriented (a) horizontally, and (b) vertically. Note that  $\theta_o = 0^\circ$  for a rotation angle of  $90^\circ$ .

The fixed-observation BRDFs and colour ratios of an Emcore TJPV cell bow-tie for horizontal and vertical orientation are shown in Figure 5.15. Again, the only noticeable difference in BRDF is that the vertical orientation exhibits

a plateau in magnitude where the most extreme off-plane facet observations were made, shown in Figure 5.15b. As before the colour ratios are the same where the normalized BRDF is greater than 0.2, however, below this value they exhibit a difference in magnitude.

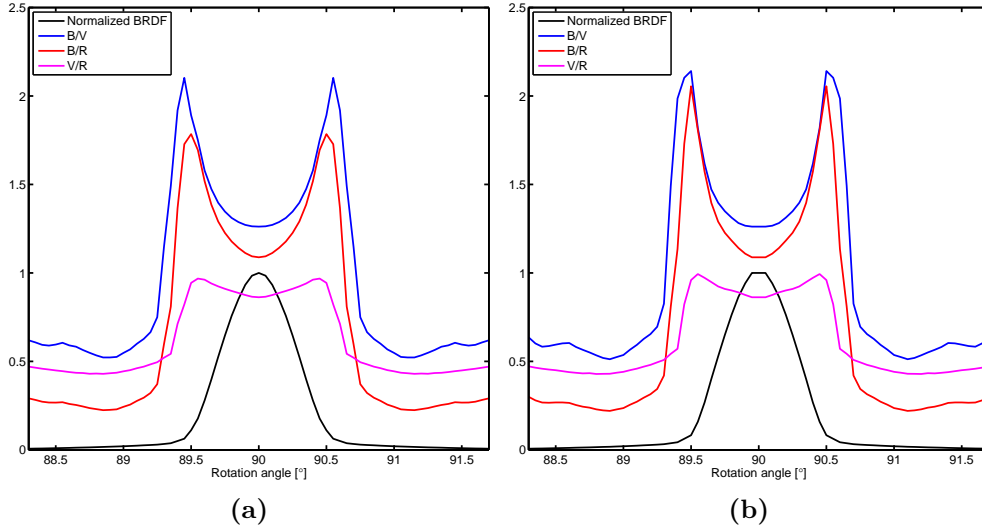


**Figure 5.15:** The normalized BRDFs and associated colour ratios for an Emcore TJPV cell bow-tie simulated with fixed-observation and oriented (a) horizontally, and (b) vertically. Note that  $\theta_i = 0^\circ$  for a rotation angle of  $90^\circ$ .

The BRDF plateaus exhibited in Figures 5.14b and 5.15b are the result of both of the model's facets having the same illumination and observation geometry due to the  $\Delta\phi$  conversion. The plateaus were not observed in Figures 5.14a and 5.15a where each facet had its own unique illumination and observation geometry.

The difference in colour ratios for both simulation types are observed where the normalized BRDF value is below 0.2, a region where they are considered unreliable by Bédard et al. [30] as described in Section 2.2. Above this value, the colour ratios depict the same relative abundances of each passband, indicating that the  $\Delta\phi$  conversion used by the synthetic sBRDF system does not introduce error within the developed scenario constraints.

The fixed-illumination BRDFs and fixed-observation BRDFs may be directly compared where their  $\theta_i$  and  $\theta_o$  are the same. This only occurs at one point in all simulations, when  $\theta_i = \theta_o = 0^\circ$ , where the rotation angle in each scenario is  $90^\circ$ , and the BRDF and colour ratios are indeed similar at this



location. At no other point within the simulation scenarios does  $\theta_i = \theta_o$  so further comparison can not be made.

As all simulations in this experiment were conducted for models whose observed facets possessed surface normal vectors parallel to the  $xy$ -plane the verification only applies to models whose facets are similarly oriented. This was within the scope of the research project as the CanX-1 EM was limited to this orientation during its characterization, outlined in Section 2.1. The future acquisition of off-plane material sBRDF measurements will eliminate the requirement for this  $\Delta\phi$  conversion and the uncertainties that it introduces.

#### 5.4.4 Conclusion

The consequences of the  $\Delta\phi$  conversion required for the synthetic sBRDF system to access the sBRDF look-up tables for off-plane observations have been assessed. The differences in the BRDFs only occur where extreme off-plane observations are made. The colour ratios depict the same relative abundances of each passband where the BRDF is greater than 0.2, within the range of reliability. The angle conversion does not negatively affect the simulation of BRDFs for off-plane facets, for scenarios within the given constraints. Regardless, its requirement should be eliminated in the future by expanding the comprehensive material reflectance database to include off-plane observations.

## 5.5 3D model verification

The accurate representation of three-dimensional models was required for the synthesis of the CanX-1 EM's ground truth. This section presents an experiment to verify the ability of the system to represent these models. This experiment was the final verification required before confidence could be given to synthetic spacecraft ground truths produced by the system developed for this research project.

### 5.5.1 Experiment aim and objectives

The aim of this experiment was to verify the ability of the synthetic sBRDF system to accurately represent three-dimensional objects. This verification would be made by comparing simulated BRDFs with measured ones when possible.

### 5.5.2 Experiment setup and procedure

In this experiment six different models were used including a unit cube of Emcore TJPV cell, a unit cube of 6061-T6 aluminum alloy, a disc of Emcore TJPV cell, a disc of 6061-T6 aluminum alloy, a sphere of Emcore TJPV cell, and a sphere of 6061-T6 aluminum alloy. The unit cube, disc, and sphere models are shown in Figures 5.16a, 5.16b, and 5.16c, respectively. Their facets possess outward-radiating surface normal vectors. The unit cube is comprised of six of unit sheets; the disc has a height of 1 unit and radius of 5 units; and the sphere has a radius of 10 units. In all simulations the illumination and observation positions were radially located 1000 units from the model centroids.

Five simulations were performed using the unit cube. The first two simulations were *fixed-phase*, where the illumination and observation positions were both rotated  $360^\circ$  about the model centroid in the  $xy$ -plane in increments of  $0.1^\circ$  with a constant phase angle between them. This simulation type is shown in Figure 5.17a. The phase angle was maintained at  $10^\circ$  for both simulations.

The cube was oriented with a  $25^\circ$  and  $50^\circ$  rotation about the  $z$ -axis for the first and second simulations, respectively. The location of this rotation angle is provided in Figure 5.18. The BRDFs from these simulations were expected to be similar to the one presented in Figure 2.3, exhibiting four reflectance peaks separated by  $90^\circ$ . The peaks would be shifted  $25^\circ$  when comparing the BRDF from the first simulation with the second due to the greater model rotation of  $25^\circ$ .

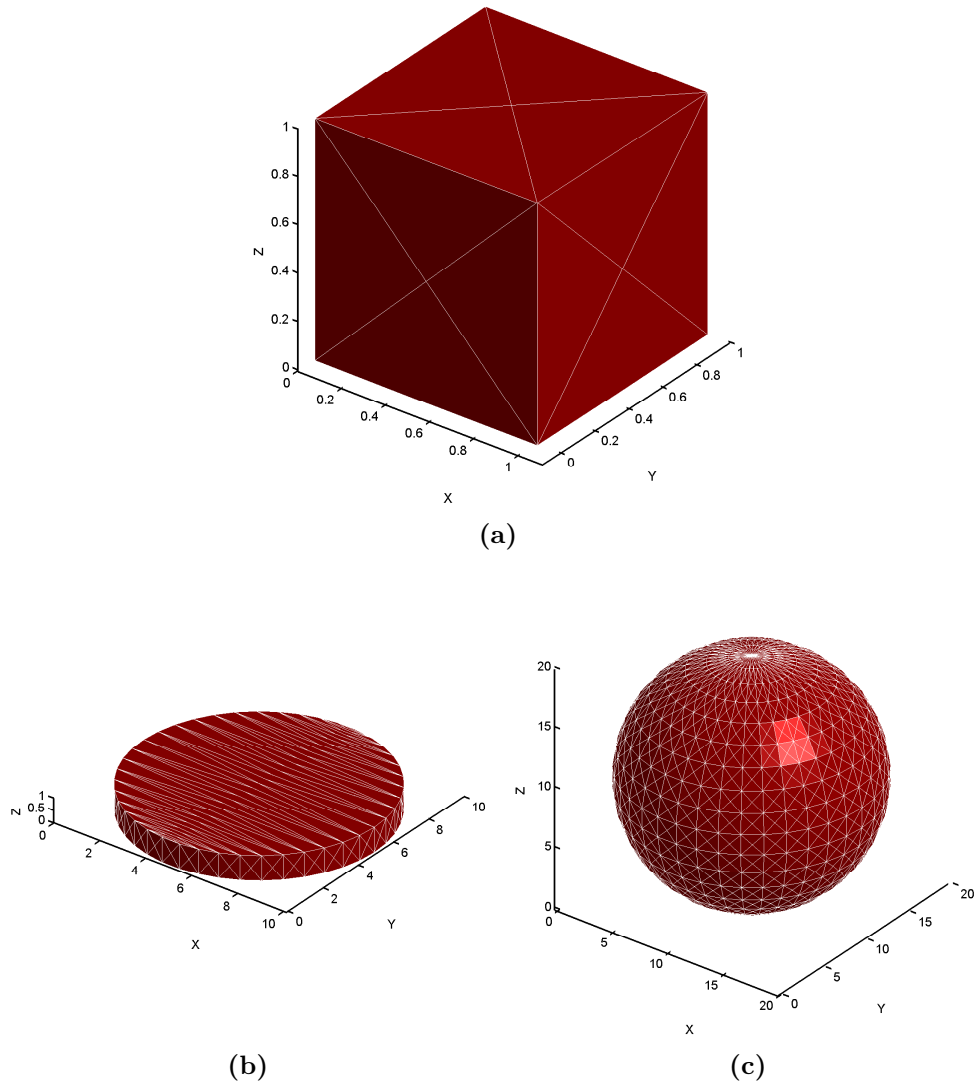
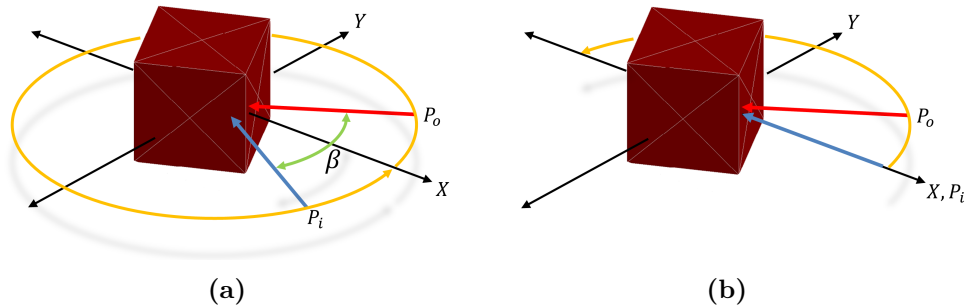
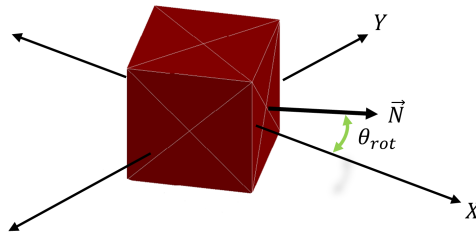


Figure 5.16: A 6061-T6 aluminum alloy (a) unit cube, (b) a disc, and (c) a sphere.



**Figure 5.17:** The (a) fixed-phase, and (b) fixed-illumination simulation scenarios for this experiment.



**Figure 5.18:** Rotation of the unit cube about the  $z$ -axis.

The third simulation was fixed-phase, using a 6061-T6 aluminum alloy unit cube. Again, the model was initially rotated  $25^\circ$ . The illumination and observation positions were both rotated  $360^\circ$  about the model centroid in the  $xy$ -plane in increments of  $0.1^\circ$  with a constant phase angle of  $10^\circ$  between them. The BRDF was expected to be similar to that of the Emcore TJPV cell unit cube produced using the same scenario parameters, however, its peaks would be less specular due to the reflectance nature of the aluminum.

The fourth and fifth simulations were fixed-illumination, where the illumination and observation position began co-located on the  $x$ -axis and the observation position was rotated  $360^\circ$  about the model centroid in the  $xy$ -plane in increments of  $0.1^\circ$ . This simulation type is shown in Figure 5.17b. The models, unit cubes of Emcore TJPV cell and 6061-T6 aluminum alloy, had an initial rotation of  $25^\circ$  about the  $z$ -axis. Both simulations were expected to produce two peaks of different magnitude separated by  $180^\circ$ . The first peak would occur where  $\theta_i$  was less than the second, causing a difference in intensity. The reflectance of the aluminum cube would be less specular than the solar cell cube.

The next two simulations were fixed-phase, utilizing both disc models. The discs were oriented so that they were viewed edge-on, where all facet surface normals were parallel to the  $xy$ -plane. Neither model was initially rotated. The illumination and observation positions were both rotated  $360^\circ$  about the models' centroid in the  $xy$ -plane in increments of  $0.1^\circ$  and the phase angle was maintained at  $10^\circ$ . The simulation of the Emcore TJPV disc was expected to produce a BRDF that exhibited specular peaks of similar magnitude. As the edge of the disc was composed of 42 flat sheets the same number of peaks would present themselves. The 6061-T6 aluminum alloy disc would similarly produce a BRDF with 42 peaks, however, their reflectance would be less specular due to the reflectance of the aluminum.

Two more simulations utilized both discs with no initial rotation. Each model was simulated using a fixed-illumination scenario, where the illumination and observation position began co-located on the  $x$ -axis and the observation position was rotated  $180^\circ$  about the model centroid in the  $xy$ -plane in increments of  $0.1^\circ$ . The BRDF of the solar cell disc was expected to produce specular peaks with changing magnitude similar to the curve shown in Figure 5.10 due to the increasing phase angle associated with each peak. The aluminum disc would exhibit the same overall shape with less specular peaks.

The next two simulations were fixed-phase, utilizing both sphere models. Neither model was initially rotated. The illumination and observation positions were both rotated  $360^\circ$  about the models' centroid in the  $xy$ -plane in increments of  $1^\circ$  and the phase angle was maintained at  $10^\circ$ . The results from these simulations were expected to be unrealistic as the model sphere contains facets whose surface normal vectors are not parallel to the  $xy$ -plane, a condition required to utilize the material look-up tables. The sphere does possess a "belt" of 38 sheets similar to the disc, so features of the BRDFs produced by the fixed-phase disc simulations were expected to appear. A sphere should produce a uniform BRDF for a fixed-phase simulation similar to the disc, however, the model was expected to break down at this point.

The final two simulations utilized both spheres with no initial rotation. Each model was simulated using a fixed-illumination scenario, where the illumination and observation position began co-located on the  $x$ -axis and the observation position was rotated  $180^\circ$  about the model centroid in the  $xy$ -plane in increments of  $1^\circ$ . Again, the model was expected to break down. The BRDFs should have a shape resembling that of the discs of similar composition though this was not expected to appear in the simulated results.

### 5.5.3 Results

The normalized BRDFs of the fixed-phase simulations using the Emcore TJPV cell unit cube are presented in Figure 5.19. In both cases there are four reflectance peaks with the same magnitude separated by  $90^\circ$ . This was expected and is verified through comparison with the measured BRDF of the CanX-1 EM in Figure 2.3. The first peak in Figure 5.19a is located at  $25^\circ$ , and at  $50^\circ$  in Figure 5.19b. This difference was due to the different initial model rotation angle and was expected.

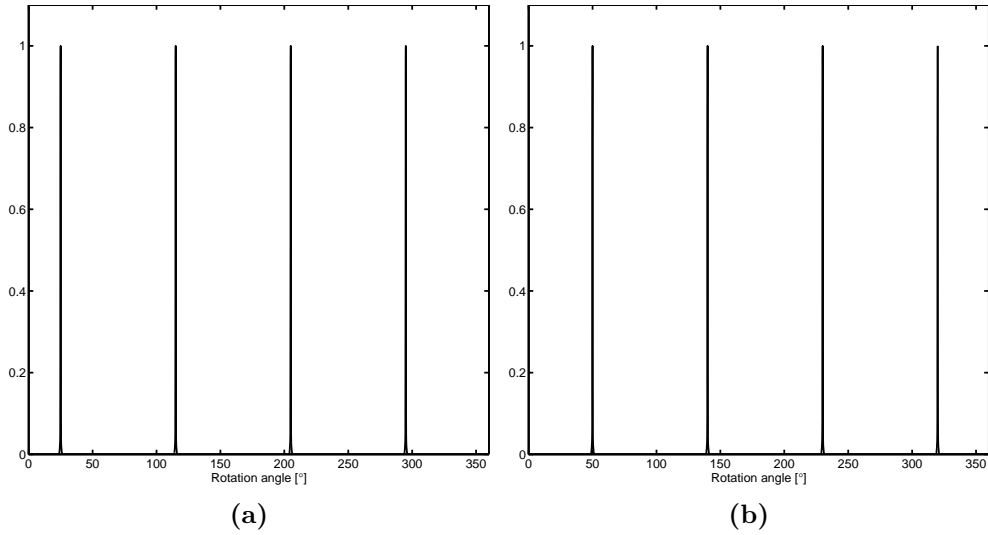


**Figure 5.19: The normalized BRDF of an Emcore TJPV cell unit cube for a fixed-phase simulation where  $\beta = 10^\circ$  with initial model rotation about the  $z$ -axis of (a)  $25^\circ$ , and (b)  $50^\circ$ .**

The normalized BRDF of the fixed-phase simulation using the 6061-T6 aluminum alloy unit cube is presented in Figure 5.20. As expected the BRDF is similar to that of the Emcore TJPV cell unit cube in Figure 5.19a but is less specular. Discontinuities are visible in this BRDF for angles-off-specular of approximately  $15^\circ$ , though they are difficult to see here due to scale. Their presence is caused by the inaccurate data contained in the aluminum look-up table, as was forecasted in Section 5.2. The collection of accurate sBRDF measurements for 6061-T6 aluminum alloy in the future will result in their removal from the BRDF.

Figure 5.21 shows the BRDF that resulted from the fixed-illumination simulation using the Emcore TJPV cell and 6061-T6 aluminum alloy unit

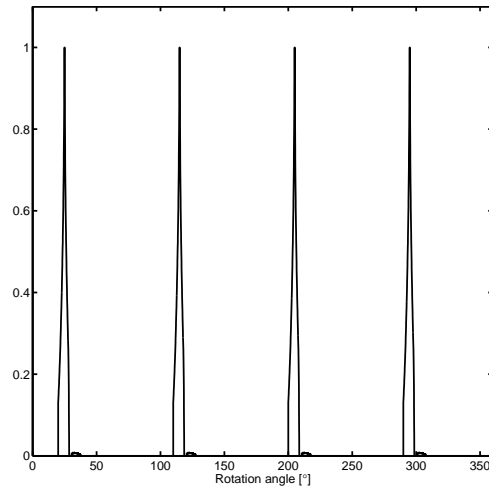


**Figure 5.20:** The normalized BRDF of a 6061-T6 aluminum alloy unit cube for a fixed-phase simulation where  $\beta = 10^\circ$  with initial model rotation about the  $z$ -axis of  $25^\circ$ .

cubes, rotated  $25^\circ$ . As expected they possess two peaks, the second of which has greater magnitude than the first, separated by  $180^\circ$ . The difference in intensity is caused by a difference in  $\theta_i$ . The first peak occurs when  $\theta_i = 25^\circ$ , while  $\theta_i = 65^\circ$  for the second. An increase in reflectance with increase in  $\theta_i$  was demonstrated in Section 2.2. The aluminum peaks are less specular due to the nature of its reflectance.

All four of the simulations that utilized a unit cube models have produced expected results. This verifies the synthetic sBRDF system and subsequent BRDF simulation for cubic models with similar scene geometry, where the observed facet surface normal vectors are parallel to the  $xy$ -plane, which contains the illumination and observation positions. These are the conditions with which the sBRDF of the CanX-1 EM will be synthesized.

The BRDFs for the two disc-model fixed-phase simulations are shown in Figure 5.22. The Emcore TJPV cell disc's BRDF in Figure 5.22a depicts 42 evenly spaced specular peaks of similar magnitude with zero reflectance in between. The 6061-T6 aluminum alloy disc's BRDF in Figure 5.22b exhibits the same number of evenly spaced peaks, however, the magnitude is more uniform and the reflectance is less specular. All results were expected.

Figure 5.23 provides the BRDFs of the fixed-illumination simulations that utilized the disc models. There are 10 equally spaced peaks in Figure 5.23a coinciding with 10 sheets that are both illuminated and observable during

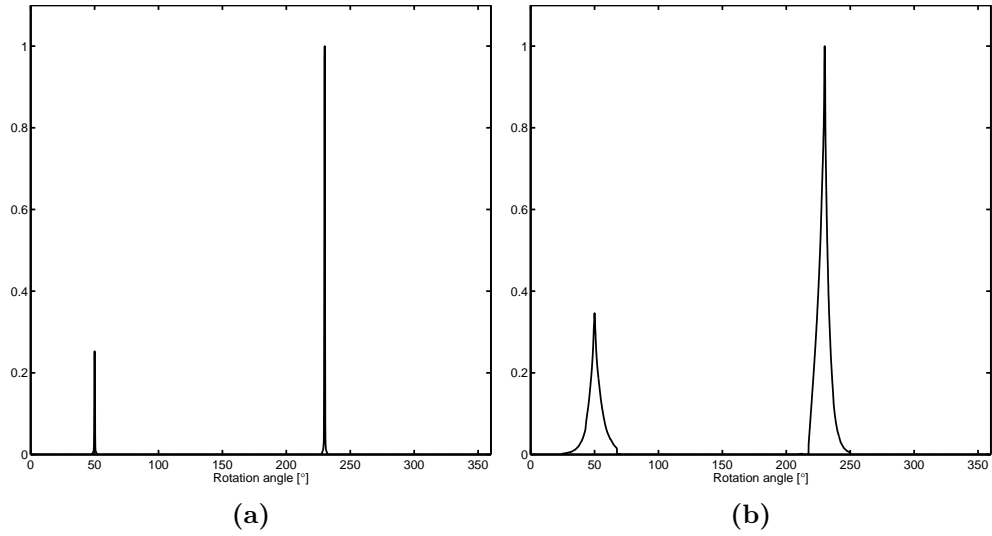


**Figure 5.21:** The normalized BRDF of (a) an Emcore TJPV cell unit cube, and (b) a 6061-T6 aluminum alloy unit cube for a fixed-illumination simulation with an initial model rotation about the  $z$ -axis of  $25^\circ$ .

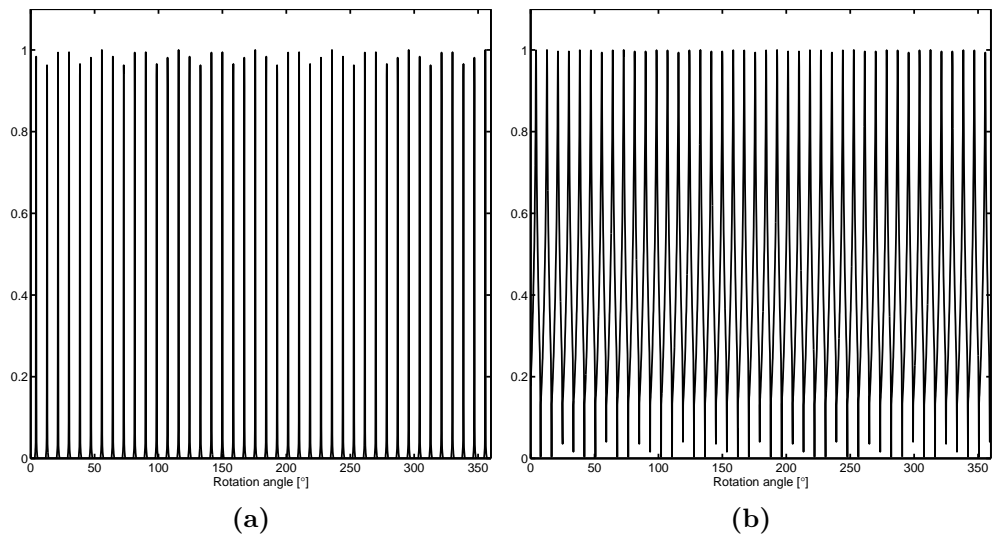


**Figure 5.22:** The normalized BRDF for a fixed-phase simulation where  $\beta = 10^\circ$ , of a disc made of (a) Emcore TJPV cell, and (b) 6061-T6 aluminum alloy.



the simulation. Their magnitudes exhibit a smooth curve similar to the one in Figure 5.10 and is a result of increasing phase angle as expected. The aluminum peaks are less specular than the solar cell, however, they depict the same curve in their magnitude.

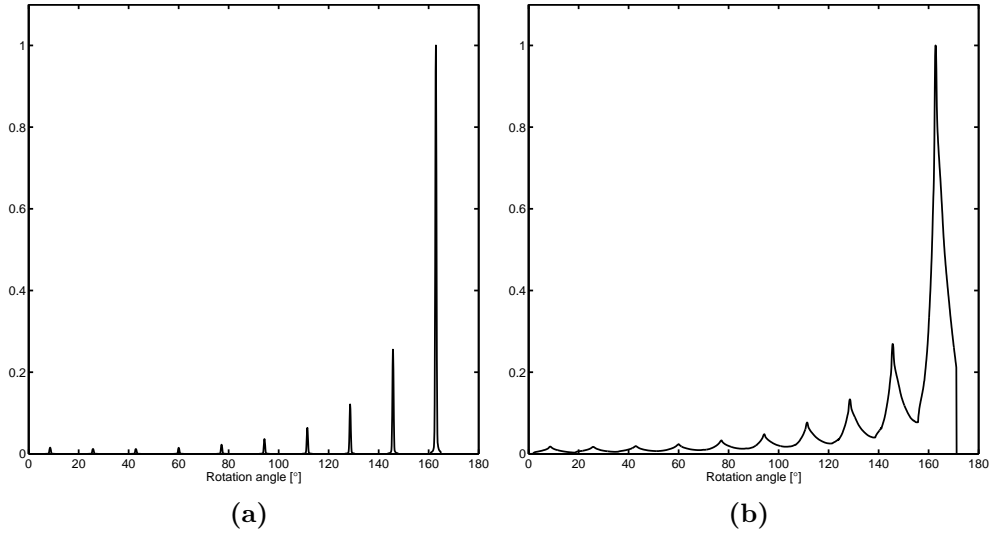


**Figure 5.23: The normalized BRDF for a fixed-illumination simulation of a disc made of (a) Emcore TJPV cell, and (b) 6061-T6 aluminum alloy.**

All four of the simulations that utilized a disc have produced expected results. This verifies the synthetic sBRDF system and subsequent BRDF simulation for similar models where the observed facet surface normal vectors are parallel to the  $xy$ -plane, containing the illumination and observation positions. That being said there is a caveat. The edge of a perfectly circular disk should reflect uniformly for a fixed-phase simulation, however, the disc model's edge was not perfectly circular due to facetization. An increase in the number of facets would result in a more uniform BRDF. Unfortunately, no measured BRDFs of discs could be obtained to provide an actual basis of comparison.

The sphere simulations demonstrated the limitations of the synthetic sBRDF system. This was expected because the sphere model contains many facets whose surface normal vectors were not parallel to the  $xy$ -plane, a constraint placed upon the system to access the material look-up tables. The fixed-phase BRDFs of the Emcore TJPV cell sphere and 6061-T6 aluminum alloy sphere are shown in Figures 5.24a and 5.24b, respectively. They possess a total of 38 peaks of varying magnitude separated uniformly, as was

expected. Both of these BRDFs should be uniform, similar to fixed-phase BRDFs of the disc in Figure 5.22. That is not observed, particularly in Figure 5.24a where the peak magnitude fluctuates dramatically. This effect is significantly reduced in Figure 5.24b though it is unclear why. The different composition of the two models was considered the cause, as this was the only difference between the two simulations, and further investigation was not conducted.

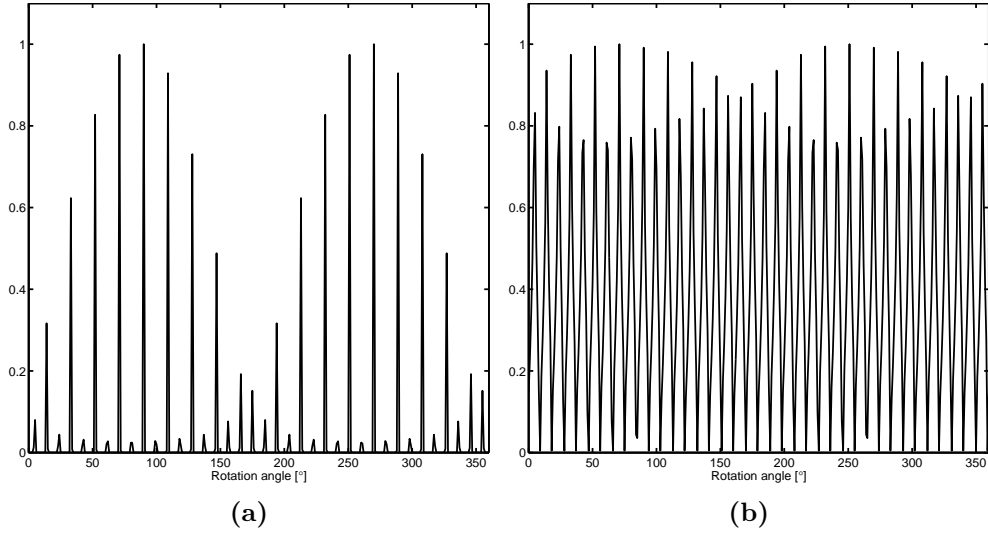


**Figure 5.24:** The normalized BRDF for a fixed-phase simulation where  $\beta = 10^\circ$ , of a sphere made of (a) Emcore TJPV cell, and (b) 6061-T6 aluminum alloy.

Lastly, the fixed-illumination BRDFs of the Emcore TJPV cell sphere and 6061-T6 aluminum alloy sphere in Figures 5.25a and 5.25b respectively, both contain 9 equally spaced peaks whose magnitudes exhibit a smooth curve. Similar to the disc BRDFs in Figure 5.23, the solar cell sphere is more specular than the aluminum one. As was expected, the overall curve in peak magnitude does resemble that of the discs in Figure 5.23 though the cause is unclear. A more detailed investigation was not conducted as it was beyond the scope of this research project.

All four of the simulations that utilized a sphere have produced results that are considered inaccurate. The synthetic sBRDF system is only verified for simulations where the observed facet surface normal vectors of a model are parallel to the  $xy$ -plane, which contains the illumination and observation positions. The sphere contains many facets that do not meet this criteria.

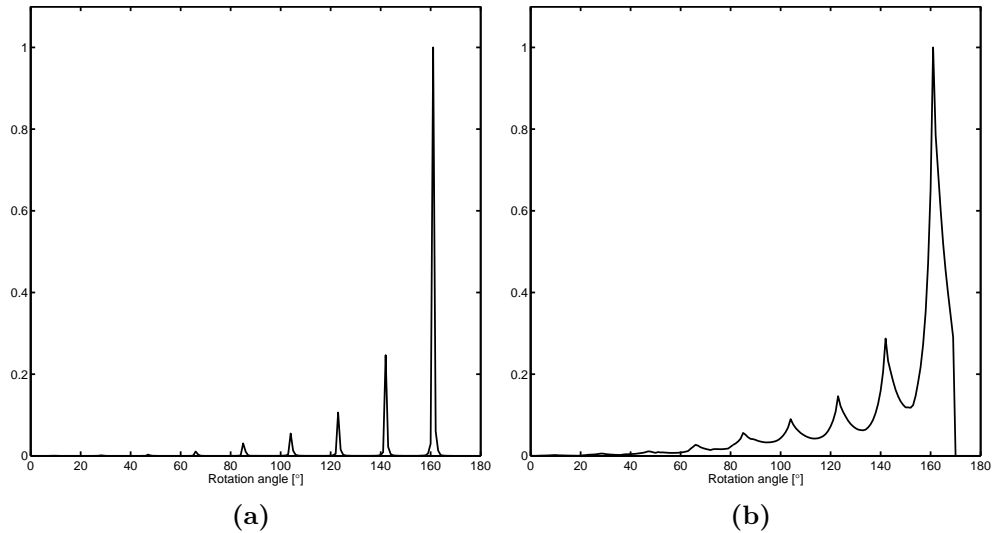


**Figure 5.25:** The normalized BRDF for a fixed-illumination simulation of a sphere made of (a) Emcore TJPV cell, and (b) 6061-T6 aluminum alloy.

Future work to incorporate off-plane measurements of material sBRDFs into the comprehensive look-up tables will allow for the modelling of models with these types of facets.

#### 5.5.4 Conclusion

The verification of the system’s ability to synthesize overall sBRDF of three-dimensional models is conditional upon the orientation of the model facets. Simulations using models that are comprised of facets whose surface normal vectors are parallel to the  $xy$ -plane are expected to produce valid results. The CanX-1 EM is comprised of facets that meet this criteria due to its cubic nature. It should also be noted that the level of facetization needs to be considered in cases where smoothly-curved surfaces are modelled since these curves are represented by triangular facets that are flat. As the CanX-1 EM does not contain curved surfaces this consideration is not required for this research project. A study to determine the required amount of facetization to accurately model curved surfaces should be completed in the future.

## 5.6 Summary of conclusions

The work presented here has verified the ability of the system to produce synthetic sBRDFs and subsequent BRDFs and colour ratios of the CanX-1 EM. More precisely, the system:

1. Identifies the material composition of each facet in a model.
2. Calculates the illumination and observation geometry of each facet.
3. Obtains the facet's sBRDF from its material look-up table.
4. Relies on sBRDF look-up tables that model material reflectance characteristics.
5. Calculates each facet's contribution to the overall sBRDF using its orthogonally-projected area.
6. Utilizes on-plane sBRDF data for off-plane observations with minor introduction of error.
7. Produces accurately simulated BRDFs of three-dimensional models comprised of facets whose surface normal vectors are parallel to the plane defined by the illumination and observation positions.

More importantly, the methodology presented here can serve as an example of how to verify spacecraft reflectance modelling systems.

Problems encountered with the system during this work include:

1. Inaccurate data in the measured sBRDF of 6061-T6 aluminum alloy.
2. Uncertain rate of change in overall reflectance associated with illumination angle.
3. Introduction of error by angular conversion to utilize on-plane sBRDF data for off-plane observations.
4. Difficulty modelling smoothly-curved surfaces.
5. Inability to produce accurate synthetic sBRDFs for three-dimensional models containing facets whose surface normal vectors are not parallel to the plane defined by the illumination and observation positions.

It is interesting to note that four of the system's current problems are sourced to the comprehensive material reflectance database. Now that the deficiencies and limitations of the current sBRDF look-up tables have been established, future work to address them will ensure that the synthetic spacecraft sBRDF system will increase in verifiable ability.

# 6 The Synthetic sBRDF of the CanX-1 EM

The aim of this research project was to develop a system that could accurately model spacecraft reflectance, producing a synthetic ground truth. The first spacecraft to be modelled by this system was the CanX-1 EM. Simulation scenarios were designed to reproduce the experimental setup of the spacecraft ground truth characterization experiment presented in Section 2.1. First, the synthetic sBRDF was interpreted and compared with the measured reflectance factor. Next, a simulated BRDF was interpreted and compared with a measured photometric light curve. Finally, colour ratios were then interpreted using unit cube CAD models. All interpretations were conducted towards characterizing the surface composition of the spacecraft.

## 6.1 Experiment aim and objectives

The aim of the experiment was to synthesize the sBRDF of the CanX-1 EM and use it to produce BRDFs and colour ratios. Results would be used to interpret the surface composition of the spacecraft for characterization. They would be validated through comparison with the measured reflectance factor and light curve by Bédard and Lévesque [22].

The five main objectives of the experiment were to:

1. Interpret the synthetic sBRDF of the +X side of the spacecraft for surface composition characterization.
2. Compare the synthetic sBRDF of the +X side of the spacecraft with the measured reflectance factor shown in Figure 2.5.
3. Interpret the simulated BRDF of the spacecraft for surface composition characterization.
4. Compare the simulated BRDF of the spacecraft with the measured photometric light curve shown in Figure 2.3.

5. Interpret the colour ratios of the spacecraft for surface composition characterization.

## 6.2 Experiment setup and procedure

The details of the experiment to produce synthetic sBRDFs of the CanX-1 EM are described in this section. The setup and procedure was developed to reproduce that of Bédard and Lévesque [22] during their characterization of the spacecraft in a controlled environment, as described in Section 2.1.

### 6.2.1 Experimental subject

The CanX-1 EM spacecraft is cubic with a shortest side length of 11 cm and longest side length of 12.45 cm. The exact dimensions of the spacecraft's features were determined using scaled photographs of its six sides, one of which is provided in Figure 6.1. Measurements were taken using a Matlab package. This approach was chosen as it allowed for more accurate measurements to be made, having an error of  $\pm 0.1$  mm, and only required physical access to the spacecraft for a short period of time.

The CAD model was built with measurement specifications to the tenth of a millimetre. The dimensions were defined for 1 CAD unit to equal 1 cm. The resulting model is comprised of 698 triangular facets, each representing one of three materials. Figure 6.2 shows this spacecraft CAD model. 6061-T6 aluminum alloy and Emcore TJPV cell, respectively in red and blue, were applied as these were the actual component materials of the spacecraft. Lord Aeroglaze 276A reflective white low-outgassing paint was applied to surfaces that were not aluminum or solar cell. This material was chosen as its reflectance was spectrally uniform, shown in Figure 5.2c, and its inclusion within the overall spacecraft sBRDF would not affect the spectral characteristics of the other two materials.

Unit cubes of Emcore TJPV cell and 6061-T6 aluminum alloy were also employed during this experiment. The aluminum cube model is shown in Figure 5.16a.

### 6.2.2 Experimental setup

The CanX-1 EM was initially positioned with its centroid located at the origin of the Cartesian coordinate system and oriented with its sides facing in the direction indicated by their labels. For example, the surface normal vectors of the +X side were parallel to the + $x$ -axis. Both illumination and observation

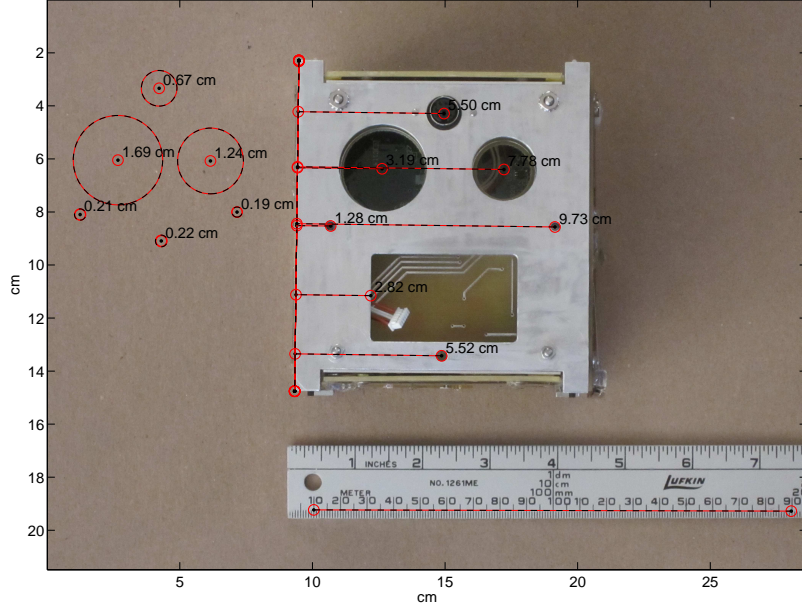


**Figure 6.1:** A scaled photograph of the CanX-1 EM with measurements.

positions were placed in the  $xy$ -plane and radially located 1000 units from the centroid of the subject. This was chosen to obtain the required model-height to radial-distance-of-observation ratio of 1:100 as suggested in Section 4.6.2.

Simulations using the unit cubes were similarly arranged, though the model-height to radial-distance-of-observation ratio was closer to 1:1000 as they were only 1 unit tall.

### 6.2.3 Experimental procedure

Four simulations were performed for this experiment. In the first the +X side of the CanX-1 EM was observed for four phase angle scenarios where  $\beta = 2 \cdot \theta_i = 2 \cdot \theta_o = 5^\circ, 30^\circ, 60^\circ$  and  $90^\circ$ . This simulation scenario is shown in Figure 6.3a. The synthetic sBRDF produced from this simulation was expected to have similar spectral features as the reflectance factor in Figure 2.5 for similar phase angle. These features associated with solar cell were predicted to shift,

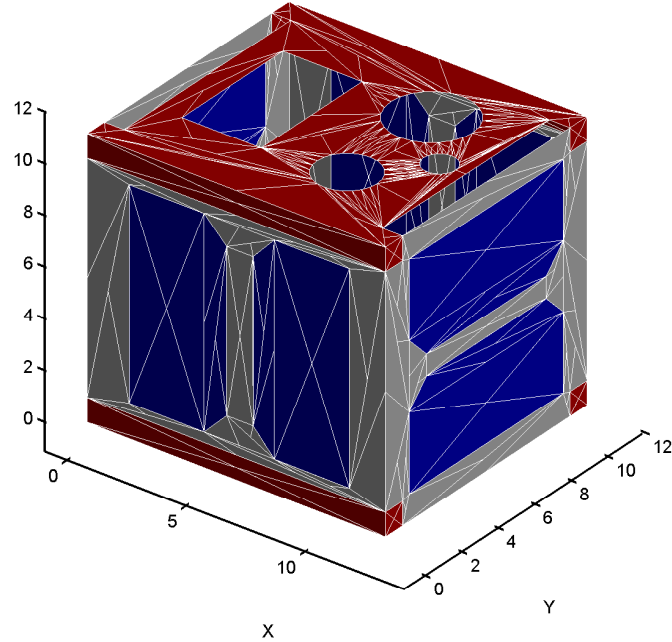


**Figure 6.2: The CanX-1 EM CAD model.**

and the overall intensity of reflectance was expected to change, with  $\theta_i$ . These relationships were shown in Chapter 2.

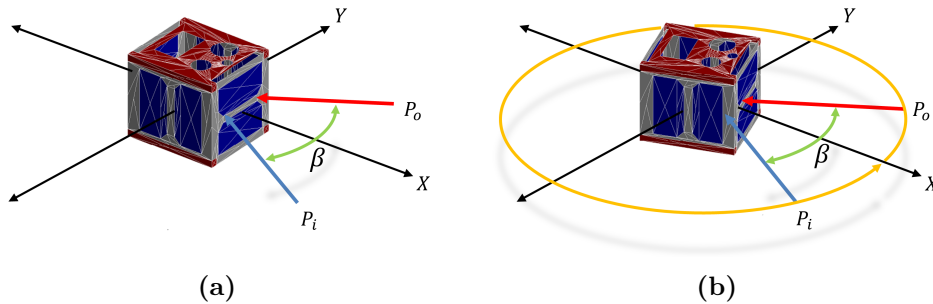


**Figure 6.3: The (a) phase angle, and (b) fixed-phase simulation scenarios for this experiment.**

The second simulation of the CanX-1 EM was fixed-phase where  $\beta = 10^\circ$  and the illumination and observation positions were rotated  $360^\circ$  about the  $z$ -axis in increments of  $0.1^\circ$ . The model was initially rotated  $25^\circ$  about the



$z$ -axis so that the first peak of the expected BRDF would not be located at  $0^\circ$ . This simulation scenario is presented in Figure 6.3b. The simulated BRDF was expected to have similar features as the photometric light curve presented in Figure 2.3 with a  $90^\circ$  separation of peaks and alternating variation in peak magnitude.

The last two simulations were fixed-phase, utilizing the unit cubes of Em-core TJPV cell and 6061-T6 aluminum alloy. Similar to the spacecraft simulation the illumination and observation positions were rotated  $360^\circ$  about the  $z$ -axis in increments of  $0.1^\circ$  maintaining  $\beta = 10^\circ$ . The resulting normalized BRDFs and colour ratios were expected to provide a reference for interpretation of those produced using the CanX-1 EM.

## 6.3 Results

### 6.3.1 Synthetic sBRDF of the CanX-1 EM

The synthetic sBRDFs of the +X side of the CanX-1 EM for four phase angles are shown in Figure 6.4. Prominent spectral features are present in the 600 to 800 nm range and shift towards shorter wavelength with an increase in  $\theta_i$ . Also, the magnitude of the sBRDF decreases from  $\beta = 5^\circ$  to  $30^\circ$  and increases thereafter.

### 6.3.2 Simulated BRDF of the CanX-1 EM

The simulated BRDF of the CanX-1 EM, initially rotated  $25^\circ$  about the  $z$ -axis, for a fixed-phase angle simulation where  $\beta = 10^\circ$  is shown in Figure 6.5. The peaks alternate in magnitude and are separated by  $90^\circ$ . Each peak presents a wider, less-specular base about  $10^\circ$  wide upon which a thinner  $1^\circ$  wide specular feature sits. The wider bases of taller peaks are themselves taller. There are also discontinuities in the reflectance located at a greater rotation angle of approximately  $5^\circ$  from each BRDF peak though they are difficult to see in the figure due to scale.

### 6.3.3 Normalized simulated BRDF and colour ratios

Figure 6.6a presents the normalized BRDF and colour ratios for the first BRDF peak in Figure 6.5, coinciding with a  $25^\circ$  rotation angle. The colour ratios are fairly uniform across the wider, less-specular base of the BRDF. All except R/I exhibit a sharp increase near specular, where the B-band shows the greatest increase in magnitude. The discontinuity in the BRDF is more

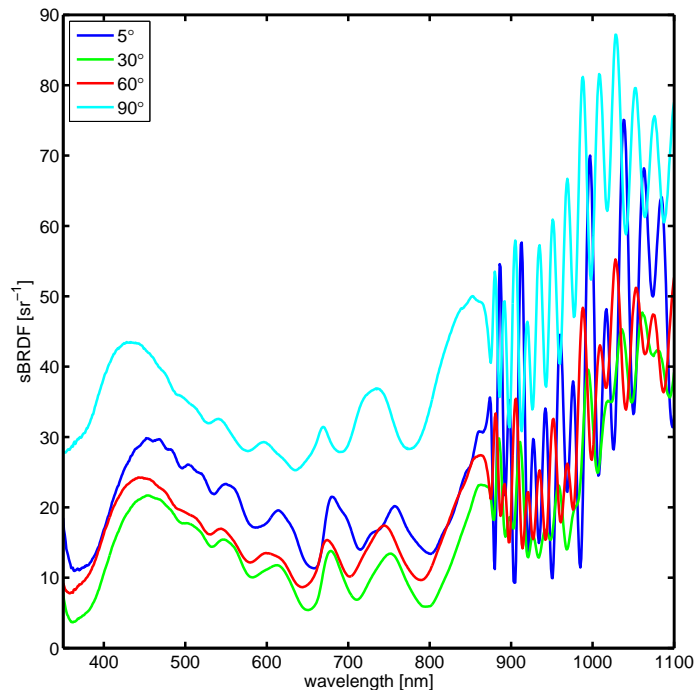


**Figure 6.4:** The synthetic sBRDF of the +X side of the CanX-1 EM for four phase angles.

obvious here as evidenced by the colour ratios. It is located at a rotation angle of approximately  $5^\circ$  greater than specular.

The sBRDF for five rotation angles that frame the specular peak in Figure 6.6a are provided in Figure 6.6b. The sBRDF at specular, for a rotation angle of  $25^\circ$ , exhibits a plethora of spectral features. These diminish as the rotation angle moves away from specular until only one feature at 800 nm is present though difficult to see in this figure due to the scale.

Figure 6.7a presents the normalized BRDF and colour ratios for the second BRDF peak in Figure 6.5, coinciding with a  $115^\circ$  rotation angle. The colour ratios behave exactly as they did for the first peak. The R/I is uniform while the greatest increase is in the B-band near specular, however, this increase is smaller in magnitude than it was for the  $25^\circ$  rotation angle. The same discontinuity for a rotation angle of  $5^\circ$  greater than specular is present.

Finally, the sBRDFs for five rotation angles that frame the specular peak in Figure 6.7a are provided in Figure 6.7b. The sBRDF for a rotation angle of  $115^\circ$  exhibits the same spectral features as that of  $25^\circ$ , which also diminish

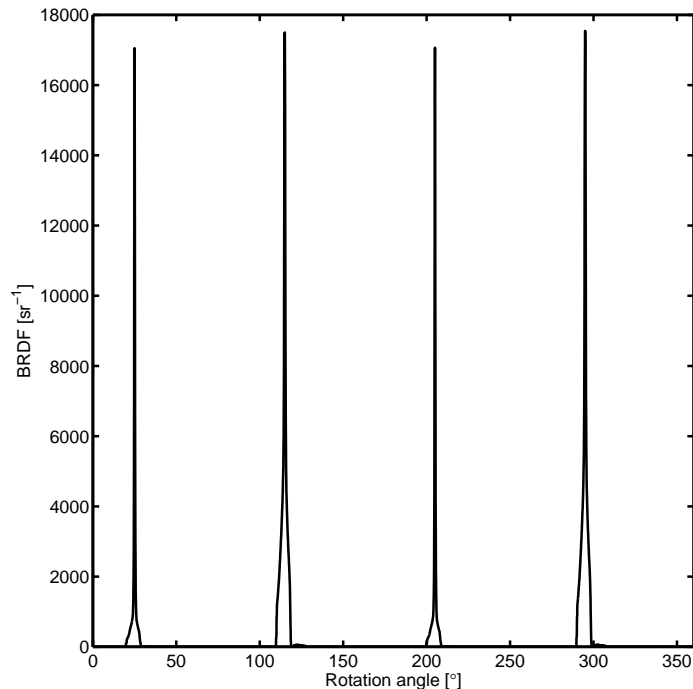


**Figure 6.5: A BRDF of the CanX-1 EM, initially rotated  $25^\circ$  about the  $z$ -axis, for a fixed-phase simulation where  $\beta = 10^\circ$ .**

as the rotation angle moves away from specular until only the 800 nm feature is present. This feature is more readily seen in this figure than in Figure 6.6b.

#### 6.3.4 Normalized simulated BRDFs and colour ratios of the unit cubes for fixed-phase

The normalized BRDF for the 6061-T6 aluminum alloy unit cube, initially rotated  $25^\circ$  about the  $z$ -axis, for a fixed-phase angle simulation where  $\beta = 10^\circ$  is shown in Figure 5.20. All four peaks present similar reflectance with a width of about  $10^\circ$ . Figure 6.8a depicts the normalized BRDF and colour ratios as a function of rotation angle from specular. The colour ratios are fairly uniform across the BRDF with a discontinuity located at a rotation angle of approximately  $5^\circ$  greater than specular.

The normalized BRDF for the Emcore TJPV cell unit cube, initially rotated  $25^\circ$  about the  $z$ -axis, for a fixed-phase angle simulation where  $\beta = 10^\circ$  is shown in Figure 5.19a. All four peaks present similar reflectance with a width of about  $1^\circ$ . Figure 6.8b depicts the normalized BRDF and colour ratios as a

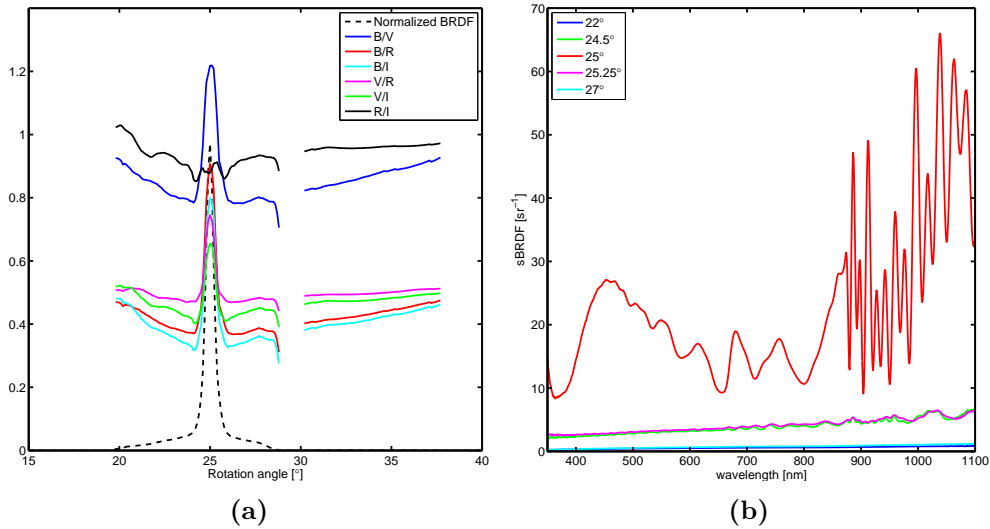


Figure 6.6: (a) A magnified region of the simulated BRDF in Figure 6.5 for a spacecraft rotation angle of  $25^\circ$ , which has been normalized, and the associated colour ratios. (b) The synthetic sBRDF for five rotation angles framing the specular region in Figure 6.6a.

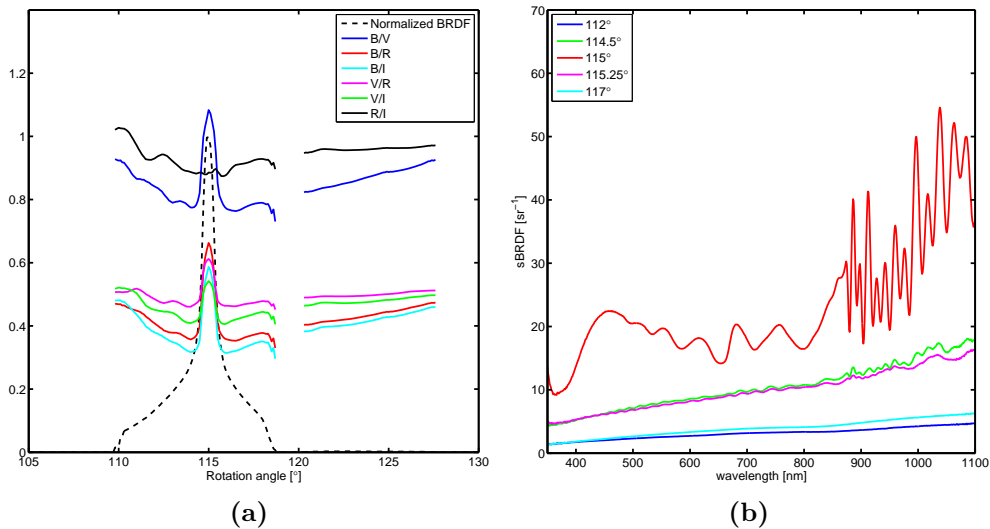
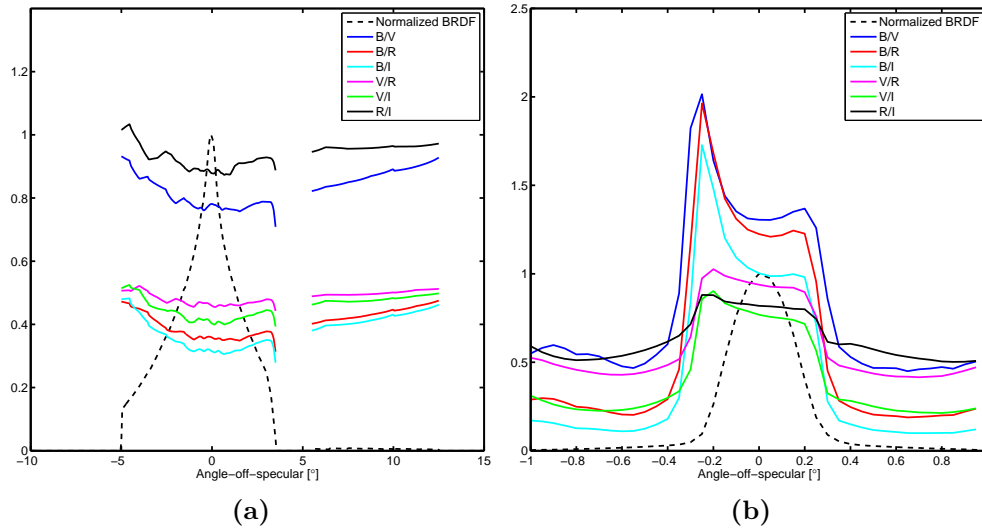


Figure 6.7: (a) A magnified region of the simulated BRDF in Figure 6.5 for a spacecraft rotation angle of  $115^\circ$ , which has been normalized, and the associated colour ratios. (b) The synthetic sBRDF for five rotation angles framing the specular region in Figure 6.7a.

function of rotation angle from specular. The colour ratios indicate a greater reflectance in the B-band than any other.



**Figure 6.8:** A normalized region of the BRDF and colour ratios for a fixed-phase simulation where  $\beta = 10^\circ$  of (a) a 6061-T6 aluminum alloy unit cube, and (b) an Emcore TJPV cell unit cube. Note that the normalized BRDF and colour ratios are presented as functions of rotation angle from specular as the reflectance is the same for each side of the respective unit cubes.

## 6.4 Discussion

### 6.4.1 Interpreting the synthetic sBRDF

The prominent spectral features in the 600 to 800 nm range of the synthetic sBRDF in Figure 6.4 coincide with those of Emcore TJPV cell, depicted in Figures 2.9b and 5.2a. These features are a result of thin-film interference, a common spectral phenomenon of solar cells which shift to shorter wavelengths with an increase in  $\theta_i$ . Figures 2.7 and 5.4a show this relationship. The presence of Emcore TJPV cell in the spectra was expected as the +X side of the CanX-1 EM is dominated by this material. While 6061-T6 aluminum alloy is also present on this side of the model its characteristic 800 nm absorption feature, depicted in Figures 2.8a and 5.2b, is undetectable.

The increase in sBRDF magnitude coinciding with an increase in  $\beta$  was expected as it was seen in Figures 2.7, 2.8, and 5.4, however, this was only observed where  $\beta > 30^\circ$ . While the decrease from  $\beta = 5^\circ$  to  $30^\circ$  was not expected it can be explained. This decrease, shown in Figure 5.4, is a result of fitting a cubic spline curve to the limited number of measured sBRDFs to develop the comprehensive look-up tables. Developing a more accurate reflectance database in the future will ensure that changes in sBRDF magnitude are more realistic.

#### 6.4.2 Comparing the synthetic sBRDF with the measured reflectance factor

The reflectance factor in Figure 2.5 is not an equivalent quantity to the sBRDF in Figure 6.4 and can not be quantitatively compared. The reflectance factor does not represent the relationship between reflectance magnitude and illumination angle. Normalizing the sBRDF for all phase angles to one wavelength produces a quantity that is more readily comparable, though it is emphasized that these two quantities are still not equivalent. Figure 6.9 presents the sBRDF of the +X side of the CanX-1 EM for four phase angles, normalized at a wavelength of 439 nm, with an  $x$ -axis that has been scaled to match that of the reflectance factor.

The measured reflectance factor in Figure 2.5 and the normalized sBRDF in Figure 6.9 possess similar characteristics. They contain similar features in the 600 nm to 800 nm range which shift to shorter wavelength with increasing  $\theta_i$ , though their exact wavelength is not the same. This is attributed to the fact that the Emcore TJPV cells are not flush to the surface of the actual spacecraft, as shown in Figure 2.4. The future investigation of a CAD model that recreates such physical flaws and how they affect the sBRDF should be performed.

The variation in sBRDF magnitude, particularly exhibited in the features located above 900 nm is not seen in the reflectance factor. This is a result of the spline fit used to develop the comprehensive look-up tables and a more accurate reflectance database would reduce this variation. Unfortunately due to the different nature of the two quantities a quantitative comparison of reflectance magnitude is not possible between them.

The system has demonstrated its ability to model spacecraft reflectance through the similarities in spectral characteristics of the synthetic sBRDF and measured reflectance factor. The spectral differences between the two quantities are most likely caused by the “flawless” CAD model and any inaccuracies contained in the material reflectance database, as the system’s mathematical

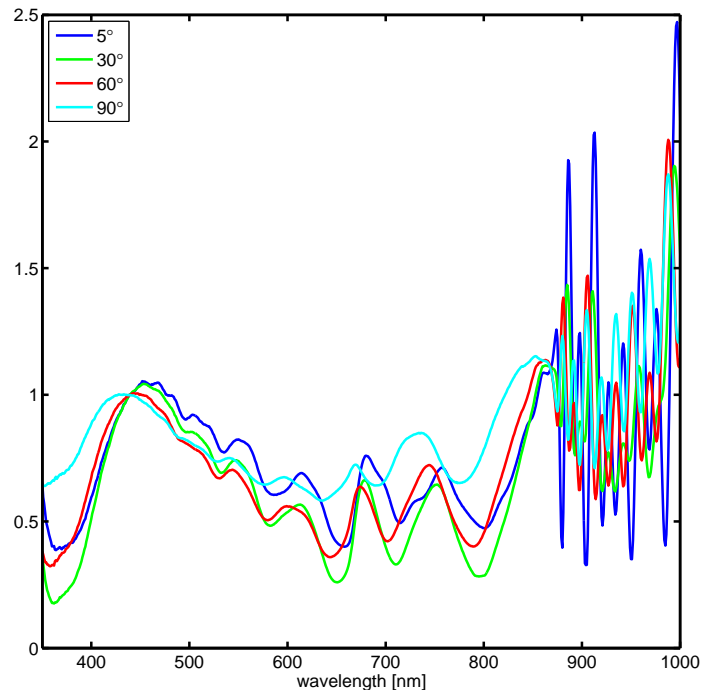


**Figure 6.9:** The synthetic sBRDF of the +X side of the CanX-1 EM for four phase angles, normalized at a wavelength of 439 nm.

algorithm was previously verified. Further investigation into CAD construction and look-up table development will increase the system’s ability to model spacecraft reflectance. The inequivalence of the two reflectance quantities leaves the causes for the difference in magnitude in question. Measuring the sBRDF of the CanX-1 EM in the future will enable a direct comparison with the synthetic sBRDF to further establish validity.

### 6.4.3 Interpreting the simulated BRDF

The  $90^\circ$  separation of the peaks observed in Figure 6.5 suggest that the CanX-1 EM is cubic. This pattern has been established in Figures 2.3, 5.19 and 5.20. The shape of the spacecraft is verified to be cubic through visual confirmation with the model shown in Figure 6.2.

The shape of the BRDF peaks show that the spacecraft is composed of at least two materials, one of which is more specular than the other. The thin specular peaks are similar to those of the Emcore TJPV cell unit cube shown in Figures 5.19 and 6.8b, while the wider less-specular bases are indicative of

6061-T6 aluminum alloy depicted in Figures 5.20 and 6.8a. The CanX-1 EM model is known to possess both materials so the presence of their reflectance characteristics in the BRDF is expected.

The ordering of spacecraft side observation was  $+X \rightarrow +Y \rightarrow -X \rightarrow -Y$ . Both X sides exhibit less reflectance overall combined with a shorter less-specular base feature when compared to both Y sides. Visual inspection of the model in Figure 6.2 shows that all four of these sides possess the same coverage of Emcore TJPV cell. That being said, the X sides, with an approximate surface area of  $122 \text{ cm}^2$  and horizontal solar cell orientation, have much less 6061-T6 aluminum alloy than the Y sides, which have a surface area closer to  $138 \text{ cm}^2$  and vertical solar cell orientation. The variation in peak BRDF magnitude is therefore unclear as this could be the result of three causes: the Y sides possess a greater surface area, the Y sides have a greater coverage of aluminum, and the orientation of the solar cells are different between the X and Y sides. Further investigation into the causes of this variation was not performed due to time constraints, though the inclusion of off-plane observation angles in the sBRDF look-up tables would eliminate solar cell orientation as a possible cause. The height of the less-specular base features, however, are attributed to the difference in the presence of aluminum on the surface of the spacecraft.

The discontinuities present in the BRDF are due to the inaccurate measured sBRDF of the 6061-T6 aluminum alloy that was used to develop the comprehensive look-up table. This is confirmed by Figure 5.20, which also contains these discontinuities. These are expected to disappear with the development of a more accurate material reflectance database.

#### 6.4.4 Comparing the simulated BRDF with the measured photometric light curve

The simulated BRDF in Figure 6.5 contains similar characteristics as the photometric light curve in Figure 2.3. The specular peaks have the same angular separation of  $90^\circ$  and sit atop wider, less-specular base features. The measured light curve, however, does not depict the specularity of the simulated BRDF for two reasons. The first is that measurements were made with a greater change in rotation angle between them, leaving the actual shape of the light curve uncertain. The second is that the surfaces of the actual spacecraft are not perfectly flush, shown in Figure 2.4, which result in a wider rotation angle range of specular reflection. A better idea of the light curve shape would be obtained by measuring intensity of the CanX-1 EM with smaller increments in rotation angle. Also, a more realistic CAD model would be



able to recreate the unevenness of the spacecraft surfaces and its construction should be investigated in the future. Unfortunately due to the different nature of the two quantities a quantitative comparison of reflectance magnitude is not possible between them.

The alternating peak magnitudes that were observed in the simulated BRDF are not reproduced as in the measured light curve. This is observed in the contrasting reflectance of the -X side which has the lowest simulated intensity but the greatest measured intensity. This is attributed to the non-flushness of the Emcore TJPV cells and the presence of features on the surface of the actual spacecraft that were not reproduced on the CAD model, as no other causes could be determined.

Finally, the simulated BRDF goes to zero between the reflectance features while the measured photometric light curve does not. This is attributed to the surface features of the CanX-1 EM such as rivets and the edges of Emcore TJPV cells, shown in Figure 2.4, which exhibited directional- and uniform-diffuse components of reflection. These surface features were not included on the CAD model as their presence was not considered within the scope of this thesis. The utility of their inclusion on future CAD models towards characterization is uncertain and an investigation should be performed.

Most differences between the simulated BRDF and measured BRDF are believed to be caused by the physical differences between the CAD model and actual spacecraft. Investigating the simulated BRDFs of CAD models that include surface features and imperfections is required. While the exact shape of the measured CanX-1 EM light curve is uncertain, the system has demonstrated an ability to produce simulated BRDFs. Measuring the reflectance of the CanX-1 EM with smaller increments in rotation angle will remove uncertainty from the shape of its light curve and is expected to further validate the efficacy of the system to simulate BRDFs.

#### 6.4.5 Interpreting the colour ratios

The uniform colour ratios across the wider, less-specular base of the normalized BRDFs in Figures 6.6a and 6.7a are indicative of 6061-T6 aluminum alloy, as depicted in Figure 6.8a. The discontinuity is also attributed to the aluminum; its presence was expected due to the inaccurate aluminum sBRDF data in the comprehensive look-up table. The sBRDFs coinciding with the uniform colour ratios in Figures 6.6b and 6.7b confirms the presence of 6061-T6 aluminum alloy as they depict its absorption feature, previously seen in Figures 2.8a and 5.2b.

The presence of Emcore TJPV cell is responsible for the sharp increase near specular of all colour ratios excluding R/I, particularly those including the B-band, in Figures 6.6a and 6.7a. This was observed for the solar cell unit cube shown in Figure 6.8b. Confirmation is provided by the sBRDF located at specular in Figure 6.6b which is that of Emcore TJPV cell, whose thin-film interference features have been shown in Figures 2.9b and 5.2a.

A comparison of the colour ratios near specular shows a greater change in the B-band for the +X side of the spacecraft in Figure 6.6a than for the +Y side in Figure 6.7a. This would appear to suggest that the solar-cell-to-aluminum ratio is higher on the +X side of the spacecraft than that of the +Y. A visual inspection of the CanX-1 EM confirms this, however, the associated sBRDFs at specular say otherwise. The magnitude of Emcore TJPV cell reflectance is actually less in Figure 6.7b than in Figure 6.6b. Since each side is known to have the same solar cell coverage the only explanation for this difference is their orientation, where they are horizontal on the X sides and vertical on the Y. The horizontal orientation locates facet centroids above and below the  $xy$ -plane meaning the  $\Delta\phi$  conversion in Section 4.1.2 is relied upon more heavily to access the Emcore TJPV cell sBRDF look-up table. The vertical orientation locates facet centroids much closer to, if not on, the  $xy$ -plane thereby reducing the requirement for this conversion. The sBRDF of the +Y side in Figure 6.7b can therefore be considered more accurate than that of the +X side in Figure 6.6b. Extending the look-up tables to include off-plane sBRDF measurements will eliminate the requirement for the  $\Delta\phi$  conversion and the resulting inaccuracy of the synthetic sBRDF.

## 6.5 Conclusion

The synthetic sBRDF system demonstrated its ability to produce quantities that can be used to characterize unresolved spacecraft. It produced quantities with similar characteristics to those measured using the CanX-1 EM spacecraft, evaluated qualitatively. A quantitative comparison between simulated and measured quantities was not possible due to differences in their nature. Simulated quantities were then interpreted to characterize the CanX-1 EM's surface composition, which was verified through investigation of the actual spacecraft. Note that the interpretation of synthetic sBRDFs, simulated BRDFs, and colour ratios required knowledge of the reflectance of the component materials, emphasizing the importance of an inclusive database.

The synthetic sBRDF of the spacecraft included the spectral features of Emcore TJPV cell, confirming its presence. The solar cell features shifted

appropriately with changes in  $\theta_i$ . 6061-T6 aluminum alloy could not be detected. The relationship between sBRDF magnitude and  $\theta_i$  is not modelled accurately due to the limited number of measured sBRDFs used to develop the comprehensive look-up tables.

Comparing the measured reflectance factor to the synthetic sBRDF required a normalization of the latter. The same Emcore TJPV cell spectral features were present in both quantities and shifted with  $\theta_i$ . A quantitative comparison of reflectance magnitude could not be performed due to the different nature of the two quantities.

The simulated BRDF showed that the spacecraft was cubic and composed of at least two materials, one of which was more specular than the other. The variation in peak shape indicated that each side contained different abundances of these two materials. The cause for the difference in peak height could not be determined.

The measured photometric light curve and simulated BRDF of the CanX-1 EM possessed similar characteristic features. The peaks were separated by  $90^\circ$  and showed highly specular reflectance. The larger change in rotation angle leaves the finer shape of the measured light curve in question. The difference in peak and minimum magnitudes is attributed to the uneven surface and small features on the spacecraft that were not included on the CAD model.

Finally, the colour ratios suggested that the spacecraft was comprised of two materials. The first material exhibited uniform reflectance characteristic of 6061-T6 aluminum alloy. The second material reflected the B-band more than any other, a characteristic of Emcore TJPV cell. Their presence was confirmed through investigation of the underlying sBRDF. The difference in colour ratios between spacecraft sides was due to the location of facets on the CAD model, requiring the use of an angle conversion to access the comprehensive look-up tables and not a variation in surface composition.

# 7 Conclusion

## 7.1 Summary of conclusions

The goal for this research project was to develop a system to produce the synthetic sBRDF of a spacecraft and to utilize this quantity to simulate BRDFs and colour ratios, quantities useful towards interpreting surface composition of spacecraft. All of the project aims were reached including the development of comprehensive look-up tables, the representation of complex spacecraft as a collection of triangular facets, the derivation of a mathematical algorithm to produce overall sBRDF, and the simulation of BRDFs, colour-filtered BRDFs, and colour ratios using synthetic sBRDFs. Based on the work presented in this thesis, the goal to produce a system to model spacecraft reflectance has been achieved.

The spacecraft ground truth and homogeneous material characterization experiments established the theoretical principals upon which the synthetic spacecraft ground truth system was developed. The CanX-1 EM spectrometric characterization demonstrated that a spacecraft's spectrum is the product of its surface material composition and the illumination and observation geometry of its panels. The synthesis of its spectrum required knowledge of the spectral reflectance characteristics of each of its materials including how these characteristics change with changes in illumination and observation geometry. The reflectance factor quantity was unable to meet this requirement as it contained a normalization that removed the relationship between reflectance intensity and illumination angle. Finally, the experiment could be reproduced for the validation of the developed spacecraft reflectance modelling system.

The spectrometric characterization of homogeneous materials showed that the sBRDF quantity met the requirements for modelling spacecraft reflectance as it was a function of illumination and observation geometry, as well as wavelength. It was capable of representing material reflectance characteristics and how they behaved with changes in illumination angle. The material sBRDFs acquired during this experiment provided the foundation for the comprehen-

sive look-up tables that were developed for the synthetic spacecraft ground truth system to utilize. Also, the experiment could be reproduced for the validation of the developed system to model spacecraft reflectance.

All previous modelling attempts demonstrated limited ability towards modelling the reflectance of spacecraft. In most cases these systems were not adequately described, negatively impacting their credibility; however, analysis of their approaches and products were used to develop the system for this research project. The most common shortcoming of these attempts was a reliance upon inaccurate material BRDF models. The most common feature was the use of spacecraft CAD models. As a result of this assessment the approach to build the spacecraft ground truth system within a numerical computing environment was developed, utilizing triangular-faceted CAD models and sBRDF look-up tables.

The spacecraft reflectance modelling system required the modification of two angles to create the comprehensive look-up tables and to allow for their access. The look-up tables were completed by first linearly interpolating the measured sBRDFs and then fitting them with a cubic spline for all illumination angles. The representation of complex spacecraft as a collection of matrix-defined triangular facets was then established. A mathematical algorithm was derived to synthesize the overall sBRDF of a model by calculating the illumination and observation geometry of its facets and accessing their respective material look-up tables. An angular conversion to enable access of in-plane sBRDFs for off-plane observations was instituted. This limited the ability of the synthetic spacecraft sBRDF system to scenarios where model facets were orientated parallel to the illumination and observation plane and placed a constraint on the distance between this plane and their centroids. Finally, the production of BRDFs, colour-filtered BRDFs, and colour ratios using synthetic sBRDFs was developed.

The ability of the synthetic spacecraft sBRDF system was verified using a series of experiments. The system was shown to be able to identify a facet's material composition, calculate its illumination and observation geometry, and obtain the correct sBRDF from the appropriate look-up table. It demonstrated its capability to produce an overall sBRDF by considering the orthographic projection of each facet. The utilization of in-plane sBRDF data for off-plane observations introduced minor error within the set scenario constraints, however, this was observed predominantly in colour ratios beyond the range of established reliability. Finally, the accurate representation of 3D models was confirmed. Most limitations of the spacecraft reflectance modelling system were sourced to the material reflectance database. These were caused by inaccuracies contained within the measured sBRDFs and the limited

sampling of few illumination angles, all of which were located in-plane. Representing smoothly-curved surfaces using flat triangular facets also presented a difficulty.

The synthetic sBRDF system demonstrated its ability to produce quantities useful towards the characterization of unresolved spacecraft. Simulated sBRDFs, BRDFs, and colour ratios of the CanX-1 EM were interpreted to identify its surface composition. Characteristic similarities between simulated and measured quantities validated the system. The presence of inaccurate sBRDF data in the material reflectance database caused unrealistic phenomena, though these phenomena were expected as the presence of the inaccuracies in the look-up tables was known. Finally, the angle conversion required to use in-plane sBRDF data for off-plane observations produced spectra that suggested different proportions of materials on alternating sides of the spacecraft, however, this was known to be untrue.

## 7.2 Future work

The current synthetic ground truth system models the overall sBRDF of a spacecraft in a laboratory setting, where model facet surface normal vectors are parallel to the plane defined by the illumination and observation positions and shadowing and masking effects need not be considered. The system can be further developed towards an end state able to produce spectrometric light curves of spacecraft in Earth orbit. This section presents the work that will be required to build upon the current system to accomplish this in the future.

### 7.2.1 Improved sBRDF look-up tables and a more comprehensive material reflectance database

The most straightforward way to improve the validity of synthetic spacecraft sBRDF system is to improve and add to the comprehensive material sBRDF look-up tables. This can be accomplished by obtaining more measured data, both in the plane defined by  $\theta_i$  as well as off-plane.

The measured sBRDF of 6061-T6 aluminum alloy for  $\theta_i = 60^\circ$  contained inaccurate data which was shown by the colour ratios in Figure 5.3b. As a result the cubic spline curve that was fit to this data was also inaccurate, leaving uncertainty in the  $\theta_{os} > 12^\circ$  range for aluminum. As a first step to improving the material database this sBRDF needs to be remeasured.

The spline fit used to determine the material sBRDF for  $\theta_i$  below  $10^\circ$  and above  $60^\circ$  was based on three measured points shown in Figure 7.1. It is suggested that sBRDF be collected for more  $\theta_i$  values in order to develop more accurate sBRDF look-up tables for the spacecraft material reflectance database. The author was able to produce a more accurate spline fit using the measured sBRDFs of seven  $\theta_i$  values during an impromptu investigation not included in this thesis. A formal investigation into the required number of measurements to optimize the sBRDF look-up tables for all  $\theta_i$  should be performed.

The measurement of material sBRDFs for off-plane observation angles is also suggested. Such an expansion to the sBRDF look-up tables would eliminate the need for the  $\Delta\phi$  conversion described in Section 4.6.2 in simulations where facet surface normal vectors are not parallel to, and contained by, the plane defined by the illumination and observation positions. Figure 7.1 provides a visualization of suggested measurements. Note that off-plane angles are not specified as they will depend on the specularity of the material being characterized. A study should be conducted to determine the required number of off-plane observations to achieve a truly comprehensive look-up table.

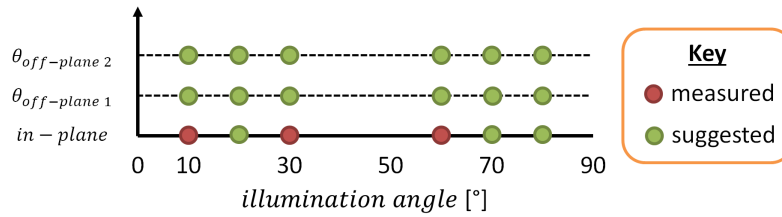


**Figure 7.1: The angles for which measurements were made of the material sBRDFs, all of which are located in-plane, and suggested off-plane measurements.**

The sBRDFs of more materials can be incorporated into the database as well. This will allow for a greater ability to produce synthetic sBRDFs of more types of spacecraft. The sBRDFs of an Azure 3G30A TJPV cell and MLI have already been obtained, however, they have not yet been developed into comprehensive look-up tables.

Finally, an assumption made for this research project is that the reflectance of these spacecraft materials is isotropic. An investigation to determine whether this is the case is strongly suggested as the reflectance of anisotropic materials can vary with their orientation while maintaining illumination and observation geometries.

### 7.2.2 More realistic CAD models

Spacecraft reflectance exhibits phenomena that have not been incorporated into the current CAD models. For instance, individual solar cells do not lie perfectly flat on a panel and therefore do not concurrently exhibit specular reflection. Future models should be modified to replicate this effect by applying a distribution to the vertices of solar panel facets, parallel to the direction of their surface normal vectors, with designated magnitude determined through study. Also, smoothly-curved surfaces require increased facetization to be modelled accurately and an investigation into this possibility is suggested.

Knowledge of a spacecraft's centre of mass will allow for more accurate rotation modelling. The system currently rotates CAD models about their centroid, which will likely introduce error in proportion to the complexity of the spacecraft.

Most complex satellites possess articulating extremities such as Sun-pointing solar panels. Currently, CAD models are unable to reproduce this behaviour. The incorporation of this ability is required to simulate light curves of these spacecraft with certainty.



Finally, both shadowing and masking effects are not modelled. This was not required as the current CAD models did not possess extremities capable of these effects. It is presumed that one algorithm can be utilized to model both shadowing and masking as they are both based on the same ray-tracing principles. Further investigation is required.

### **7.2.3 Expanded CAD model library**

The current CAD model library only includes simple shapes and a model of the CanX-1 EM spacecraft. More spacecraft models are required for the system's utility to increase. Porting of developed spacecraft CAD models from other software packages should be investigated in order to reduce the amount of effort required to develop them from scratch. Conversely, the development of a spacecraft-building utility in the Matlab environment should also be considered.

### **7.2.4 On-orbit simulation scenarios**

The ability to simulate on-orbit scenarios must be incorporated. This requires utilizing time, spacecraft TLE, and pitch/yaw/roll data. Combining this state information will provide realistic spacecraft geometry for a given time interval, changing at the appropriate rate.

The Sun and observer positions must also be in the same coordinate frame as the spacecraft. A spacecraft-centred coordinate system would likely be the most straightforward to use as the centroid of the model is currently located at the origin.

### **7.2.5 Simulated sensor measurements**

A spacecraft's sBRDF, BRDF, colour-filtered BRDF, and colour ratios are not measurements obtained by optical sensors. These quantities are derived by subjecting measurements to data processing techniques. Section 1.1 described how telescopes measure flux to produce light curves, sometimes employing filters to produce colour light curves. The simulation of light curves is therefore more useful for interpreting measurements and can be achieved by incorporating solar irradiance of the spacecraft and the aperture area of the sensor into the mathematical algorithm. This ability is the proposed end state of the system.

# Bibliography

- [1] NASA Orbital Debris Program Office. Orbital debris quarterly newsletter, 2013.
- [2] L. del Monte. A european approach to space situational awareness. Technical report, European Space Agency, Brussels, Belgium, November 2007.
- [3] M. L. Stone and G. P. Banner. Radars for the detection and tracking of ballistic missiles, satellites, and planets. *Lincoln Laboratory Journal*, 12 (2):217–244, 2000.
- [4] G. R. Wagner. Navy transfers space surveillance mission to air force. *America’s Navy*, October 2004. URL [http://www.navy.mil/submit/display.asp?story\\_id=15597](http://www.navy.mil/submit/display.asp?story_id=15597).
- [5] J. D. Drummond and R. H. Rast. First resolved images of a spacespace in geostationary orbit with the keck-ii 10 m telescope. In *Proceedings of the 2010 AMOS Technical Conference*, Kihei, Maui, HI, September 2010. Maui Economic Development Board, Inc.
- [6] K. K. Luu, C. L. Matson, J. Snodgrass, S. M. Giffin, K. Hamada, and J. V. Lambert. Object characterization from spectral data. In *Proceedings of the 2003 AMOS Technical Conference*, Kihei, Maui, HI, September 2003. Maui Economic Development Board, Inc.
- [7] A. Jolley. Multicolour optical photometry of active geostationary satellites using a small aperture telescope. Master’s thesis, The Royal Military College of Canada, Kingston, ON, May 2014.
- [8] R. L. Scott and B. Wallace. Satellite characterization using small aperture instruments at drdc ottawa. In *Proceedings of the 2008 AMOS Technical Conference*, Kihei, Maui, HI, September 2008. Maui Economic Development Board, Inc.
- [9] P. Somers. Cylindrical rso signatures, spin axis orientation and rotation period determination. In *Proceedings of the 2011 AMOS Technical Conference*, Kihei, Maui, HI, September 2011. Maui Economic Development Board, Inc.

- 
- [10] D. Bédard. *Spectrometric Characterization of Artificial Earth-Orbiting Objects: Laboratory and Observational Experiments*. PhD thesis, The Royal Military College of Canada, Kingston, ON, September 2013.
- [11] D. Bédard and G. A. Wade. Analysis of time-resolved spectrometric measurement of the galaxy 11 geostationary satellite. Under preparation, June 2015.
- [12] D. Bédard, G. A. Wade, and A. Jolley. Interpretation of spectrometric measurements of active geostationary satellites. In *Proceedings of the 2014 AMOS Technical Conference*, Kihei, Maui, HI, September 2014. Maui Economic Development Board, Inc.
- [13] M. Bessel. Ubvri passbands. *Astronomical Society of the Pacific*, 102: 1181–1199, 1990.
- [14] D. Bédard. Measurement of the photometric and spectral brdf of small canadian satellites in a controlled environment. In *Proceedings of the 2011 AMOS Technical Conference*, Kihei, Maui, HI, September 2011. Maui Economic Development Board, Inc.
- [15] F. Chromey. *To Measure the Sky - An Introduction to Observational Astronomy*. Cambridge University Press, 2010.
- [16] W.J. Smith. *Modern Optical Engineering*. SPIE Press, 2008.
- [17] M. Zeilik and S. A. Gregory. *Introductory Astronomy & Astrophysics*. Thomson Learning, Inc., 4th edition, 1998.
- [18] M. J. Gaffey, E. A. Cloutis, M. S. Kelley, and K. L. Reed. *Asteroids*, volume III, chapter Mineralogy of Asteroids, pages 183–204. University of Arizona Press, 2003.
- [19] S. J. Bus, F. Vilas, and M. A. Barucci. *Asteroids*, volume III, chapter Visible-Wavelength Spectroscopy of Asteroids, pages 169–182. University of Arizona Press, 2003.
- [20] T. B. McCord, J. B. Adams, and T. V. Johnson. Asteroid vesta: Spectral reflectivity and compositional implications. *Science*, 168: doi:10.1126/science.168.3938.1445, June 1970.
- [21] K. Abercromby, J. Okada, M. Guyote, K. Hamada, and E. Barker. Comparisons of ground truth and remote spectral measurement of the for-sosat and ande spacecraft. In *Proceedings of the 2006 AMOS Technical Conference*, Kihei, Maui, HI, September 2006. Maui Economic Development Board, Inc.
- [22] D. Bédard and M. Lévesque. Analysis of the CanX-1 EM spectral reflectance measurements. *Journal of Spacecraft and Rockets*, 51(5):1492–1504, 2014. doi: 10.2514/1.A32643.
- [23] M. J. Duggin, J. F. Riker, W. Glass, K. A. Bush, D. Briscoe, M. Klein, M. L. Pugh, and B. Engberg. Multi-spectral image analysis for improved

- space object characterization. In *Proceedings of the 2008 AMOS Technical Conference*, pages 561–574, Kihei, Maui, HI, September 2008. Maui Economic Development Board, Inc.
- [24] D. Hall. Surface material characterization from non-resolved multi-band optical observations. In *Proceedings of the 2010 AMOS Technical Conference*, Kihei, Maui, HI, September 2010. Maui Economic Development Board, Inc.
- [25] A. B. Chaudhary, T. Payne, S. Gregory, and P. Dao. Fingerprinting of non-resolved three-axis stabilized space objects using a two-facet analytical model. In *Proceedings of the 2011 AMOS Technical Conference*, Kihei, Maui, HI, September 2011. Maui Economic Development Board, Inc.
- [26] F. E. Nicodemus, J. C. Richmond, and J. J. Hsia. *Geometrical Considerations and Nomenclature for Reflectance*. U.S. Department of Commerce, Washington, D.C., October 1977.
- [27] J. M. Palmer. *Handbook of Optics*, volume 2. McGraw-Hill, Tucson, Arizona, 1995.
- [28] P.W. Kervin, P. D. Hall, M. Bolden, and J. Toth. Phase angle: What is it good for? In *Proceedings of the 2010 AMOS Technical Conference*, Kihei, Maui, HI, September 2010. Maui Economic Development Board, Inc.
- [29] G. Schaepman-Strub, M. E. Schaepman, T. H. Painter, S. Dangel, and J. V. Martonchik. Reflectance quantities in optical remote sensing - definitions and case studies. *Remote Sensing of Environment*, 103:27–42, March 2006.
- [30] D. Bédard, G. A. Wade, and K. Abercromby. Laboratory Characterization of Homogeneous Spacecraft Materials. *Journal of Spacecraft and Rockets*, 00(00):1–10, 2015. doi: 10.2514/1.A33079.
- [31] X. D. He, K. E. Torrance, F. X. Sillion, and D. P. Greenberg. A comprehensive physical model for light reflection. *Computer Graphics*, 25(4): 175–186, July 1991.
- [32] R. Montes and C. Ureña. An overview of brdf models. Technical Report LSI-2012-001, Dept. Lenguajes y Sistemas Informáticos, University of Granada, Granada, Spain, 2012.
- [33] S. H. Westin, H. Li, and K.E. Torrance. A comparison of four brdf models. In H.W. Jensen and A. Keller, editors, *Eurographics Symposium on Rendering*, pages 1–10, April 2004.
- [34] G. J. Wells, L. Stras, and T. Jeans. Canada’s smallest satellite: The canadian advanced nanospace experiment (canx-1). Technical report, University of Toronto Institute for Aerospace Studies, Toronto, Ontario, 2002.

- 
- [35] M. Pharr and G. Humphreys. *Physically Based Rendering: From Theory to Implementation*. Morgan Kaufmann, Burlington, MA, 2 edition, 2010.
- [36] J.R. Maxwell, J. Beard, S. Weiner, D. Ladd, and S. Ladd. Bidirectional reflectance model validation and utilization. Technical Report AFAL-TR-73-303, Environmental Research Institute of Michigan (ERIM), October 1973.
- [37] G. J. Ward. Measuring and modeling anisotropic reflection. *SIGGRAPH*, 26(2):ACM-0-89791-479-1/92/007/0265, July 1992.
- [38] C. Früh. Analysis of observed and simulated light curves of space debris. In *Proceedings of International Astronautical Conference*, Prague, Czech Republic, 2010. International Astronautical Federation.
- [39] S. Arnold. Simulation of lightcurves by means of rendering. Master’s thesis, University of Bern, Bern, Switzerland, September 2011. Translated from German.
- [40] Osfield. *OpenSceneGraph*. OpenSceneGraph, December 2014. URL <http://www.openscenegraph.org/>.
- [41] Grimaldi. *LuxRender: GPL Physically Based Renderer*. LuxRender, December 2014. URL [http://www.luxrender.net/en\\_GB/index](http://www.luxrender.net/en_GB/index).
- [42] J. F. Riker, G. A. Crockett, and R. L. Brunson. The time-domain analysis simulation for advanced tracking (tasat). *SPIE*, 1697:297–309, 1992.
- [43] D. Hall, K. Hamada, T. Kelecý, and P. Kervin. Surface material characterization from non-resolved multi-band optical observations. In *Proceedings of the 2012 AMOS Technical Conference*, Kihei, Maui, HI, September 2012. Maui Economic Development Board, Inc.
- [44] K.M. Jorgensen. *Using Reflectance Spectroscopy to Determine Material Type of Orbital Debris*. PhD thesis, Colorado Center for Astrodynamics Research, University of Colorado, Boulder, CO, 2000.
- [45] J. R. Schott, S. D. Brown, R. V. Requeño, H. N. Gross, and G. Robinson. An advanced synthetic image generation model and its application to multi/hyperspectral algorithm development. *Canadian Journal of Remote Sensing*, 25(2):99–111, June 1999.
- [46] Modeling and Simulation Group. *The Digital Imaging and Remote Sensing Image Generation Model (DIRSIG)*. Rochester Insitute of Technology: Digital Imaging and Resmote Sensing (DIRS) Laboratory, December 2014. URL <http://dirsig.org/get>.
- [47] D. A. Bennett, J. A. Dank, D. W. Tyler, M. Gartley, and D. Allen. Ssa modeling and simulation with dirsig. In *Proceedings of the 2014 AMOS Technical Conference*, Kihei, Maui, HI, September 2014. Maui Economic Development Board, Inc.

- [48] R. L. Scott, A. Ellery, and M. Lévesque. Non-resolved detection of objects performing on orbit servicing in geostationary orbit. In *Proceedings of the 2011 AMOS Technical Conference*, Kihei, Maui, HI, September 2011. Maui Economic Development Board, Inc.
- [49] M. Ackermann. Blind search for microsatellites in leo: Optical signatures and search strategies. In *Proceedings of the 2003 AMOS Technical Conference*, Kihei, Maui, HI, September 2003. Maui Economic Development Board, Inc.
- [50] *Matlab R2015a Documentation*. MathWorks, May 2015. URL <http://www.mathworks.com/help/matlab/>.
- [51] T. Bajd, M. Mihelh, and M. Munih. *Introduction to Robotics*, chapter Rotation and Orientation, pages 9–36. Springer, 2013.
- [52] R. Paquin. *Handbook of Optics: Devices, Measurement, and Properties*, volume 2, chapter Properties of Metals. McGraw-Hill, New York, 1995.

## 8 Curriculum Vitae

**Name:** Alexander Alan Willison  
**Place of birth:** Oshawa, Ontario  
**Year of birth:** 1986

**Post-secondary education and degrees:** **M.Sc. Candidate** **2013-2015**  
Royal Military College of Canada  
Kingston, Ontario

**Additional Qualification in Teaching and Learning through e-Learning** **2011**  
University of Ontario Institute of Technology  
Oshawa, Ontario

**B.Ed., Senior Physics and Mathematics** **2011**  
University of Ontario Institute of Technology  
Oshawa, Ontario

**B.Sc., Astrophysics** **2007**  
University of Western Ontario  
London, Ontario

---

<b>Employment history:</b>	<b>Research Assistant</b>	<b>2014-2015</b>
	Space Surveillance Research Laboratory Royal Military College of Canada Kingston, Ontario	
	<b>Teaching Assistant</b>	<b>2014-2015</b>
	PHE104: General Physics (First year lab) PHE260: Astronomy and the Evolving Universe Physics Department Royal Military College of Canada Kingston, Ontario	
	<b>Faculty</b>	<b>2012-2013</b>
	SES4Ue: Grade 12 Earth and Space Science e-Learning Consortium Canadian Accredited Independent Schools Online	
	<b>Faculty</b>	<b>2011-2013</b>
	SPH4U: Grade 12 Physics SES4U: Grade 12 Earth and Space Science SNC1D: Grade 9 Science (Academic) Trinity College School Port Hope, Ontario	